

**A CMOS-compatible Electronic  
Nose Fabricated via Dielectrophoretic  
Assembly of Nanomaterials**

A thesis

submitted by

**Sam MacNaughton**

In partial fulfillment of the requirements

for the degree of

Master of Science

in

*Electrical and Computer Engineering*

TUFTS UNIVERSITY

*May, 2013*

© 2013, Sam MacNaughton

ADVISER: Sameer Sonkusale

Signature of Author .....

Sam MacNaughton

*Department of Electrical and Computer Engineering*

Certified by .....

Sameer Sonkusale

*Associate Professor,*

*Electrical Engineering*

*TUFTS UNIVERSITY*

*Thesis Supervisor*

Certified by .....

Tom Vandervelde

*John A. and Dorothy M. Adams Faculty Development Professor,*

*Electrical Engineering*

*TUFTS UNIVERSITY*

*Thesis Supervisor*

Certified by .....

Mehmet R. Dokmeci

*Assistant Professor, Electrical Engineering*

*NORTH EASTERN UNIVERSITY*

*Thesis Supervisor*

# Abstract

An electronic nose formed from a heterogeneous array of chemiresistors is presented. The sensor is fabricated in a novel, CMOS-compatible process by the sequential, dielectrophoretic assembly of a diverse set of chemiresistive nanomaterials (reduced graphene oxide, carbon nanotubes, and copper oxide nanowires) onto a silicon chip. Fabrication of the substrate and nanomaterials is detailed, as well is the process of sequential dielectrophoretic assembly to integrate the nanomaterials and substrate. Individually, the sensors show a high degree of sensitivity, demonstrating fractional changes of resistance of greater than 50% upon exposure to gas vapors. The entire chip with the ensemble of chemiresistors is shown to be an effective electronic nose, with distinguishable responses to ammonia, methanol, and toluene.

# Acknowledgements

This work would not have been possible without the continual support of all those around me. The denizens of 200 Boston have always provided me with a wealth of knowledge which has been integral to this work. Professor Rob White and his group have been especially helpful in the microfabrication travails of the past years.

My family and friends have been a constant source of inspiration and support. Without them, this work could never have been accomplished.

I would also like to thank my thesis committee of Dr. Mehmet Dokmeci and Dr. Tom Vandervelde. I can not think of two more qualified people to review my work.

Lastly, I'd like to acknowledge my advisor, Dr. Sonkusale, whose knowledge and wisdom have for many years been my guide through my academic endeavors.

# Table of Contents

Abstract .....	ii
Acknowledgements.....	iv
Table of Figures .....	ix
Chapter 1: Introduction.....	1
1.1 Motivation.....	1
Chapter 2: Background.....	8
2.1 Bottom Up vs. Top Down.....	8
2.1.1 Dielectrophoresis .....	9
2.1.2 Dielectrophoresis as a Means of Assembly .....	15
2.1.3 Other Assembly Methods .....	16
2.2 Chemiresistive Sensors .....	19
2.2.1 Metal Oxide Chemiresistors .....	19
2.2.2 Carbon Chemiresistors.....	21
2.2.3 Conductive Polymer Chemiresistors.....	25
2.3 Other Gas Sensing Mechanisms .....	26
2.4 Sensor Electronics.....	29
2.4.1 Wheatstone Bridge.....	29
2.4.2 Instrumentation / Operational Amplifiers.....	30
2.4.3 Analog to Digital Conversion.....	31

2.5	Signal Processing .....	32
2.5.1	Support vector machines .....	32
2.5.2	Artificial Neural Networks .....	33
2.5.3	Cluster Analysis .....	34
2.5.4	Principle component analysis .....	35
2.6	Electronic Nose .....	35
2.6.1	E-Nose Implementations .....	36
Chapter 3:	Fabrication .....	38
3.1	Silicon Electrode Array Photolithographic Fabrication .....	38
3.1.1	Lithography .....	38
3.1.2	Mask Design .....	41
3.1.3	Electrode Geometries .....	43
3.1.4	Packaging .....	43
3.2	Fabrication / Procurement of Chemiresistive Nanomaterials ..	46
3.2.1	Reduced Graphene Oxide .....	46
3.2.2	Carbon Nanotubes .....	48
3.2.3	Copper Oxide .....	49
3.3	Dielectrophoresis and Nanomaterial Assembly .....	53
Chapter 4:	Design and Modeling .....	57
4.1	First Order Electrical Model of DEP Assembly .....	57

4.1.1	Parallel Resistance .....	61
4.1.2	Nanomaterial Resistance.....	61
4.1.3	Contact Resistance .....	65
4.1.4	Capacitances .....	70
4.2	Model of Dielectrophoretic Assembly.....	57
Chapter 5:	Results.....	72
5.1	Test Setups .....	72
5.2	Measured Responses of Individual Gas Sensors .....	77
5.2.1	Reduced Graphene Oxide .....	77
5.2.2	Carbon Nanotubes.....	79
5.2.3	Copper Oxide .....	82
5.3	Electronic Nose Performance .....	86
Chapter 6:	Conclusions.....	90
6.1	Future Work .....	90
6.1.1	Sensor Mechanism .....	90
6.1.2	Greater Sensor Variety.....	91
6.1.3	Classification Algorithm Implementation.....	91
6.1.4	CMOS .....	91
Appendix I.	Printed Circuit Board Design.....	93
Appendix II.	LabView Interface .....	96
Appendix III.	Relevant MatLab Code .....	98

Chapter 7: References.....100

# Table of Figures

Figure 1- Representative diagram illustrating DEP assembly force [14] .....	9
Figure 2 – DEP versus fluid flow assembly of polyaniline nanowires. DEP assembly shown at top is marked by assembly only between electrodes, while fluid assembly below shows assembly around the entire perimeter of each electrode.....	13
Figure 3 - EOF (right) and ETF (left) induced flows in water with an ionic surfactant. Note the differing range and flow rates of each mechanism. In deionized water, EOF would be nearly negligible due to the lack of ions to form an electrolytic bilayer[18].....	14
Figure 4 - Spatially selective DEP assemblies in a 128*256 pixel array [30]. .....	16
Figure 5 - AFM image of a film of reduced graphene oxide platelets[63] .....	21
Figure 6 - The valence (blue) and conduction (red) band structure of graphene. Note the linear, conical shape around each Dirac point[64]. .....	23
Figure 7 – Illustration of the difference between the chiralities of metallic and semiconducting carbon nanotubes[70]. .....	24
Figure 8 - Wheatstone bridge circuit .....	30
Figure 9 - Difference amplifier .....	30
Figure 10 - Schematic representation of a neural network [88].....	34
Figure 11 - Example of iterative process of cluster analysis[89].....	35
Figure 12 - Illustration of the fabrication sequence of the electrode array for DEP assembly. The step numbers correspond to those in the following table, which outlines the fabrication process.....	39
Figure 13 - Mask design. Each chip has 40 assembly sites and 4 ground paths connected to the 44-pin pad frame. A grid of 35 test electrodes site in the center of the chip. The "M-3" in the legible in the inset stands for Multi-finger electrode with 3 $\mu$ m electrode spacing. For scale, the entire chip is 1cm x 1cm, and the pads in the inset are 200 $\mu$ m x 250 $\mu$ m.....	42

Figure 14 - Primary electrode geometries studied. A) Parallel electrodes B) Multi Finger Electrodes C) Single Finger Electrodes. In all cases, the gap is varied from 2 to 5 microns in increments of 1 micron. The assembly region is highlighted in red. ....	43
Figure 15 – Micrograph of Diced Chip.....	44
Figure 16 - Encapsulation and DEP Assembly Process. The electrode chip (1) is wirebonded in an LCC package. Epoxy is selectively placed over the wirebonds and not the electrode array by masking with an appropriately cut PDMS block (2). UV light is then used to cure the epoxy (3). This yields a selectively encapsulated chip as shown in (4), and allows for mechanical and chemically stability while performing DEP assembly (5).....	45
Figure 17 - Intermediate process steps of rGO synthesis (image courtesy of Manohar group) .....	46
Figure 18 - Heavily concentrated dispersion of carbon nanotubes. Generally, dispersion concentrations look like water .....	48
Figure 19 - SEM of AAO showing pore density and homogeneity.....	49
Figure 20 - Copper nanowire array viewed from an angle (above) and above (bottom).....	50
Figure 21 - EDS spectrum of copper oxide nanowire. The gold signature is from the electrode on which the nanowire rests. Although the quantitative analysis is notoriously inaccurate, this result does act as evidence that the nanowire is predominately CuO rather than Cu <sub>2</sub> O.....	51
Figure 22 - Fabrication sequence of copper oxide nanowires. ....	52
Figure 23 – Process flow of multi-material sequential integration of different nanomaterials. (1) A drop of SWNT dispersion is placed on chip and a voltage is applied to the appropriate electrode(s). The dispersion is blown off leaving a n assembly of SWNT’s (2) The same procedure is repeated for rGO at different electrode(s). (3) After repeating again for CuO, a heterogeneous array has been sequentially assembled with complete spatial selectivity. ....	54
Figure 24 - Parametric variation of assembly parameters and resultant resistances. NA stands for no measurable assembly. Note that this is a microscope image; the nanoscale DEP assemblies between the above electrodes cannot actually be discerned at this level of magnification. Each electrode pair is separated by approximately a millimeter.....	55

Figure 25 - Example of DEP assembly. CuO is assembled here. ....	56
Figure 26 - Relative DEP force observed for copper oxide in DI water, reduced graphene oxide in DMF, and single wall nanotubes in DI Water.....	58
Figure 27 - Cross section of DEP assembly with notable resistances: .....	60
Figure 28- Force per unit area of Van der Waals forces, electrostatic forces and capillary forces as a function of separation distance[134]. ....	66
Figure 29- Current pathways in metal-semiconductor assembly junction.....	70
Figure 30 - Picture of multiplexed gas sensor test board. The entire set up (excluding laptop) can easily be held in one hand. ....	73
Figure 31 - Simplified diagram of evaluation board operation.....	75
Figure 32 - IV curve of rGO DEP assembly showing non-linearity at low voltages. Higher potentials were used in testing to avoid responses in this regime. The kink observed at 2.1V is the result of range switching on the SourceMeter. ....	76
Figure 33 – False color SEM images of assembled rGO. Gold electrodes are demarcated by the gold coloring.....	78
Figure 34 – Typical response of single rGO gas sensor. The spikes at the end of each gas hump are due to mechanical vibrations caused by the introduction of the gas and are not artifacts of the sensing mechanism itself. The peaks correspond to (in order) Methanol, Methanol again, Ethanol, IPA, and the last one being acetone. The sharp spike observed after 2000 was caused by a loss of connection. ....	79
Figure 35 - SEM image of single wall carbon nanotube DEP assembly. Electrodes in false color gold.....	80
Figure 36 - Response of two separate SWNT DEP assemblies to simultaneous gas testing. Note the separate y-axis for each assembly. Despite being almost an order of magnitude different in resistance, the fractional changes in resistance are almost identical. ....	81
Figure 37- Bundled and single copper oxide nanowires assembled across DEP electrode. The nanowires exceed the 200nm pore diameter because the nanowires thicken during oxidation. ....	83
Figure 38 - Gas response of copper oxide to methanol, ethanol and acetone.....	85

Figure 39- Parallel output of heterogeneous gas sensor array. Green is rGO; red is CuO; Blue is SWNT's; Grey is ground pins. X-axis is time in minutes; Y-axis is resistance. The four visible responses correspond, in order, to Methanol, Acetone, IPA, and Ethanol.....	86
Figure 40 - Gas response to methanol, toluene and ammonia. ....	88

# Chapter 1: Introduction

## 1.1 Motivation

Sensors and transducers bridge the gap between the physical world and the electric realm, which are ever-increasingly fusing into one entity in modern society. As such, sensors are relied upon in nearly every aspect of everyday life from the automotive sensors that keep commuters safe on the road to the temperature sensors that keep people comfortable at home and work. With the rise of this digital world, so too has risen the need for technology to acquire, process, control, communicate, and output this vast system of sensor signals. Solid state circuitry, in particular, Complementary Metal Oxide Semiconductor (CMOS) technology, has become integral as the electrical backbone of most complex electronic systems. With transistor counts topping a billion per chip and clock speeds exceeding 1GHz, today's typical consumer may switch a billion transistors a billion times each over the course of a single day [1].

Because most sensor systems are tethered to CMOS chip for signal acquisition, processing, digitizing and, perhaps, transmission, there has become a growing trend of integrating sensors monolithically onto a CMOS die. This eliminates long and complex pathways between the sensing element and the chip and provides many advantages over conventional sensing set ups that are based on a remote sensor device with a potentially noisy transmission path back to a bulky board or system fabricated with off-the-shelf components. In particular,

integrated sensors allow for a reduction in cost, size, and complexity while potentially boosting the sensitivity of the sensor. Integrating sensing elements into or onto the semiconductor substrate results in profound miniaturization, which is critical for embedded biomedical devices and mobile devices where there are tight size constraints. This integration also removes the need for interconnects and interfaces (wires, adapters, printed circuits, etc.) between the CMOS processing center of the system and the sensor itself. This network of pathways can be complex, adding to the design and materials costs of the system. Furthermore, placing the sensing element directly on chip drastically mitigates parasitic losses in signal lines. This leads to potential gains in sensitivity.

The trend of integrating sensors with CMOS has been enabled by the rise of MEMS (micro-electromechanical systems) sensors, whose fabrication processes mimic those of semiconductor foundries. The nearly complete compatibility of the two fabrication processes provided a simple path for integrated CMOS-MEMS sensors. This first major mass market application of this technology was introduced by Analog Devices with their introduction of CMOS-MEMS accelerometers and, later, microphones[2]. CMOS substrates also lend themselves to optical sensing due to the compatibility of silicon's band gap with the visible spectrum. With the reduction of feature sizes over the past decade, CMOS image sensors have moved to compete with charge-coupled devices with respect to speed and pixel size. Now, CMOS image sensors are the method of choice in many imaging applications from high-end digital cameras to the miniature cameras found in mobile phones[3]. CMOS cameras demonstrate the

ability of CMOS to function as a platform for the massively parallel operation and readout of many sensing elements (in this case, pixels or photodiodes).

It should be noted that CMOS sensors have progressed to far outperform of their human counterparts. Modern CMOS image sensors outstrip the human eye in terms of dynamic range, resolution and frame rate; Analog Devices' microphones feature a far wider bandwidth than the human ear; and CMOS-MEMS accelerometers and gyroscopes rival the equilibrium abilities of the inner ear [4-6]. Indeed, CMOS sensors have eclipsed their biological equivalents in nearly every realm. However, the ability of the human nose to distinguish, identify and quantify over 10,000 odors has not been rivaled on any platform, including CMOS[7].

The key to the sensitivity and selectivity of biological olfactory systems is an array of hundreds of different chemoreceptors, which transmit neurological impulses to the brain upon interaction with certain gas species or odorants[8]. This scheme is intriguing in that these chemoreceptors are cross-reactive. That is, each kind of chemoreceptor is sensitive to a broad set of odorants, and these sensitivity sets can be widely overlapping between any two types of chemoreceptors. It is unclear how the human brain processes these interfering and conflated signals, but it has been shown that every distinguishable odor creates a unique chemotopic map in the brain[9]. Detection of odor by brain parallels Principle Component Analysis (PCA), a method commonly use to extract useful data from cross-reactive arrays of gas sensitive elements[10].

The need for a human nose on chip is ubiquitous and critical. Safety and olfactory fatigue limit the utility of people to detect odors. Innately, humans cannot monitor an odorant for an extended period of time because a phenomenon known as olfactory fatigue will cause our brains to subconsciously filter out the scent over time. Thus, a person cannot be relied upon for continuous odor monitoring. Also, there are some vapors and environments which are unsuitable for humans. The detection of noxious gases and detection in extreme environments are two examples where humans cannot be relied upon for vapor detection. Furthermore, current gas sensors are generally designed to detect a single odorant (e.g. smoke detectors), but many settings require the detection and identification of many target analytes. For example, toxic gas alarms should be able to detect all harmful gases in the environment. Often, it is impractical to install gas sensors for every potential target; these situations illustrate the necessity of electronic noses. Applications of an electronic nose include quality assurance in the food service and preparation industry, security, medical patient monitoring, process monitoring, environmental safety and hygiene, and pollution monitoring.

Why has the implementation of an ‘electronic nose’ or ‘e-nose’ on CMOS not been forthcoming? While the processing capabilities of CMOS allow for facile implementation of sensor arrays on chip (e.g. megapixel CMOS image sensors), the materials used in a CMOS foundry are not particularly reactive to gases, let alone cross-reactive. Thus, to create an electrical analog of the human nose on CMOS, more processing steps are needed to include gas sensitive elements.

However, in the ‘top-down’ methodology of CMOS fabrication (to be discussed later), each type sensor element to be added considerably raises the overhead both for expense and time. The natural inclination is to explore ‘bottom-up’ assembly strategies as an alternative method to fabricate a cross-reactive array of gas sensors. Bottom-up fabrication methods rely on the use nanoscale or molecular properties to assemble devices rather than large macroscale tools to form patterns layer-by-layer one material at a time. Bottom-up methodologies are much more amenable to the massively parallel fabrication of many individual and not necessarily identical devices.

There are many types of gas sensors including optical, quartz crystal microbalance, gas chromatography, surface acoustic wave, and electrochemical methods, but perhaps the most easily implemented gas sensors are chemiresistors[11]. As the name suggests, chemiresistors are a class of materials whose resistivity changes upon interaction with certain gas species. Many nanomaterials, such as carbon nanotubes, graphene nano-platelets and nanowires, are especially sensitive chemiresistors because interactions at the surface more greatly affect volume of these materials as a whole. Chemiresistive nanomaterials are also amenable for integration with CMOS due to their scale: realizing a gas chromatography set up on silicon, for example, would be challenging to say the least.

There are many assembly methods for integration of nanomaterials onto silicon including drop casting, Langmuir-Blodgett assembly, direct printing, and

in situ growth. An ideal assembly process would fulfill the following requirements:

- **Massively parallel:** The process should be able to assemble many sensors at once.
- **Compatible:** The process needs to work for a broad range of nanomaterials.
- **Reliable and repeatable:** There should be consistency in assembly between runs.
- **Controllable:** There needs to be both spatial (assemble only at the desired sites) and quantitative (control over the amount and, therefore, resistance of the sensor) control.

Based on these requirements, a prime assembly mechanism candidate emerges in dielectrophoresis, a versatile assembly method based on the motion of polarizable particle relative to a non-uniform electric field in an a dielectric medium[12]. As will be discussed in the ensuing section, dielectrophoresis allows for precise placement and alignment of nearly any nanomaterial, regardless of its physical or electric properties.

Thus, the combination of the processing power of CMOS, the versatile assembly capabilities of dielectrophoresis, and the sensitivity of chemiresistive nanomaterials creates an ideal platform for gas sensing. Presented in this thesis is the CMOS-compatible fabrication and assembly process to transform CMOS dies into fully integrated electronic nose. Exemplary gas sensing properties of carbon based nanomaterials such as carbon nanotubes and reduced graphene oxide, along

with a relatively novel metal oxide nanowire in copper oxide, will be utilized in these implementations.

# Chapter 2: **Background**

In this chapter, gas sensing technologies and their role in creating an electronic nose will be reviewed. The progression from an individual gas sensor to a heterogeneous array of sensors with olfaction ability will be outlined. A brief overview of fabrications methodologies available to accomplish this task will be outlined. Also included is a discussion on the sensor electronics back end and the classification algorithms that assimilate the multitude of individual gas sensor outputs into a single gas identification.

## 2.1 **Bottom Up vs. Top Down Fabrication**

Top down fabrication utilizes the sequential patterning of many layers to realize the desired structure, while bottom-up processes involve the ordered clustering of small units such as atoms, molecules, or nanomaterials into useful structures. Each methodology has advantages and disadvantages. Bottom up fabrications processes are not always versatile in terms of materials and can be limited in their patterning ability. However, they also tend to be cheaper, quicker, and more easily implemented at the nanoscale. Top down methods are nearly synonymous with lithographic techniques. Lithography suffers from high mask costs, scaling issues at the nanoscale, and laborious fabrication processes. However, lithography has become the technique of choice for most micro and nanofabrication operations because it is well-characterized, exceptionally versatile, and high throughput[13]. This work utilizes both top-down and bottom-

up methods: CMOS dies are perhaps the most advanced example of top down manufacturing, here being used as an electro-active substrate for the bottom-up assembly of nanomaterials to serve as integrated gas sensors.

### 2.1.1 Theory of Dielectrophoresis

The mechanism of dielectrophoresis is illustrated in Figure 1

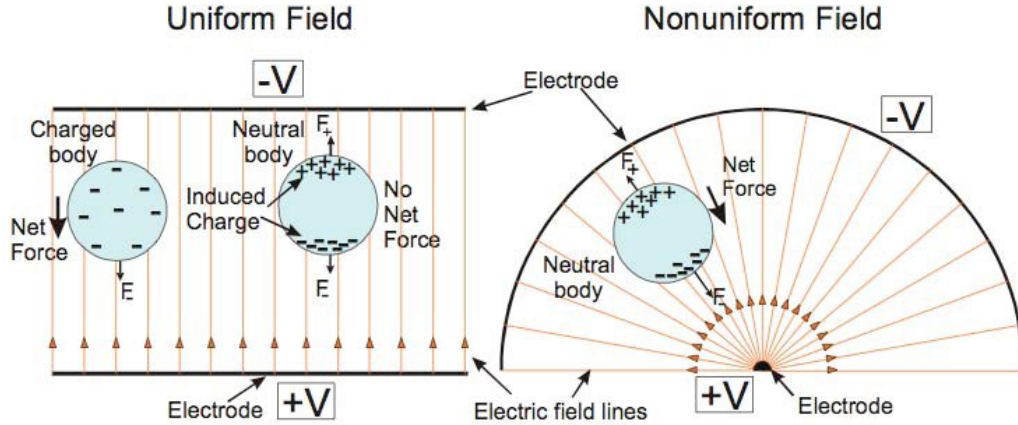


Figure 1- Representative diagram illustrating DEP assembly force [14]

Neutral, polarizable particles suspended in a dielectric medium tend to experience a force along the steepest gradient of an applied electric field. A force towards the region of greatest electric field is known as positive DEP (or pDEP), while the converse is negative DEP (nDEP). This motion can be described by the following equations:

$$F \propto aK(\omega)\nabla|E^2| \quad 2-1$$

$$K(\omega) = \frac{\epsilon_p^* - \epsilon_m^*}{3(\epsilon_m^* + (\epsilon_p^* - \epsilon_m^*)L)} \quad 2-2$$

$$\epsilon_x^* = \epsilon_x - j\omega\sigma_x \quad 2-3$$

where  $a$  is a constant dependant on the geometry of the particle,  $E$  is the applied electric field,  $\omega$  is the frequency of the applied field, and  $K(\omega)$  is the Clausius-Mossotti factor. This is dependent on  $L$ , which deals with the polarizability of the

particle along different dimensions, and the complex permittivities of the particle and medium ( $\epsilon_p^*$  and  $\epsilon_m^*$ , respectively). The polarization factor,  $L$ , causes the Clausius-Mossotti factor to be very different depending on the geometry of the particle. The complex permittivities are in turn dependent on the frequency, as well as the conductivity ( $\sigma$ ) and dielectric constant ( $\epsilon$ ) of the particle or medium[15, 16]. Furthermore, dielectric constants are a misnomer because they do vary with frequency. For a rigorous evaluation of the Clausius-Mossotti relation, one must be careful to use the correct permittivity for any given frequency.

As illustrated by equations 2-1-3, the dielectrophoretic force experienced by a given particle in a certain medium is a function of frequency and electric field. Thus, the force, and thereby degree, of assembly can be modulated by adjusting the applied field and its frequency. The field relation is a simple square relationship: doubling the applied voltage gradient will quadruple the experienced force. Less clear is the frequency dependence, which is entirely a function of the Clausius-Mossotti factor. Due to polarization effects, this factor has a strong dependence on the geometry of the particle. This arises from the polarization factor in the general Clausius-Mossotti given in Equation 2-2. The analysis is further complicated by torques experienced by particles. For example, nanowires and nanotubes experience a torque such that they align themselves perpendicular to the applied field. This renders the DEP forces due to the charge accumulation on the short axes insignificant. The Clausius-Mossotti relation for the most

common nanomaterial geometries is given in Table 1[17]. The derivation of these relations is beyond the scope of this work.

Sphere	$K(\omega) = \frac{\varepsilon_p^* - \varepsilon_m^*}{\varepsilon_p^* + 2\varepsilon_m^*}$	2-4
Prolate Ellipsoid (e.g. nanowire)	$K(\omega) \cong \frac{\varepsilon_p^* - \varepsilon_m^*}{3\varepsilon_m^*}$	2-5
Disc / Platelet	$K(\omega) \cong \frac{\varepsilon_p^* - \varepsilon_m^*}{3\varepsilon_p^*}$	2-6

**Table 1 – Clausius-Mossotti factors for common nanomaterial geometries**

A second critical insight into the mechanism of DEP is also gained from the Clausius-Mossotti factor. The sign of the equation 2-7<sup>1</sup>, derived from the Clausius-Mossotti factor, conveys the direction of the DEP force: positive indicates pDEP, while negative indicates the opposite.

$$\omega^2(\sigma_m - \sigma_p)\sigma_m - (\varepsilon_p - \varepsilon_m)\varepsilon_m \quad 2-7$$

This holds only for prolate ellipsoid particles such as carbon nanotubes and nanowires, but similar expressions can be derived for other geometries. In this work and in general, the permittivity of the medium exceeds that of the particle, and the conductivity of the particle is greater than that of the medium. As such, the pDEP is generally observed at low frequencies, and nDEP is observed at high

---

<sup>1</sup> This equation is derived by taking the real part of the full Clausius-Mossotti factor. That is, only the real parts of the complex permittivities are accounted for and the quotient is evaluated. The resulting denominator is omitted as it is always positive.

frequencies. The cut-off frequency occurs when the expression given by equation 2-7 is equal to 0<sup>2</sup>.

It should be noted that many other electro-hydrodynamic kinetic effects (both as a result of the applied field and otherwise) influence any dielectrophoretic assembly. While DEP is generally the dominating force in the vicinity of the electrode, many other phenomena including, but not limited to, Brownian motion, electro-osmotic effects, and electrothermal flow [16, 18]. These (electro) hydrodynamic effects can very much alter the efficacy of DEP assembly and are discussed in more detail.

- **Brownian motion:** Brownian motion is the stochastic “jittering” of a particle due to collisions with atoms or molecules of a fluid medium. The motion is described by a Gaussian random walk. In the context of DEP assembly, Brownian motion has the effect to spread the region of assembly. This effect is especially pronounced in concentrated dispersions and with smaller particles. This effect is temperature dependent; lowering the temperature mitigates Brownian motion.
- **Electro-osmosis:** Electroosmotic flow (EOF) arises from an electrolytic bilayer formed in fluid medium. Mobile ions experience an average force over time in the direction parallel to the electric field and tangential to the electric double layer. The effect generally is only

---

<sup>2</sup> It is possible that there exists no real solution. In this case, only pDEP or nDEP is observed across the entire frequency spectrum.

significant a few microns from the electrode perimeter. This flow can cause spurious assembly around the perimeter of electrode sites as shown in Figure 2. This process can be moderated by using exceptionally deionized dispersion mediums and high frequencies (>100kHz). In such conditions, the electrolytic bilayer is less

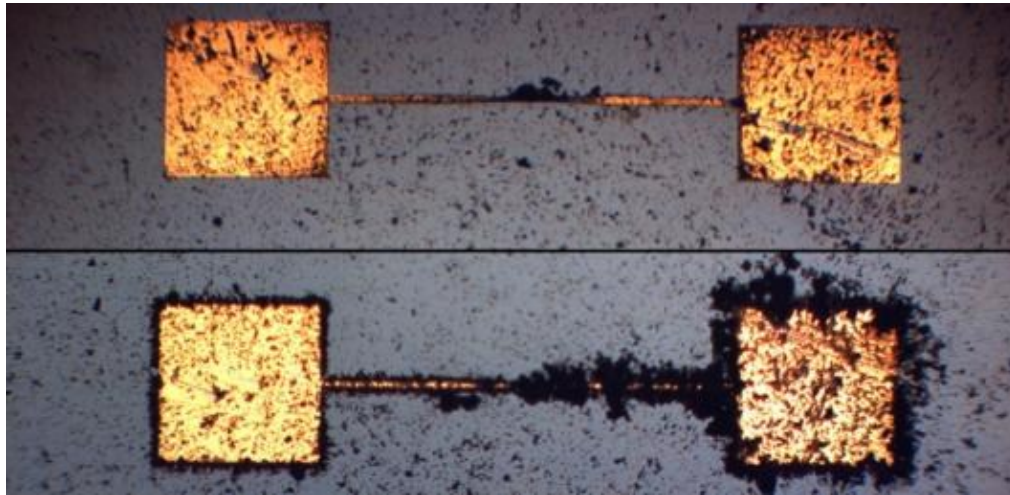


**Figure 2 – Polyaniline nanowire assemblies serving to illustrate the difference between fluid flow assembly and dielectrophoretic assembly. DEP assembly shown at top is marked by assembly only between electrodes, while fluid assembly below shows assembly around the entire perimeter of each electrode.**

pronounced[19].

- **Electrothermal Flow:** Joule heating of the medium in which DEP assembly is being performed creates temperature gradients, which in turn create a body flow (electrothermal flow, or ETF) of fluid along this gradient. This effect can extend tens of microns from the electrode gap. ETF is an extremely important aspect of any DEP assembly, although it is often unrecognized as a factor. While DEP is the primary force acting on particles in the immediate vicinity of an electrode gap (within microns), ETF is the primary mechanism for

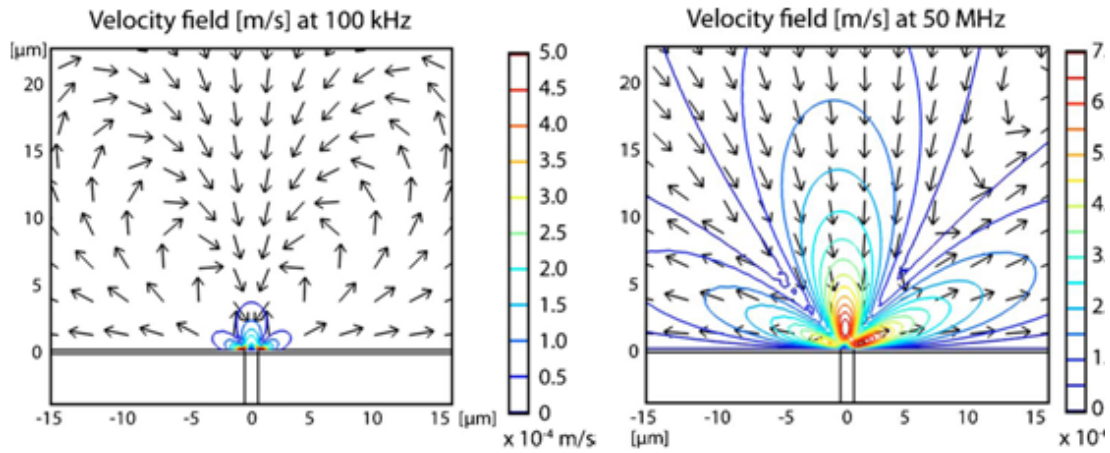


**Figure 3 - EOF (right) and ETF (left) induced flows in water with an ionic surfactant. Note the differing range and flow rates of each mechanism. In deionized water, EOF would be nearly negligible due to the lack of ions to form an electrolytic bilayer[18].**

particles to enter this vicinity. ETF provides a constant stream of dispersion past the electrode. Without this flow, DEP assembly would be strongly attenuated. As it is driven by joule heating, increasing the assembly voltage also increases the ETF. Thus, increasing the voltage has a dramatic effect on assembly because the DEP force is proportional to the square of the applied field, and the ETF is increased linearly, as well. In the frequency range used in the work, ETF generally grows with frequency as the resistance seen across the electrode gap becomes more prominent than the reactance (i.e. more power is dissipated as heat than stored in the electric field as the frequency is increased). As with EOF, in extremely concentrated solutions, ETF may cause some spurious assembly around the perimeter of the electrode sites.

### 2.1.2 Dielectrophoresis as a Means of Assembly

Dielectrophoresis has long been used as a means of nano- and microscale bottom-up assembly. DEP has been employed to assemble and/or separate biological cells, polymers, microbeads, nanoparticles, DNA and many other similarly scaled objects [20-23]. Devices made via dielectrophoretic assembly include gas sensors, dielectrophoretic tweezers, field emitters, interconnects, transistors and a wide range of bio-sensors [20, 24-29]. Virtually any particle may be controlled via DEP, and, as such, a great variety of devices fabricated using DEP have been developed.

However, although DEP has the capability of creating heterogeneous arrays of diverse materials, this application of DEP is conspicuously absent from the literature. This ability is derived from the extreme spatial resolution of DEP. Because assembly only occurs at the electrode(s) where a potential is applied, sequential DEP assemblies of different materials can be executed at different electrodes or regions of electrodes across an entire substrate without any intermediate steps. This functionality allows the creation of heterogeneous arrays for selective gas sensing employed in this work and detailed in the fabrication section of this thesis.

Dielectrophoresis has also been used to integrate unique materials onto CMOS. Early work by Evoy and Mayer shows the viability of DEP as a means to



**Figure 4 - Spatially selective DEP assemblies in a 128\*256 pixel array [30].**

wed CMOS substrates with functional materials [31, 32]. Dielectrophoresis has been used to assemble the functional element of sensors on CMOS dies[33]. In terms of sensor arrays, a DEP platform for array-based DEP analysis for bio-assay applications has been reported by Enteshari et al.; however, it was not intended for the use as a heterogeneous sensor array[34]. A similar effort by Hunt et al. allowed for the selective assembly of droplets and cells on an array of  $128 \times 256$  pixels stretching across a  $4\text{mm}^2$  area[30]. DEP has even been used to assemble gas sensors on CMOS chips; however, the use of DEP to create a heterogeneous array of sensors on CMOS is still forthcoming[15].

### **2.1.3 Other Assembly Methods**

There exist several other bottom-up assembly methods; however, none matches dielectrophoresis in spatial controllability and ease of implementation. A

non-comprehensive selection of some of the more popular bottom-up methodologies is detailed here.

a) ***Dropcasting / Dip-Coating***

Perhaps the simplest form of self-assembly; drop casting or dip coating is performed by allowing the solvent of a nanomaterial dispersion to evaporate on a substrate. The remaining nanomaterials form a thin film. Dip coating can be made spatially selective by using surface modification of the substrate (hydrophobic vs. hydrophilic) such that the dispersion only covers the appropriate sections of the substrate. Alternatively, areas of the substrate may be masked by a sacrificial layer. However, these pre-deposition patterning steps are generally top down operations, which go against the advantages of using bottom-up processing in the first place. This method has been used to make patterned films of two of the materials used in this work: graphene and carbon nanotubes [35-37].

b) ***Langmuir-Blodgett Assembly***

Langmuir-Blodgett assembly is, in essence, a form of dip coating. The surface onto which the nanomaterial is to be assembled is dipped in a trough of an appropriate dispersion. Due to the surface chemical interactions between the substrate and the dispersing medium, a thin film of the nanomaterial is deposited as the substrate is removed from the liquid. There is no spatial selectivity beyond that the film will only adhere where the appropriate surface exists. While Langmuir-Blodgett assembly is an excellent and facile method to create atomically thin films, there are many constraints on the dispersing medium and assembly surface [38-40].

### c) *Inkjet Printing*

A popular top-down methodology, ink jet printing can be applied to dispersions of nanomaterials to raster print patterns of nanomaterial films. The spatial resolution is limited to tens of microns or larger depending on the dispersing medium. Inkjet printing has a huge advantage in that almost anything can be printed; there are very few material restrictions. Gas sensing devices have been inkjet printed from carbon nanotube, graphene and conducting polymers [41, 42]. The two main drawbacks to ink jet printing are alignment and speed. Aligning the print head to underlying features can be challenging, and the overall throughput of inkjet printing is slow as the printer must mechanically scan through the entire pattern [43].

### d) *In-situ Growth*

Finally, in particular cases, nanomaterials can be grown in situ. This technique varies depending on the material to be grown and the substrate. However, the process can be very spatially selective, growing only where a catalyst or electrode exists. The temperature, chemical environment, and pressure must be compatible with the substrate. An example of in situ growth is the chemical vapor deposition of carbon nanotubes (which only grow at catalyzed points on the substrate). Electrochemical polymerization can also be used to grow polymer-based sensors at electrodes. In situ growth does lend itself to the facile integration of a broad selection of materials and should be considered as an alternative to assembly [44-47].

## 2.2 Chemiresistive Sensors

Due to their relative simplicity, chemiresistive materials have long been used for gas sensors. Three common types of chemiresistors will be discussed in detail: metal oxide, carbon and conductive polymer. The former represents the most commonly found gas sensors on the market. Carbon and polymer chemiresistors are the two most active areas of current chemiresistors research.

### 2.2.1 Metal Oxide Chemiresistors

Metal oxide gas sensors are the most common gas sensors. In particular, the Taguchi tin dioxide gas sensor has found use both in civil and military environments, including many of the residential carbon monoxide alarms that some states require in every home. These gas sensors rely on changes of the surface resistivity of thin SnO<sub>2</sub> filaments[48]. Other metal oxides, notably zinc oxide (ZnO), are also sensitive to gaseous species[49].

The general mechanism of metal oxide semiconducting gas sensors is a change surface resistivity in the presence of redox reaction agents. Reducing agents are prone to giving up electrons, which are injected into the conduction band of the metal oxide semiconductor. This raises the conductivity. Conversely, oxidizing gas species raise the resistance of the sensor by robbing charge carriers from the conduction band. Other factors such as grain size, contact material, and, most significantly, temperature affect the response of the sensor. Metal oxide chemiresistors generally operate between 200°C and 400°C. In this range, there is enough activation energy to initiate the redox reaction, but not too many thermally generated charge carriers to bury the response of the sensor[50]. In

nanoscale materials, these temperatures can easily be achieved with modest bias currents. As with all semiconductors, incident photons as well as temperature affect the number of charge carriers and conductivity of metal oxides. As such these variables must be controlled or monitored so that their effects are not confused with chemical responses.

In this work, copper oxide has been chosen to be evaluated for its efficacy as a nanoscale chemiresistor. While tin oxide sensors are the predominant metal oxide sensor, they are implemented on a scale that is order of magnitudes large (hundreds of microns rather than nanometers).

a) ***Copper Oxide***

Copper oxide has long garnered research attention for its superconductive properties (alloyed, at cryogenic temperatures), but only recently has it found renewed interest as a sensor material[51]. Copper oxide can be used as a catalytic surface (especially when nano-structured) for solution-based sensing[52, 53]. For gas phase detection, copper oxide is most often used as a dopant or small alloy constituent to a tin oxide based sensor [54-56]. However, copper oxide itself has been shown to be sensitive to many vapor species including oxygen, formaldehyde, ethanol, nitrous oxide, hydrogen sulfide, and other various hydrocarbons [57-60].

In this work, the functionality of copper oxide as a gas sensor is evaluated. As previously stated, the power of a heterogeneous sensor array for machine olfaction is derived from diversity. This diversity can be achieved by the addition

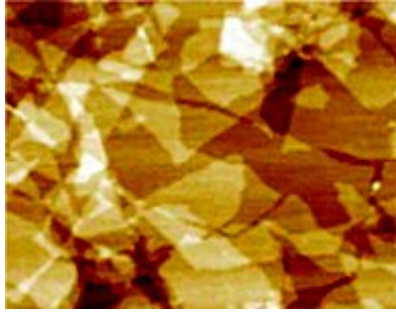


**Figure 5 - AFM image of a film of reduced graphene oxide platelets[63]**  
of copper oxide to a heterogeneous array of more common chemiresistive metal oxide such as SnO<sub>2</sub> or ZnO. As such, copper oxide

### 2.2.2 Carbon Chemiresistors

#### a) *Graphene*

The advent of carbon nanotubes and graphene in the past three decades has opened up a new set of materials for exceptionally sensitive gas sensors. The electronic properties of a single atomic monolayer of graphite (graphene) have long been known, but it was thought that the synthesis of such a structure was impossible[61]. The successful isolation of single layers of graphene by Geim et al. has paved the way for many investigations into graphene and graphene-like structures for gas sensing applications[62].

Graphene's electron band structure boasts two very unique features: First, pure, single layer of graphene is a zero band gap material, also known as a semimetal. This means that the conduction band touches the valence band at a point known as the Dirac point. Any amount of energy can excite an electron from the valence to the conduction band. Second, the energy versus momentum relationship in the vicinity of the Dirac point is linear, rather than the typically-observed quadratic. This translates to exceptionally high electron and hole

mobilities[64]. Adding additional graphite layers, introducing impurities, or spatially constraining the electrons at the quantum level can open up the bandgap, making graphene into a semiconductor.

While there are many desirable electronic properties of pure graphene, chemically graphene is rather inert[65]. The chemical activity of graphene is highest at the dangling bonds that exist at edges of flakes or at impurities within the graphene plane[66]. Chemically derived graphene through the chemical reduction of graphene oxide platelets finds a balance between the non-insulating nature of graphene and the chemical activity of graphene oxide. The chemical activity is due to oxygen-containing impurity sites of alcohols, epoxides and carboxyl groups[63, 67]. These impurities actually act as binding sites for gas molecules, increasing the interaction response. Thus, ‘lower’ quality graphene from an electronics standpoint is actually higher quality graphene from a sensors point of view[68, 69].

#### b) *Carbon Nanotubes*

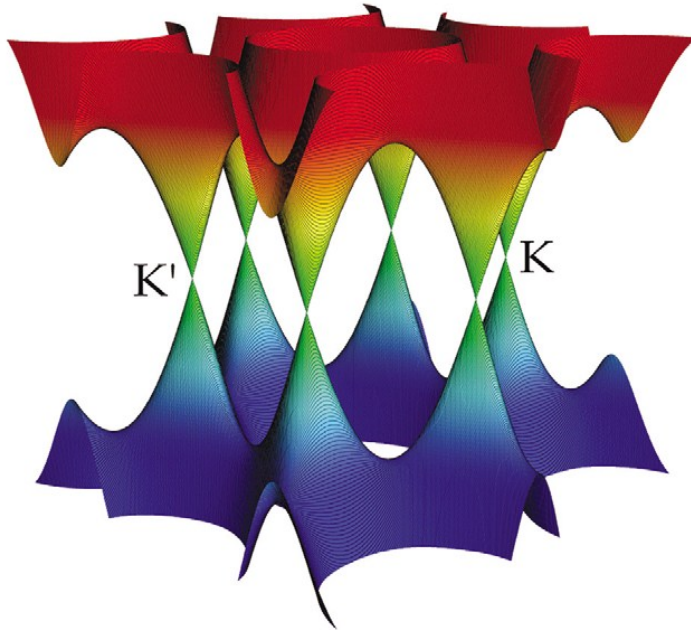


**Figure 6 - The valence (blue) and conduction (red) band structure of graphene. Note the linear, conical shape around each Dirac point[64].**

Rolling up a sheet of graphene yields a carbon nanotube. Like graphene, these 1-dimensional materials span the border between metals and semiconductors. The electrical behavior of a carbon nanotube is defined by its chirality, the lattice orientation along which the carbon nanotube is rolled (see Figure 7).

As with graphene, carbon nanotubes come in single layer and multi layer varieties. Multi-wall nanotubes (MWNT) have many concentric tubes, while a single atomic layer defines single wall nanotubes (SWNTs). MWNT's always behave like metals, while SNWT's can behave like either metals or semiconductors. In this work, SWNTs are primarily investigated for their gas sensing potential.

The mechanism of chemoresistance for carbon-based gas sensors is the same as that of metal oxide sensors. That is, gas species can either contribute or take electrons from the conduction band of semiconducting graphene or carbon nanotubes. However, due to the extreme dimensions of these materials, other factors come into play such as quantum confinement of the charge carriers, one- or two-dimensional current pathways. However, of particular interest for sensing application is the exceptionally high surface to volume ratio: all the atoms in the materials are at the surface, and thus are able to be intimately affected by the environment. Because these materials are only one atom in thickness, gaseous species interacting at the surface can affect the electron band diagram of the material as a whole. This vastly changes the electrical characteristics. Fractional changes in resistance exceeding three orders of magnitude have been observed in these materials [71].

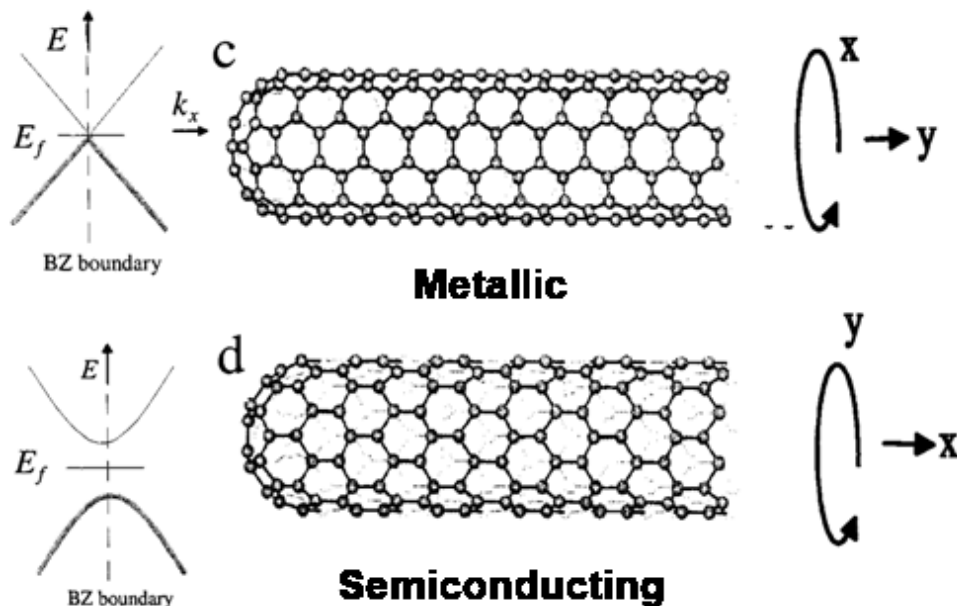


Figure 7 – Illustration of the difference between the chiralities of metallic and semiconducting carbon nanotubes[70].

### 2.2.3 Conductive Polymer Chemiresistors

The third common variety of gas sensors are conductive polymers. The most popular polymers for this application are polyaniline and polypyrrole [72]. These two polymer families have been used for olfaction application since the late 1980's [73]. Many other polymers also find use as gas sensors including, but not limited to: poly(p-phenylene azomethine), polythiophene, poly(phenyl vinylene) and poly(3,4-ethylene-dioxythiophene) [24, 74, 75]. Due to this variety, polymers make a good candidate for components of a heterogeneous sensor array for electronic nose applications.

Conductive polymers do not display the high resistivities generally associated with polymers due to alternating single and double bonds, which serve to delocalize electrons in neighboring  $\pi$  orbitals. This leads to an energy gap between the highest occupied state in one  $\pi$  band and the lowest unoccupied state in the other. This energy gap is typical of insulators and semiconductors. The polymer is turned into an electrically metallic state by doping; much the same as a degenerately doped semiconductor is effectively a metal. In the conductive polymers, doping is generally achieved by the introduction of anions along the back bone of the polymer chain. Incidentally, these dopant atoms also serve as efficient binding points for gas analytes[76].

Conductive polymer chemiresistors function similarly to the previously detailed semiconducting chemiresistors. Gas analytes participate in redox reactions, which serve to increase or decrease the number of charge carriers in the polymer. Unlike carbon and metal oxide chemiresistors, inert gas species can

modulate the conductivity of polymers by deforming the polymer chain upon binding with it. Conductive polymers also differ from other varieties of chemiresistors in that they are more permeable to vapors. This means that the full response to a gas species may come much after its introduction as the vapor diffuses into the bulk. Because volatile species take time to desorb from the polymer, the sensor also has memory (meaning previous sensing events can affect the present state of the gas sensor). Lastly, it should be noted that doping has a huge effect on the performance of conductive polymer gas sensors. Certain dopant atoms/ions provide binding sites to particular analytes; dopant atoms are directly related to the conductivity of the polymer; and, without dopants, conductive polymers can be fundamentally instable. Thus, when working with conductive polymers, the doping material and procedures often dictate the performance of the sensor as a whole[77].

### 2.3 Other Gas Sensing Mechanisms

It should be noted that many other gas sensing mechanisms exist and their popularity is based on the applications. For completeness sake, some of the most common will be mentioned briefly, and their advantages and disadvantages as compared with chemiresistors will be commented upon.

- **Gas chromatography:** Gas chromatography utilizes the different transit times of gas through a constrictive medium called a stationary phase. This stationary phase may be a solid, liquid or simply a capillary. Depending on the interaction forces between the gas molecule and the stationary phase, the transit time through this

medium will vary. A highly sensitive and multi-specie detector is used at the back end of the stationary phase recording the transit time from which different odors may be identified[78]. There are two main issues with gas chromatography: First, the sensor is only as sensitive as the back end detector for any given analyte. Second, transit time is not a strictly unique identifier for a given analyte. As such, gas chromatography units are generally paired with a more powerful back end detector, and transit time is used as a secondary vector for the identification of an introduced analyte. It should be noted, however, that gas chromatography is amenable to miniaturization with on-chip implementations existing for decades[79].

- **Mass Spectrometry:** Mass spectrometry operates on the principle of the separation of ionic species of the same velocity as they travel through a magnetic field. Gas species must be ionized before they are accelerated through a velocity selector. This separates ions spatially by mass such that an array of ion detectors can create a histogram of ions by mass. Alternatively a quadrupole-based mass spectrometer can be used to separate ions in temporally by mass, and a single sensor can record incident charge as a function of time[11]. This method is extremely selective as it yields exact information of a physical property of the gas molecule (molecular weight). It can also be very sensitive, detecting ions in parts per billion concentrations. However, due to the complexity of the set up, it is a very intractable problem to

miniaturize the system. Therefore it is often used as an analytical tool in laboratories, often in conjunction with a gas chromatograph.

- **Acoustic Wave Devices:** Gas species can be detected by minute amounts of gas species absorbed onto a surface by observing the change in the natural frequency of a resonator. This resonator can be a micro-cantilever or a quartz crystal microbalance [80, 81]. As with chemiresistors, these sensors can be fabricated on the micro-scale and placed in arrays to allow for selectivity. Further, selectivity can be achieved by coating subsets of the array with thin films that bind with certain kinds of analytes. However, these methods can suffer from low sensitivity.

- **Optical Methods**

Fluorescence and

- **GasFETs:** Gas sensitive field effect transistors are an extremely sensitive and nanoscale option for electronic nose applications. The sensing mechanism of these sensors occurs at the gate where gas interactions either introduce charge onto the gate or modify the work function of the gate material. This either changes the conductance across the channel or the turn-on voltage of the transistor. Because the sensing mechanism occurs at the gate of the transistor, there is an inherent amplification of signal in line with the transconductance of the transistor. GasFETs also have the inherent advantage of being electrical in nature, meaning that no transduction is necessary to

transfer the information into the electrical domain for data acquisition and processing. Selectivity can be achieved by utilizing different gate materials. However, selectivity is difficult to achieve on a single die because integrating transistors with different gate materials across a single die involves a huge increase in fabrication complexity[82].

## 2.4 Sensor Electronics

Perhaps the greatest advantage of chemiresistors is the fact that their mode of operation is already in the electrical domain. This eliminates the need for a transduction stage to transfer sensor information into a readable form for the sensor back end. However, even though the sensor data is in the electrical domain, it is not necessarily amenable to acquisition and measurement. Therefore, some sort of sense electronics should be used to condition the signal prior to acquisition.

### 2.4.1 Wheatstone Bridge

The classical approach to resistive sensors utilizes a Wheatstone bridge (shown in Figure 8) to allow for the facile detection of minute changes in resistance. The voltage,  $V_g$ , seen across the bridge is equal to:

$$V_g = V_{Source} \left( \frac{R_4}{R_3 + R_4} + \frac{R_2}{R_1 + R_2} \right) \quad 2-8$$

For small changes in a balanced bridge:

$$\Delta V_g \cong V_{Source} \left( \frac{\Delta R}{\kappa R} \right) \quad 2-9$$

As shown above the change in  $V_g$  for a balanced bridge (meaning that, initially  $R_1/R_2 = R_3/R_4$ ) is equal to the relation given in Equation 2-9 (where  $\kappa$  is a

proportionality constant no less than 4). In this manner, fractional changes in resistance of any of the four resistors in the bridge can easily be transferred into the voltage domain. The subtraction of the baseline resistance is not even necessary. The method is further attractive because it is easy to bias the resistor at whatever value necessary.

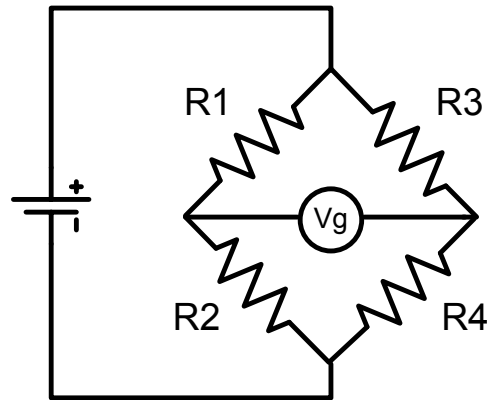


Figure 8 - Wheatstone bridge circuit

### 2.4.2 Instrumentation / Operational Amplifiers

Instrumentation amplifiers provide an active method to condition signals. There are many ways to configure amplifiers amongst other components to achieve various functions such as filtering, amplifying or summing. The following topology, the difference amplifier, is presented out of applicability[83].

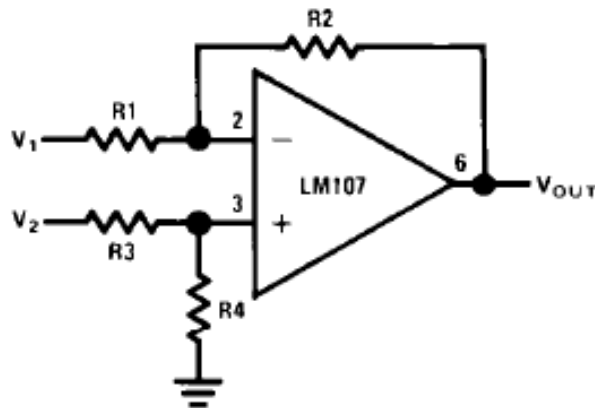


Figure 9 - Difference amplifier

The output voltage can be shown to be given by Equation 2-10. When inserting the chemiresistor as  $R_1$ , appropriate choices of resistors  $R_{2-4}$  will not only cancel the baseline voltage, but also result in significant differential amplification. While this works very well for a single chemiresistor, the resistor values have to be tailored to the individual chemiresistor. Thus, a single difference amplifier will not function adequately for an entire array without programmable companion resistors. Such a circuit very feasibly implemented in CMOS.

$$V_{out} = \left( \frac{R_1 + R_2}{R_3 + R_4} \right) \frac{R_4}{R_1} V_2 - \frac{R_2}{R_1} V_1 \quad 2-10$$

In addition, this circuit or a similar variation can be used to read out the voltage from a Wheatstone bridge. One is welcome to look at several other interface circuits based on whether the sensor output is voltage or current or charge. A more comprehensive review can be found here[84].

### 2.4.3 Analog to Digital Conversion

A final option is to convert the data to the digital domain. While a simple level shifter, gain element and low-pass filter may be needed to match the input range for the analog-to-digital convertor (ADC), all other necessary filtering and data conditioning operations can take place in the digital domain. As long as the quantization levels are small enough to not lose any information due to sampling, this allows for the most straightforward manipulation and acquisition of data. Several architectures are popular for analog to digital conversion for sensor signals. The frequency content of most sensors for applications, such as in gas sensing or biomedical diagnostics, will be in the DC- kHz range. The resolution

requirement for sensor signal digitization typically depends on the SNR and could range in moderate to high resolution range of 12-20 bits. The ADC architectures suitable for such specifications are Delta-Sigma converters and Successive approximation converters. More basic information on these architectures can be found here[85].

## 2.5 **Signal Processing**

The processing and interpretation of signals generated by a heterogeneous gas sensor array often dictates the sensitivity and selectivity of the olfaction process. For example, although the interaction cross section of the chemoreceptors of the human nose is miniscule compared to some electronic gas sensors, millions of years of evolution have made the processing power of the brain so advanced that human olfaction outmatches any electronic nose in many respects. Tomography of brain activity during olfaction tests has shown that certain odors excite certain regions of the brain[86]. This mapping operation is a recurring theme throughout many processing algorithms that strive to transform sensor data to useful chemical environment information.

Several algorithms have been put forward as methods to interpret sensor data from heterogeneous gas sensor arrays. Some of the more common methods will be discussed in detail.

### 2.5.1 **Support vector machines**

Support vector machines (SVM) are the simplest form of machine learning to classify data. It is primarily a binary algorithm to distinguish between two classes, but can be modified to distinguish between many classes simply by

making the multi-classification problem into many sequential binary classifications. Given a set of  $n$ -dimensional training data with classifications, an SVM algorithm creates an  $(n-1)$ -dimensional hyperplane that most adequately divides the space such that only data of one class lies on each side of the plane. In two dimensions, this would be analogous to a line separating two clusters of data. Points fed into the SVM will then be classified based on which side of the line they fall upon[87].

### 2.5.2 Artificial Neural Networks

Artificial neural networks aim to classify data sets by creating layers of nodes with weighted interconnections between each layer. This seeks to emulate the neuron and axon connection in the human brain. The input to the nodes is data acquired from the sensor(s). The output nodes are the different observable classifications. Any given set of data fed through the network will be weighted through the connections resulting in one of the outputs having a greater score than the rest. This output should correspond to the correct class. The training of a neural network is computationally complex, involving iterative processing to find the correct weights to put at each interconnection[88]. It should be noted that the interconnections can feedback between layers of nodes. In this way, neural networks resemble Markov chains. This allows for neural networks to easily account for the memory effects that are present in some chemiresistors; a trait not shared by other classification algorithms.

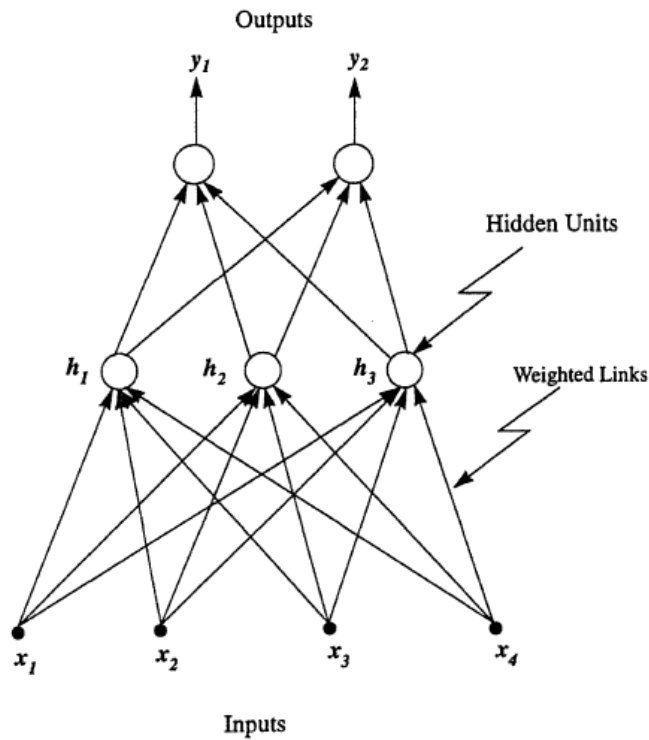
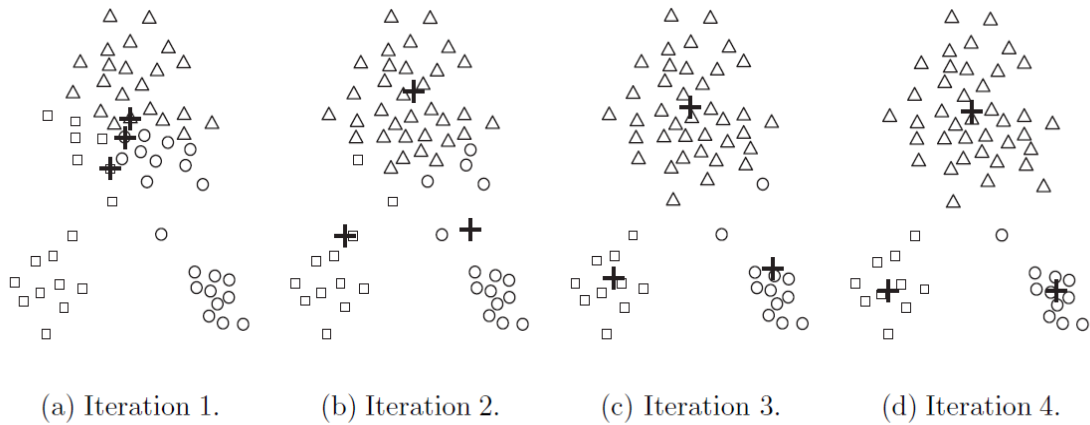


Figure 10 - Schematic representation of a neural network [88]

### 2.5.3 Cluster Analysis

Cluster analysis is the subdividing data points into clusters that should each include only one class of data. Cluster analysis operates on the principle that mean distance between the centroid of a cluster and each data point in that cluster is minimized. In general, this is an iterative procedure. There are varying methods to define the geometric centroid of a cluster and measuring the distance between point and centroid (e.g. Euclidean distance or maximum norm), so there are many flavors of cluster analysis that exist. These versions vary in convergence time and accuracy, but represent the simplest method of data classification [89, 90].



**Figure 11 - Example of iterative process of cluster analysis[89]**

### 2.5.4 Principle component analysis

From a least squares error perspective, principle component analysis (PCA) should yield the most accurate classifications for gas species. PCA can be viewed as an advanced form SVM classification. In PCA, the data is first run through an algorithm such that the variance of the data is maximized. This eliminates any redundancy in the data set that can mask patterns. The data is then replotted in the n-dimensional space where there exists the greatest variance. The axes of this space are the ‘principle components’ of the data set. At this point, dimensions with low variance (high redundancy) can be ignored to simplify the problem by projecting the data set into a lower dimension. In general, PCA can be viewed as tightening the clusters of separate classes of data. Once this data processing is finished, one of the aforementioned algorithms such as cluster analysis or a SVM may be used to classify the data[10, 91].

## 2.6 Electronic Nose

There is a great difference between a conventional gas sensor and an electronic nose. While the former is typically designed to detect a single analyte

without any response to other gases, the latter must not only respond to as many analytes as possible, but also identify them. Furthermore, an ideal E-Nose could perceive the concentration of the detected analyte.

The difficulty in implementing an E-Nose arises in that it must be greater than the sum of its parts. It would be impossible to create an individual gas sensor for every possible analyte and integrate them all into a single device. Therefore, an electronic nose must function as the human olfaction system introduced in the previous chapter. It must rely on a diverse array of broadly cross-reactive sensors. One of the aforementioned classification algorithms may be used to process the data from the array of gas sensors and intuit the gas environment. Thus, a true olfaction machine must have all the components introduced in this chapter: an array of sensing elements (chemiresistive or other), a platform to integrate the sensors on, sensor electronics to acquire and process the sensor data, and a classification algorithm to convert the sensor data into useful gas environment information.

### **2.6.1 E-Nose Implementations**

Many E-Noses have been implemented through the aforementioned methods. Arrays of functionalized quartz crystal microbalances have achieved selectivity in an electronic nose [92]. Optical methods have also been explored, exploiting arrays of cross-reactive, fluorescing microbeads to generate a chemotopic map unique to a given gas[93]. Heterogeneous chemiresistor arrays have been fabricated using standard top-down techniques with neural networks or PCA analysis to achieve selectivity [94-97].

While all of these sensing apparatuses could be used to create an electronic nose, the creation of heterogeneous array of chemiresistors via dielectrophoresis is the most facile method of creating a both cross-reactive and sensitive sensor array on CMOS. It also should be noted that these electronic noses generally only take advantage of one type of sensing element or chemiresistor (e.g. metal oxide or conducting polymer). This is a direct result of the limited versatility of the fabrication means. In this way, DEP truly excels, being easily adaptable for the assembly of conductive polymers, carbon nanostructures, metal oxide nanowires and other nanoscale chemiresistors.

# Chapter 3: **Fabrication**

The fabrication of the presented electronic nose is multi-step process involving both top-down and bottom-up fabrication methodologies. The fabrication consists of three steps: first, the patterning of the silicon wafer with gold electrodes; second, the fabrication of the nanomaterials themselves that will eventually become chemiresistors; and, third, DEP assembly of the nanomaterials on the silicon substrate, thereby integrating the products of the first two steps. Each of these processes will be detailed in the following chapter.

## 3.1 **Silicon Electrode Array Photolithographic Fabrication**

The first step in creating gas sensors was to create a platform on which to assemble the chemiresistive elements. This was accomplished using the standard CMOS-compatible top-down fabrication methods.

### 3.1.1 **Photolithography**

Standard photolithographic procedures were used to define the electrode patterns for DEP assembly of gas micro-sensors on silicon. The silicon wafer serves as little more than a planar surface for subsequent lithographic steps. Therefore, test grade wafers procured from Nova Electronic Materials (Flower Mound, TX) were chosen as the most economical substrate. The fabrication steps including important process parameters are summarized in **Error! Reference source not found.** and illustrated in Figure 12.

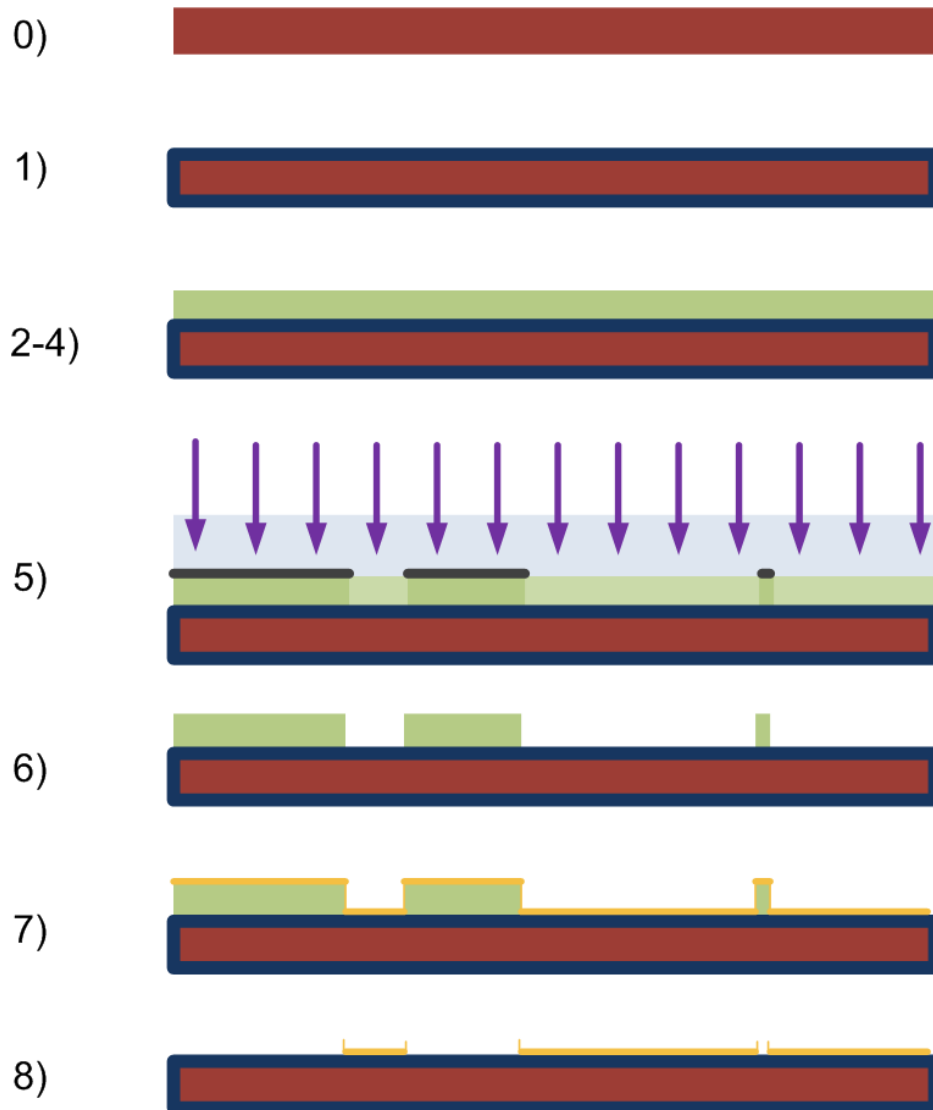


**Figure 12 - Illustration of the fabrication sequence of the electrode array for DEP assembly. The step numbers correspond to those in the following table, which outlines the fabrication process.**

1	Thermal Oxidation	1050°C for 2 hours plus heating/cooling time
2	Spin HMDS	3500RPM for 30s
3	Spin S1813 PR	3500RPM for 30s
4	Soft Bake	115°C for 1 minute
5	Expose	2.3s at 60mW/cm <sup>2</sup>
6	Develop	1:45 in MF CD 26 Metal Ion Free Developer
7	Sputter	Evaporate
		Metallization, generally about 200nm of metal
8	Liftoff	Ultrasonication

**Table 2 - Summarized fabrication steps for lithographic patterning**

The first fabrication step was the thermal oxidation of the silicon wafer. This creates an oxide layer on the surface of the wafer that serves to electrically isolate the DEP electrodes. This was achieved by two hours (not including heating and cooling times) of thermal oxidation in a Thermolyne 47900 muffle furnace (Thermo Fisher Scientific, Waltham, MA) at 1050°C in the ambient air atmosphere. This produces a very uniform ( $\pm 10\%$ ) silicon dioxide film. However, the average thickness of this film varied from 70 to 130 nanometers from run to run. The wide range of thicknesses can be explained primarily by the variations in the humidity of the environment and also variable heating and cooling times due to changes in the ambient temperature. The absolute thickness of this oxide layer is of no importance as long as the open circuit resistance seen across the fabricated electrodes is many orders of magnitude greater than that of the DEP assembly. As discussed in the following chapter, bulk resistivity

generally far exceeds surface resistivity in these dimensions. Typical open circuit resistances exceeded one gigaohm, well above observed chemoresistances, which agrees with the expected value of conductivity as given by the model presented in section 2.1.1.

With the SiO<sub>2</sub> film, standard lithographic procedures to pattern electrode sites can commence. First, the wafer is inspected for cleanliness. If necessary, the wafer is sonicated in DI water and/or, in the case of organic residue, rinsed with a sequence of acetone, isopropyl alcohol, and, lastly water. The silicon wafer is then put in a Laurell WS-400B-6NPP-LITE spinner for the application of adhesion promoter and photoresist. Hexamethyldisilazane (HMDS) is used as an adhesion promoter for Shipley S1813 photoresist. A mixture of 80% PM acetate and 20% HMDS is spun onto the wafer at 3500RPM, allowing it to spin and evaporate off. This modifies the surface of the wafer through a process known as silylation, which leaves dangling siloxane functional groups for photoresist to bond to. Furthermore, HMDS is an effective desiccating agent and helps remove water from the surface of the wafer. This improves wettability of the surface for better performance during development[98].

### 3.1.2 Mask Design

In order to fabricate the gas sensors, a mask needed to be designed and made to perform the photolithographic process to create the electrode array for DEP assembly. The mask design contained several 1cm by 1cm chips, each containing different electrode geometry and spacings as outlined in Section 3.1.2. An example chip layout is shown in Figure 13.

Each chip is designed to fit in a 44-pin leadless chip carrier package with an open cavity. Of the forty four pads in the pad frame, forty are connected to one electrode of a DEP assembly. The other sides of these forty electrodes are shorted together and connected to four ground pads (for redundancy). In addition to these forty assembly sites, a five by seven array of 35 isolated assembly sites exist in the center of the chip. These may only be accessed by probing and serve as test assembly sites. These sites are used to fine tune DEP conditions before assembling on the main sites connected to the pad frame.

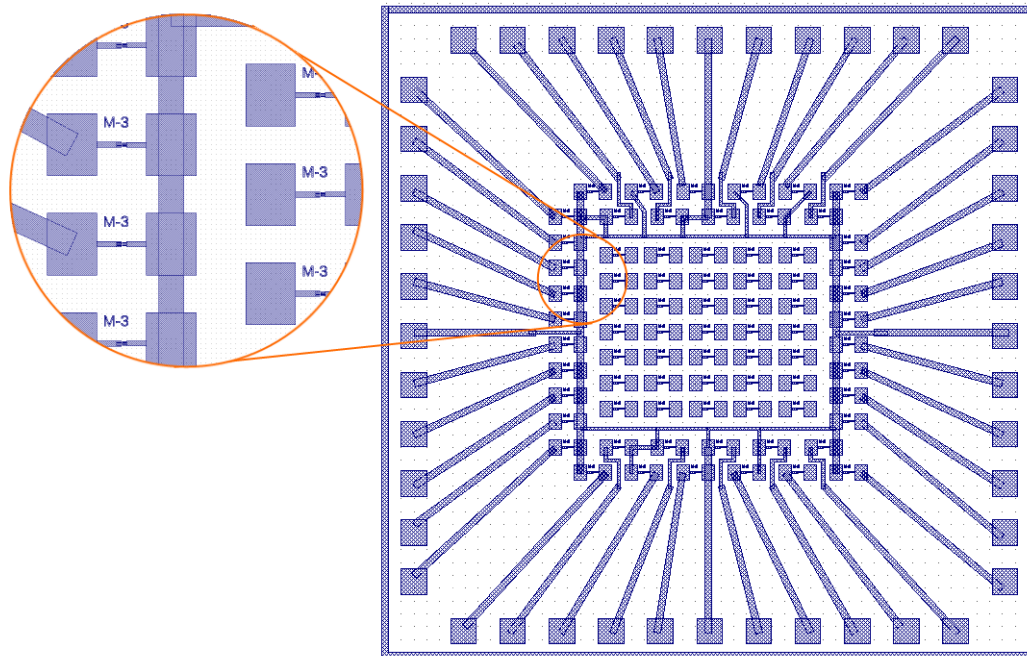


**Figure 13 - Mask design.** Each chip has 40 assembly sites and 4 ground paths connected to the 44-pin pad frame. A grid of 35 test electrodes site in the center of the chip. The "M-3" in the legible in the inset stands for Multi-finger electrode with 3µm electrode spacing. For scale, the entire chip is 1cm x 1cm, and the pads in the inset are 200µm x 250µm

The mask was ordered from Advanced Reproduction Inc. (Andover, MA).  
The mask itself was a 5" soda lime glass patterned with chrome.

### 3.1.3 Electrode Geometries

Three electrode geometries were studied in particular (shown in Figure 14). In each case, the inter-electrode distance was varied from two to five microns. This spacing corresponds to the dimensions of the nanomaterials used which do not generally exceed  $10\mu\text{m}$  in their greatest dimension. First, shown in Figure 14.a, is two parallel electrodes sharing a long length. Due to the extreme shared length of electrode, DEP assemblies across this pattern were expected to be of extremely low relative resistance. Conversely, in the ‘single-finger’ electrode design, shown in Figure 14.c, the small assembly area was designed to result in high resistances and frequently. The ‘multi-finger’ design, shown in Figure 14.b, was designed as a compromise between the single-finger and parallel electrode geometries.

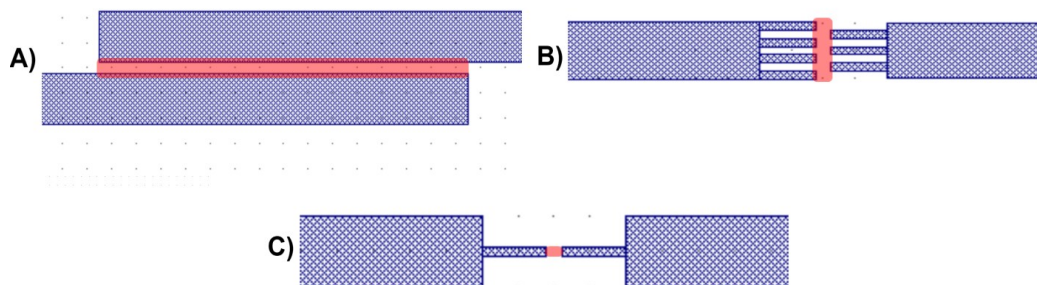


**Figure 14 - Primary electrode geometries studied. A) Parallel electrodes B) Multi Finger Electrodes C) Single Finger Electrodes. In all cases, the gap is varied from 2 to 5 microns in increments of 1 micron. The assembly region is highlighted in red.**

### 3.1.4 Packaging

Many aspects of the packaging operation (UV light, ultrasonic vibration and heat) can damage DEP-assembled chemiresistive sensors. Therefore, it is necessary to complete the packaging steps prior to DEP. The first step is to separate the wafer into chips. This can be accomplished by dicing (precise) or

scribing (crude and quick). Dicing uses a circular saw with a diamond blade (Micro Automation MA1006) to perform carefully camera-aligned cuts across the substrate. Alternatively, a diamond tip scribe can be used to score a wafer along an appropriate crystallographic orientation. The wafer can then be cloven along the drawn scribe line. A picture of a scribed wafer is shown in Figure 15.

To integrate the chip into a chip carrier, wirebonding is used. This process combines thermal and ultrasonic energy to thermosonically bond thin (1mils diameter) gold wire between the gold pads on the die to the gold-plated pads of the chip carrier. Packaging prior to assembly also circumvents the need for a probe station to apply the input signals necessary for DEP. Probing is time- and energy-intensive and limits throughput. However, much as the packaging operation can be harsh on the DEP assemblies, so too can the DEP assembly process can be harsh on packaged chips. It is customary to encapsulate wirebonds in epoxy to ensure their integrity. This is especially important for chips

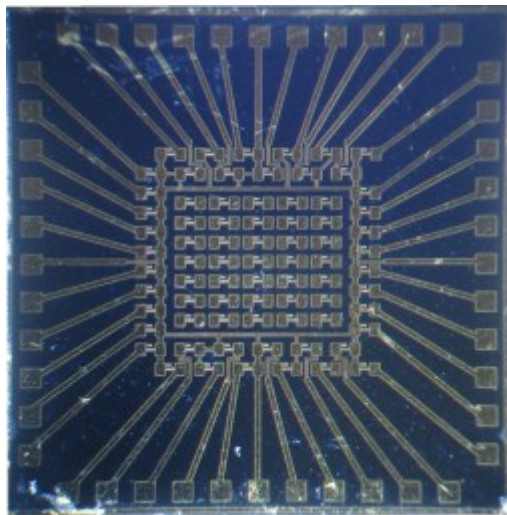


**Figure 15 – Micrograph of Diced Chip**

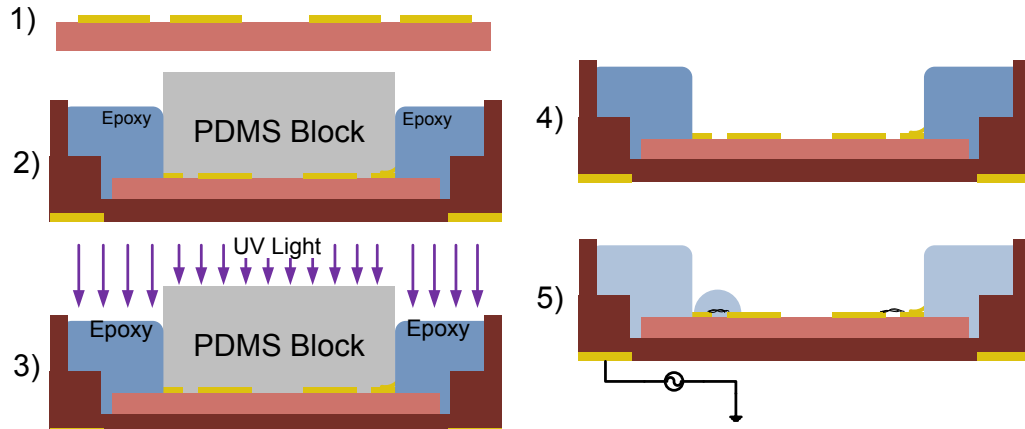


**Figure 16 - Encapsulation and DEP Assembly Process.** The electrode chip (1) is wirebonded in an LCC package. Epoxy is selectively placed over the wirebonds and not the electrode array by masking with an appropriately cut PDMS block (2). UV light is then used to cure the epoxy (3). This yields a selectively encapsulated chip as shown in (4), and allows for mechanical and chemical stability while performing DEP assembly (5).

undergoing DEP assembly because the combination of applied voltage, an aqueous medium and application of compressed air is a difficult environment for wirebonds to withstand. Even the capillary force of water droplets drying between wirebonds can be sufficient to disconnect delicate wedge bonds. The chip must only be partially encapsulated because the electrodes must be left open to allow for assembly and subsequent interaction with gas molecules. Partial encapsulation is achieved by covering the central region of the chip with an appropriately cut piece of PDMS and filling the rest of the chip cavity with UV or heat curable epoxy. The PDMS block is manually placed with tweezers, and the natural adhesion between the silicon and PDMS maintains a tight seal throughout the process. The epoxy is then cured utilizing a UV curing oven, and the PDMS removed. This leaves the wirebonds encapsulated and central, gas-sensing region exposed as illustrated in Figure 16. Subsequent moderate power oxygen plasma cleaning is generally performed to ensure the complete removal of residue from the chip's exposed area.

## 3.2 Fabrication / Procurement of Chemiresistive Nanomaterials

### 3.2.1 Reduced Graphene Oxide

There are a few methods of creating graphene. The highest quality graphene is actually produced by the ‘Scotch-Tape’ method, which involves the exfoliation with Scotch tape of single layers of graphene from pyrolytic graphite[62]. Another popular method for creating large areas of graphene is through the sublimation of silicon from the top layers of a silicon carbide wafer. The remaining carbon can form a graphene sheet [99]. High quality graphene can also be produced by CVD on catalytic surfaces such as copper or nickel [100]. However, we used a chemical procedure to produce lower electronic quality, high impurity, multi-layer graphene sheets. As mentioned in Chapter 2, this economical fabrication method results graphene that is better for gas sensing than the inert counterparts produced in other methods.

The synthesis of rGO used in this work was carried out by Professor Sanjeev Manohar’s group at UMass Lowell. The process is an evolution of the Hummer’s method[101]. In brief and in general, the process involves oxidizing graphite

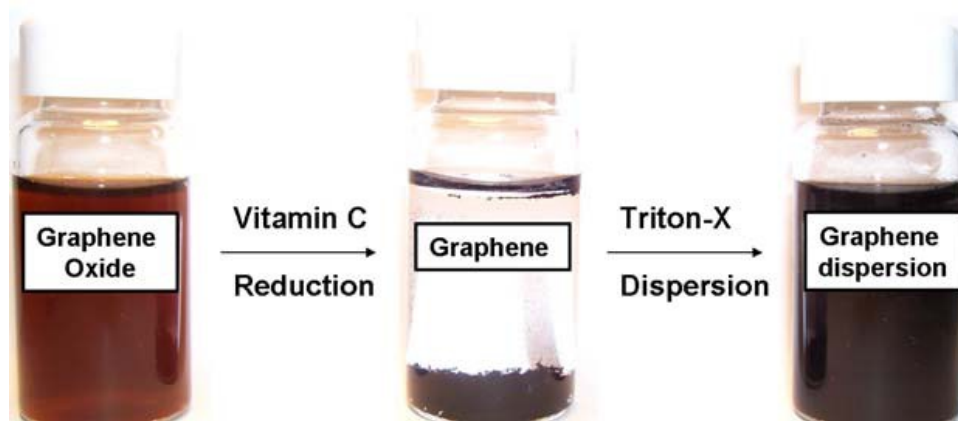


Figure 17 - Intermediate process steps of rGO synthesis (image courtesy of Manohar group)

(thermally or chemically) and then chemically reducing the resultant graphene oxide to make graphene. The oxidation only occurs at the surface of the graphite, causing surface stress and platelets to peel off. These platelets will go on to become graphene flakes, once reduced.

The synthesis of graphene oxide begins with graphite nanoplatelets. Two grams of these platelets and one gram of sodium nitrate are added to 50mL of concentrated sulfuric acid and stirred. Six grams of solid potassium permanganate is added slowly while the solution temperature is kept to under 10°C by an ice bath. After the solution has risen to 35°C in a warm water bath, water is added causing a vigorous exothermic reaction. After the reaction has been driven to completion, the solution is further diluted and hydrogen peroxide is used to convert the unreacted  $\text{KMnO}_4$  and  $\text{MnO}_2$  to soluble  $\text{MnSO}_4$ . The solution is then brought to a neutral pH and dried in a vacuum oven. This results in a bright yellow graphene oxide (GO) powder.

To convert the graphene oxide into reduced graphene oxide, 15mg of GO is added to 5ml of deionized water, to which 1ml of hydrazine monohydrate is added as a reducing agent. Alternatively, ascorbic acid (vitamin C) may be used as a safer and more environmentally-friendly substitute. The solution is heated to around 80°C for one hour. The resultant rGO is rinsed repeatedly by alternating cycles of centrifugation and reimmersion in DI water. The rGO can be dispersed in DMF in quantities of ~1mg/ml without the need for a surfactant to achieve dispersion. Surfactants are avoided as they increase the conductivity of the solution; thereby invalidating the assembly model presented in Chapter 2.

### 3.2.2 Carbon Nanotubes

The carbon nanotubes used in this study were procured from Unidym, Inc. (Sunnyvale, CA) and Helix Material Solutions (Richardson, TX). The carbon nanotubes from Unidym were created using a high pressure vapor phase deposition using a catalyst and carbon monoxide, while the Helix nanotubes were synthesized by a chemical vapor deposition technique.

The Unidym process, generally abbreviate HiPCO for High Pressure Carbon Monoxide, is entirely a gaseous deposition. First, iron pentacarbonyl ( $\text{Fe}(\text{CO})_5$ ) is allowed into the system, which deposits an iron catalyst on the substrate. The chamber is elevated to a pressure of 30atm and temperature of  $1050^\circ\text{C}$ . At these conditions the following reaction occurs at the iron nucleation points resulting in carbon nanotubes.



This results in high yield and high purity carbon nanotubes[102].

In addition to the HiPCO method, there are dozens of other CVD recipes for the synthesis of SWNT's using organometallic precursors (ferrocene, iron oxide)



**Figure 18 - Heavily concentrated dispersion of carbon nanotubes. Generally, dispersion concentrations look like water.**

to make nucleation sites and various organic compounds at the carbon feedstock, primarily methane, [103-105]. Two other main synthesis means are via laser vaporization and by creating arc discharges between graphite plates. The pulsed laser deposition operates on the principle of vaporizing bulk carbon doped with metal atoms to act as nucleation points for SWNTs and can yield small amounts of modestly pure SWNTs[106]. The arc discharge method has the least pure yield, but also is the least costly[107, 108].

### 3.2.3 Copper Oxide

The fabrication steps for making copper oxide nanowires are shown in Figure 22. This process is completed entirely in the Tufts Micro- and Nano- Fabrication Facility that is a class-1000 clean room. The procedure for creating nanowires through anodic alumina membranes is widely used for a variety of materials, including copper oxides [109, 110]. Anodic alumina oxide templates are

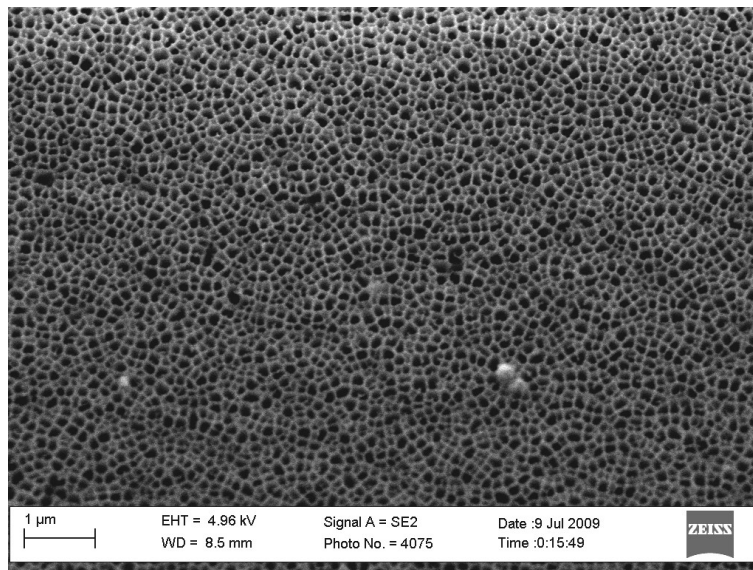


**Figure 19 - SEM of AAO showing pore density and homogeneity**

membranes with pores penetrating through the entire membrane. The porosity is exceptionally high (up to  $10^{10}/\text{cm}^2$ ), and every pore is of a similar diameter depending on anodizing conditions. Pore sizes can range from tens of nanometers to microns.

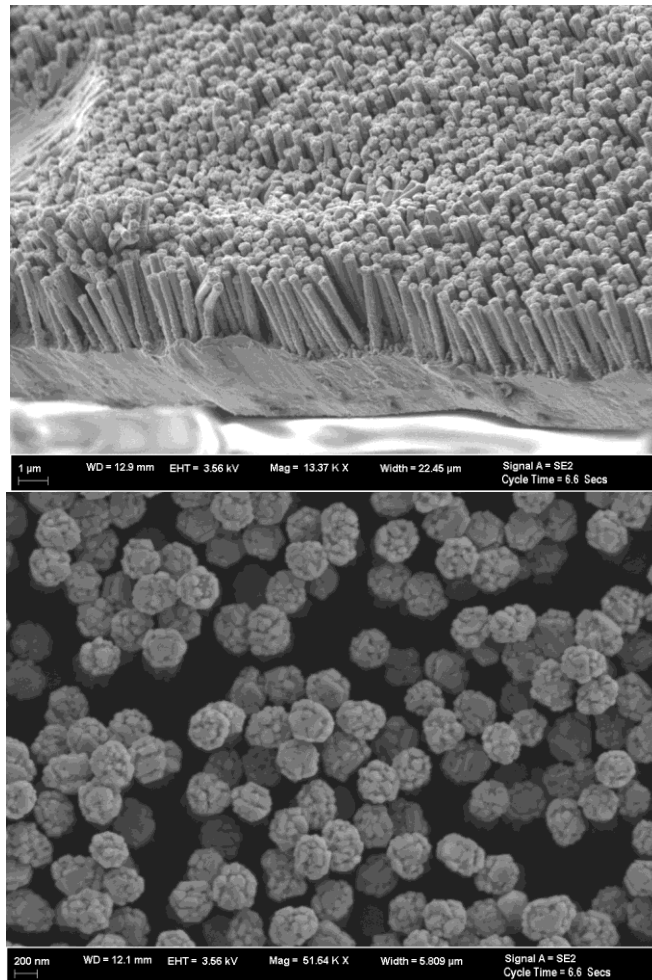
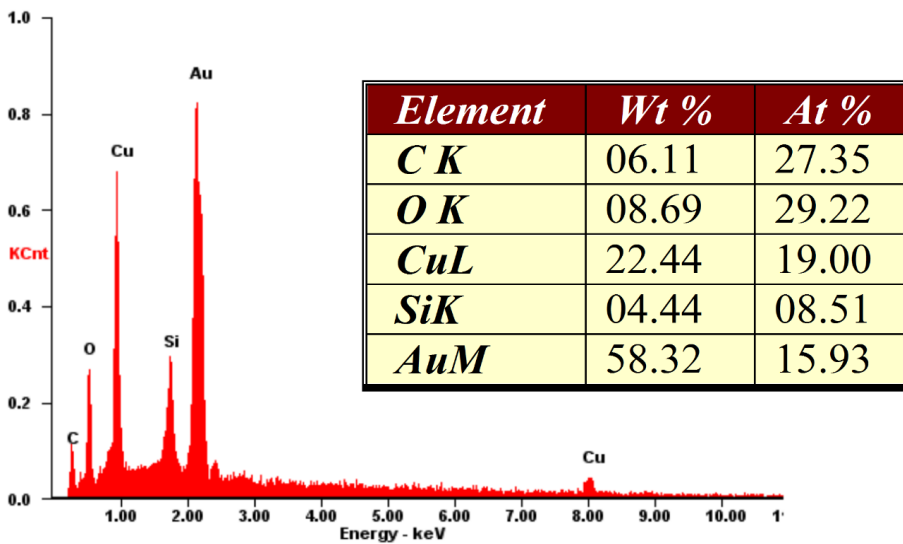


Figure 20 - Copper nanowire array viewed from an angle (above) and above (bottom).

In a typical procedure, a commercial AAO is coated on one side with 200nm of silver via sputtering. Next a clip is used to maintain electrical connection to the silver film while the membrane is immersed in a copper electroplating solution. The electroplating solution is a commercially available copper sulfate acid plating

bath available from Technic, Inc. (Cranston, RI)[111]. A current density of  $5\text{mA}/\text{cm}^2$  is applied. This value is kept low to increase the microscopic throwing power of the solution. If it were higher, the plating would occur inadequately at the bottom of the pores of the AAO. The nanowires grow in the pores at a rate of approximately  $100\text{nm}/\text{min}$ . After the nanowires are of a sufficient length (generally  $5\mu\text{m}$  or 50 minutes of plating), the AAO is removed from the plating solution and rinsed thoroughly. Then, the AAO is dissolved in a 15% potassium hydroxide (KOH) solution, leaving a freestanding nanowire array as shown in Figure 20. The array is rinsed thoroughly to remove any residual KOH. Next, the



**Figure 21 - EDS spectrum of copper oxide nanowire. The gold signature is from the electrode on which the nanowire rests. Although the quantitative analysis is notoriously inaccurate, this result does act as evidence that the nanowire is predominately CuO rather than  $\text{Cu}_2\text{O}$ .**

nanowires are thermally oxidized in an air environment at  $350^\circ\text{C}$  for 3 hours in a muffle furnace to completely oxidize the copper to copper oxide. The energy-dispersive X-ray spectroscopy profile of a copper oxide nanowire is shown in Figure 21. The release from the substrate can be accomplished in two ways: the silver seed layer can be etched selectively in a 5:1:1 solution of DI water,

hydrogen peroxide, and ammonium hydroxide, respectively. The easier method is to simply sonicate the nanowire array in water, which mechanically and effectively detaches the nanowires from the substrate. This leaves the nanowires dispersed in solution and ready for DEP assembly or dilution.

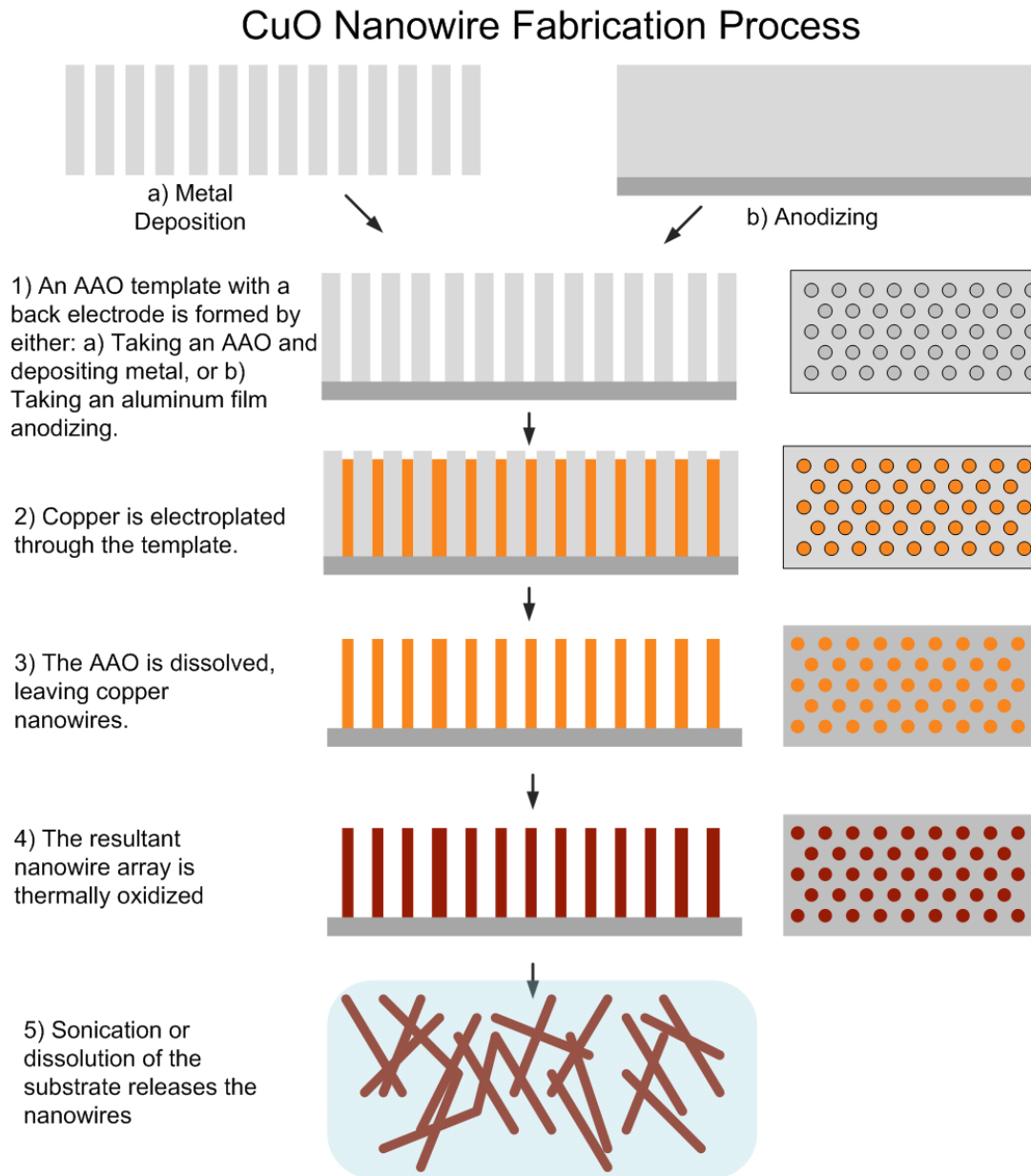


Figure 22 - Fabrication sequence of copper oxide nanowires.

### 3.3 Dielectrophoresis and Nanomaterial Assembly

Dielectrophoretic assembly is the final and easiest step of fabrication. The desired nanomaterial is dispersed in an appropriate dielectric medium by probe and/or bath sonication for several minutes. Once a dispersion is made; it can last several months, even years, before needing to be restocked. Only occasional sonication is needed to re-disperse the particles. To assemble, the AC voltage signal is applied across the electrodes with a function generator. Then, using a syringe, approximately 50 $\mu$ l of the dispersion is applied over the electrode. The dispersion is allowed to sit for 1-5 minutes, before being blown from the substrate with compressed dry air. The voltage source is then turned off. Typical assembly parameters of the nanomaterials used in this work are given in Table 3 – DEP

<b>Material</b>	<b>Medium</b>	<b>Dispersion concentration</b>	<b>Assembly Voltage</b>	<b>Assembly Frequency</b>
Carbon Nanotubes	DI Water	$\approx$ 5mg/ml	5V	1MHz- 10 MHz
Reduced Graphene Oxide	DMF	$\approx$ 1mg/ml	5V	100kHz- 500kHz
Copper Oxide	DI Water	$\approx$ 50 $\mu$ g/ml	5V	50kHz-500kHz

**Table 3 – DEP Assembly parameters of gas sensitive nanoparticles.**

Assembly parameters of gas sensitive nanoparticles..

This process is repeated sequentially for each electrode site and for each nanomaterial. The process flow for integrating three separate materials in a spatially selective manner on a single substrate is illustrated in Figure 23.

Multiple assemblies of the same type may be assembled simultaneously if the dispersion covers multiple electrodes. In this manner, sequential assembly of different materials with high repeatability and spatial resolution is easily accomplished. By other assembly means, the creation of heterogeneous, electrically-addressable sensor array would be a daunting, if not impossible, task.

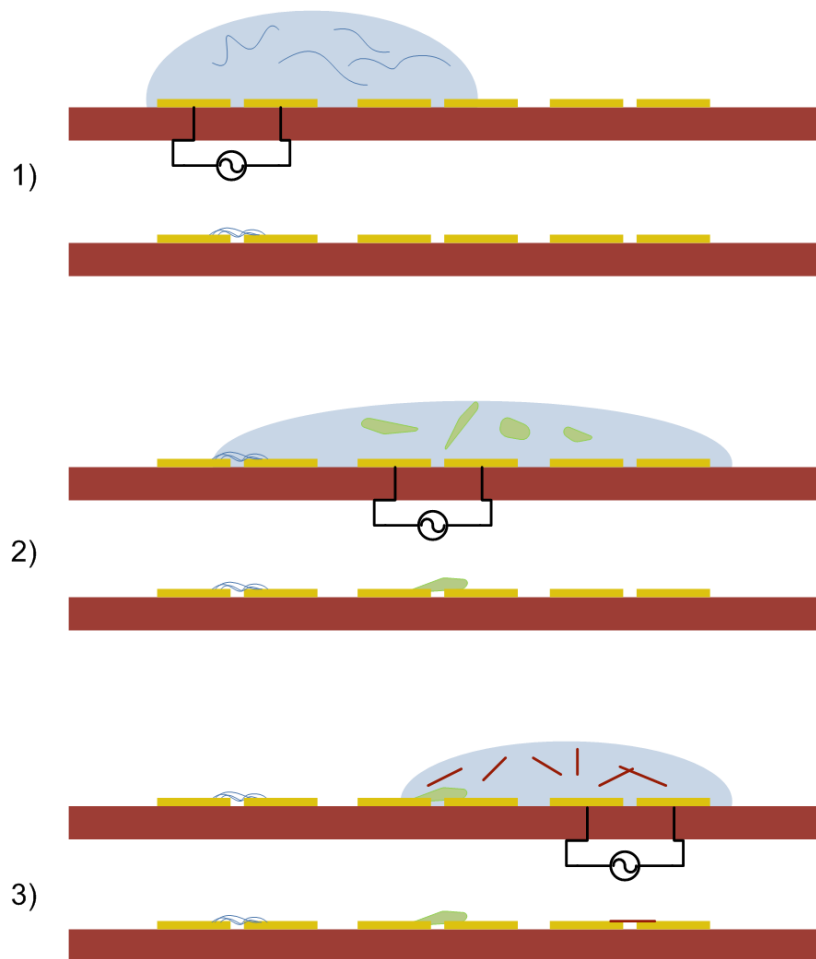


**Figure 23 – Process flow of multi-material sequential integration of different nanomaterials. (1) A drop of SWNT dispersion is placed on chip and a voltage is applied to the appropriate electrode(s). The dispersion is blown off leaving a n assembly of SWNT's (2) The same procedure is repeated for rGO at different electrode(s). (3) After repeating again for CuO, a heterogeneous array has been sequentially assembled with complete spatial selectivity.**

It should be noted that these assembly frequencies (which were determined heuristically) correspond to roughly similar relative DEP forces predicted by the

model put forth in next chapter. To further validate the model, an assembly grid was made to parametrically vary the assembly parameters to illustrate their effects on the assembly. The applied voltage was varied from 2.5 to 10 volts and the frequency from 50 to 500 kHz for the DEP assembly of rGO. The result is illustrated in Figure 24. As predicted by the model, the amount of assembly (reflected by the resistance) increases with applied voltage and decreases with frequency.

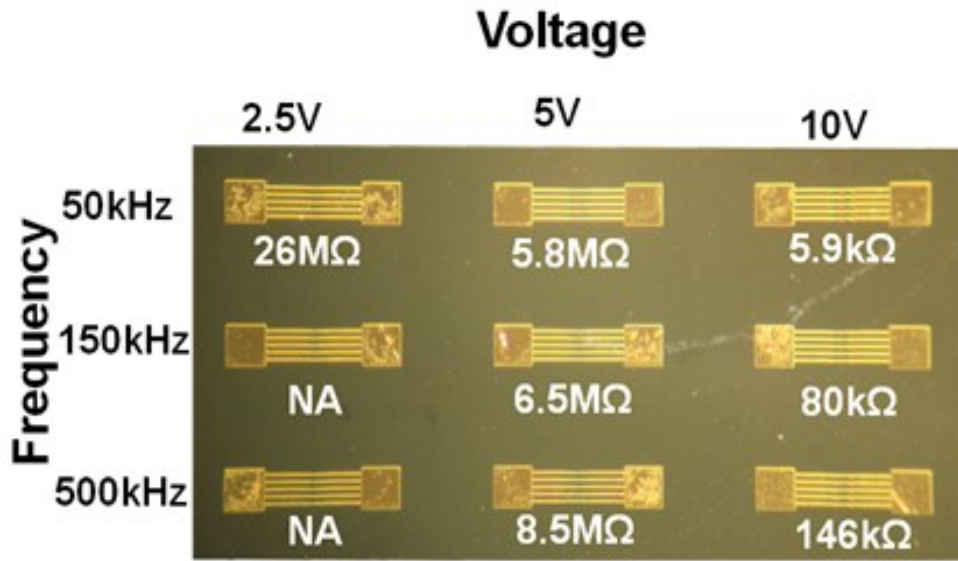
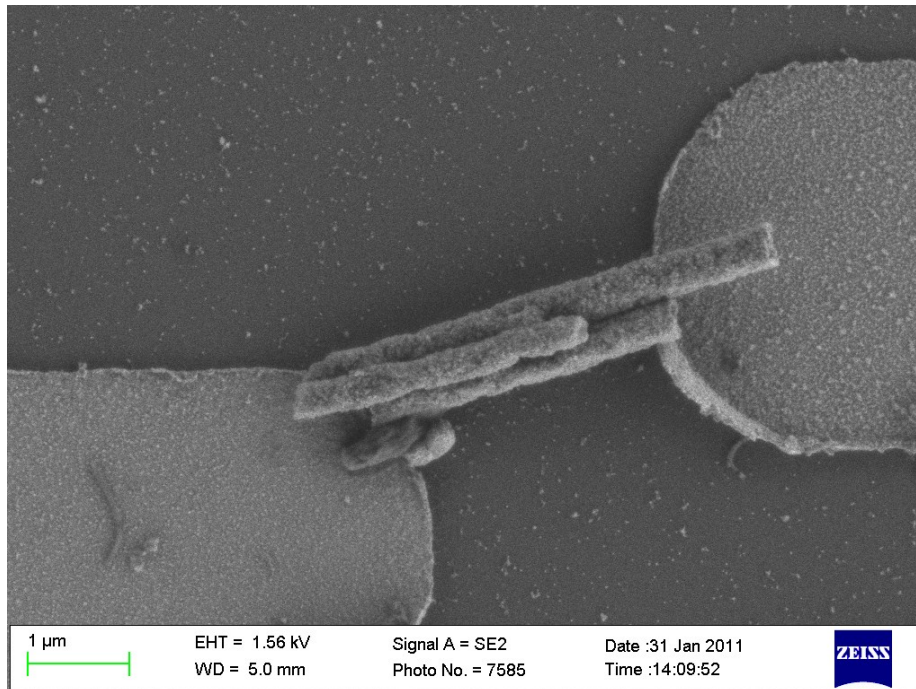


Figure 24 - Parametric variation of assembly parameters and resultant resistances. NA stands for no measurable assembly. Note that this is a microscope image; the nanoscale DEP assemblies between the above electrodes cannot actually be discerned at this level of magnification. Each electrode pair is separated by approximately a millimeter.

After the DEP assembly, the chip is soldered onto a daughter board, and the gas sensor array is ready for testing. A completed single gas sensor is shown in the following SEM image (Figure 25). Copper oxide nanowires are shown across two gold electrodes. Images of other assemblies will be shown with the results in Chapter 5.



**Figure 25 - Example of DEP assembly. CuO is assembled here.**

## Chapter 4: **Design and Modeling**

In this chapter, two parts of the DEP assembly are modeled. First, the resistive properties and second the mechanism of assembly with respect to the actual materials used. In order to understand the internal workings of gas sensor assembly, it is important to characterize the sources of resistance. This is especially important for a resistive sensor because sensitivity is inextricably linked to the series and parallel resistances around the sensor. Small parallel resistances and large series resistances will mask the gas response experienced by a chemiresistor. The effects of specific parameters of the DEP assembly process should be known in order to be able to intelligently modify assembly parameters to achieve higher or lower assembly resistances.

### 4.1 **Model of Dielectrophoretic Assembly**

The theory of DEP assembly was detailed in Chapter 2. The entire effects can be modeled by equations 2-1 to 2-5. The only data needed to create a frequency domain model of the nanomaterial materials is the permittivities and conductivities of the particles and mediums. This data is given in the following table:

Nanomaterial	Permittivity	Conductivity	Medium	Permittivity	Conductivity
Reduced Graphene Oxide	$3.5\epsilon_0$	100 S/m	DI Water	$78 \epsilon_0$	$5.5 \times 10^{-6}$ S/m
Carbon Nanotubes	$2.5\epsilon_0$	$10^5$ S/m	DMF	$37.5 \epsilon_0$	$1.6 \times 10^{-7}$ S/m
Copper Oxide	$15 \epsilon_0$	1 S/m			

**Table 4- Electrical properties of DEP particles and media [112-117].**

For this analysis the permittivities were assumed to constant over the frequency range of interest (0Hz to 1GHz). This assumption is sound in that, in general, the dipole oscillation interactions that cause changes in permittivity are observed at frequencies of 1GHz and higher. Other effects such as bond and

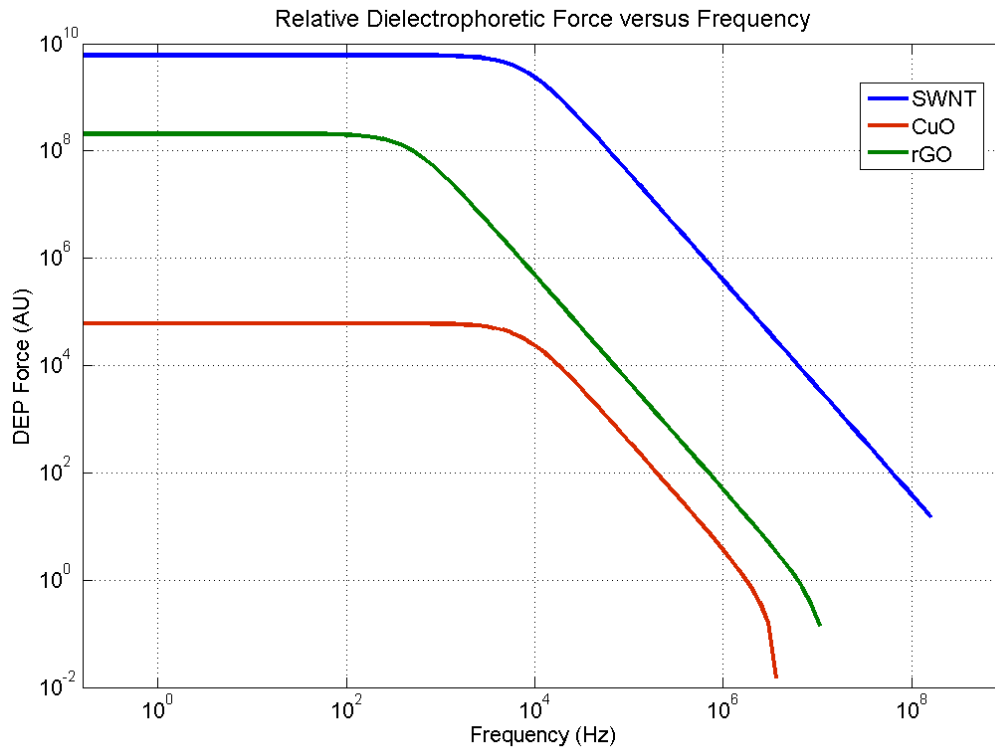


**Figure 26 - Relative DEP force observed for copper oxide in DI water, reduced graphene oxide in DMF, and single wall nanotubes in DI Water.**

atomic vibrations occur at even higher frequencies.

Using these values the above plot (Figure 26) of relative DEP forces versus frequency can be generated for each material / medium combination. This is a direct result of the Clausius-Mossotti factor. The applied voltage is not accounted for in the plot, but is assumed to be constant between every case. For all materials, the DEP force decreases with frequency. It should be noted that, while the DEP force is highest in the lower frequencies (<10kHz), other electrohydrodynamic mechanisms dominate in this regime, as discussed in Chapter 2.

Due to the log scale, the regimes of negative DEP are not plotted. The crossover points from pDEP to nDEP for copper oxide, rGO and SWNTs are modeled to be, respectively 10MHz, 30MHz, and 3THz. The nDEP force is several orders of magnitude smaller than that of pDEP. It is expected that capillary and Van der Waals interactions will dominate over DEP in the small radius that nDEP could function.

Two points should be noted concerning the degree of assembly by DEP: First the relative force shown in the figure above only relates the dielectrophoretic force as a mechanism to overcome other natural forces (such as Brownian motion) to guide nanomaterials to the electrodes. It does not strictly reflect the amount of assembly at the electrodes. However, it does a fairly decent job of indicating trends, as shown in Chapter 3. Second, other factors also have an equal, if not greater effect, on the amount of DEP assembly. The foremost of these factors is particle concentration. Obviously, if there is a greater density of dispersed material, more particles will be within the radius of the DEP force, and be

assembled. Other factors include temperature, time of assembly, and fluid viscosity[118].

#### 4.2 First Order Electrical Model of DEP Assembly

The cross section of a typical electrode for DEP assembly with assembled nanomaterial is shown in Figure 27. Illustrated in the diagram are the notable resistances of the simplified assembly. It should be noted that that the resistances are actually complex, but, in this work, all measurements were taken at DC. Therefore, only the real portion of resistance is considered. Major resistances include the parallel resistance through the substrate ( $Z_{\text{Parallel}}$ ), the contact resistances where the nanomaterial meets each electrode ( $Z_C$ ), and, of course, the resistance of the nanomaterial itself ( $Z_{\text{NM}}$ ). These resistances are not necessarily

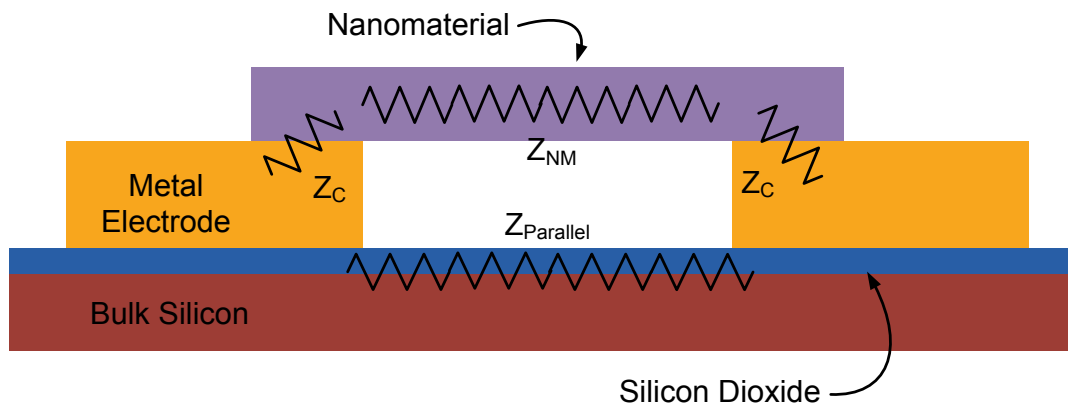


Figure 27 - Cross section of DEP assembly with notable resistances:

linear.

As discussed in the preceding chapter, the inter-electrode distance is between two and five microns in our implementations. Our choice of the electrode distance was based on the limits of our cleanroom fabrication process at Tufts

Micro and Nanofabrication facility. Smaller distances will allow for higher electric field and more spatial resolution in assembly.

#### 4.2.1 **Parallel Resistance**

The parallel resistance is orders of magnitudes greater than that of the DEP assembly. This shunt resistance is a result of the surface conductivity of the silicon oxide rather than the bulk resistance. Indeed, the equivalent bulk resistance observed 200nm of oxide across an area the size of the entire chip ( $1\text{cm}^2$ ) would be thousands of gigaohms [119]. The surface conductivity of thermal silicon oxide is, at worst, approximately  $1 \times 10^{-10}$  S [120]. This value actually varies with the ambient environment, affected by temperature and humidity, especially. The worst case value yields a value of approximately 1 gigaohm (parallel line electrode geometry), which matches well with the open circuit resistances observed prior to assembly. The open circuit resistance is generally greater than that of the DEP assemblies in any gas environment (though CuO assemblies can come close). Thus, this parameter can be largely ignored in the analysis of the electrical properties of the DEP assemblies.

#### 4.2.2 **Nanomaterial Resistance**

The nanomaterial resistance is a very complicated calculation and depends on several factors. Many factors play a role in determining the resistance between the contacts. While a complete (or even limited) discussion of the phenomena at work in determining this resistance is beyond the scope of this writing, brief mention should be made of the major factors governing the nanomaterial resistance.

a) **Bulk Resistivity**

In macroscale systems, the resistivity of an object can be calculated from the equations below:

$$R = \frac{\rho}{ta} \quad 4-1$$

$$R = \frac{\sigma}{a} \quad 4-2$$

where R is the resistance,  $\rho$  the bulk resistivity,  $t$  the thickness,  $\sigma$  the surface resistivity, and  $a$  is the aspect ratio of the width to the length of the electrode spacing. Many other factors can begin to dominate in nanoscale geometries, but these equations still have some bearing. From the preceding equations, we can expect that electrode geometries with high aspect ratios, such as that shown in Figure 14.a, will have smaller resistances. This is due to many more parallel paths being open for charge carriers to travel. Also, bulk resistivity on its own can be used to estimate the relative resistances of assemblies of different materials. The resistivities of the materials used in this work are given in Table 5.

Material	Resistivity	Reference
rGO	$10^2$ - $10^3 \Omega/\square$	[67, 121]
SWNT	$10^{-3} \Omega\text{-cm}$	[122]
Cu <sub>2</sub> O / CuO	$10^2$ - $10^4 \Omega\text{-cm} / 10^1$ - $10^2 \Omega\text{-cm}$	[123-125]

**Table 5 - Resistivities of selected nanomaterials. The units reflect the dimensionality of the material.**

b) **Percolation Theory**

Another source of resistance arises from networks of nanomaterial conductors. When a conduction path is defined by a network of individual and randomly

interconnected conductors, percolation theory is best-suited to describe the conductance of the system. This is most applicable to carbon nanotube networks.

A general formula for the resistance seen in conductive networks is given by

$$R = k(D - N_C)^\alpha L^\beta \quad 4-3$$

where  $k$  is a fitting constant,  $D$  is the density of the network,  $N_C$  is percolation threshold,  $\alpha$  is defined by the spatial arrangement of conductors,  $L$  is the average length of the conductors, and  $\beta$  is related to the inter-conductor resistance[126].

From this formula, one would expect an infinite resistance across a network until a critical density of conductors is reached. Thus, the amount of assembly also has a drastic effect in the determining the resistance. Greater amounts of conglomerated nanomaterial at the electrode allow for more parallel paths for current to travel, driving down the resistance. Alternatively, more layers of nanomaterial being added may be construed as increasing the thickness,  $t$ , in Equation 2-1, thereby lowering the resistance. One of the advantages of dielectrophoresis is that the amount may be controlled to some extent by varying the assembly parameters [127].

### c) *Scattering effects*

As the dimensions of materials approach the nanoscale, scattering effects begin to dominate the resistance of a material. For polycrystalline materials, these effects begin to manifest when the constraining dimension approaches the crystal grain size of the material. A simplified relation of resistivity increase due to scattering can be shown to be the following:

$$\rho = \rho_0 f(R, P) \frac{\lambda}{w} \quad 4-4$$

Where  $\rho_0$  is the bulk resistivity,  $f(R,P)$  is a function of,  $R$ , the reflectivity coefficient (probability of reflection at a grain boundary) and,  $P$ , the specularity,  $\lambda$  is the mean electron free path, and  $w$  is the smallest dimension of the nanomaterial [128]. Because the function of the coefficient of reflection and specularity is constant, the resistivity in nanoscale materials is proportional to the ratio of the mean free path and the width of material [129, 130].

Conversely, if the mean free path is greater than length of the material, electrons may travel without scattering. Thus, the material has negligible resistance as the electrons are constrained only by the laws of relativity. This requires the material to have extremely high electron mobilities. Carbon nanotubes and graphene can demonstrate this quality, but not at the length scales and quality of material presented in this work [131, 132].

#### d) ***Ambient Environment***

Lastly, the ambient environment has a large effect on the resistance. In the case of semiconductors, light and temperature create charge carrier pairs, thereby raising conductivity. Conversely, metals increase in resistance with temperature

And, of course, by design gases in the atmosphere are meant to affect the resistance of the materials in this study. Binding events on the surface of these materials offer or impede paths for current to travel, modulating the conductivity. Gas molecules can also participate in redox reactions at the surface injecting charge carriers which also modifies the assembly's resistance.

### 4.2.3 Contact Resistance

The resistance between the nanomaterial and the metal electrode is also a complex quantity depending on several factors. While an exhaustive discussion of contact resistance is beyond the scope of this work, the semiconducting nanomaterial and the metal electrode, in general, do not form an ohmic contact. Thus, a non-linear voltage current relationship is attained. This problem is accentuated by the non-intimate contact between the nanomaterial and electrode: the nanomaterial merely sits on top of the electrode. This is in contrast to other work, where intimate contact is achieved by depositing the metal electrode on top of the nanomaterial (frequently in four point measurements, which eliminate contact resistance effects) [133]. Furthermore, the connection can be further complicated by oxides or organic residues on the electrode. For this reason, gold electrodes are used to minimize the effects of resistive oxide layers.

#### a) *Constriction Resistance and Real Area of Contact*

One of the major influences in the contact resistance between two surfaces is the actual area of contact. This is not defined by the overlapping area of the nanomaterial and electrode, but rather by the amount of force between the two. The area of intimate contact between any two surfaces is only the amount of area needed to bear the pressure exerted between them. In macroscale systems the pressure is exerted mainly by gravity, but in microscale systems Van der Waals forces, capillary forces, and electrostatic forces play the greatest roles[134]. Figure 28 shows the relative strength of these forces.

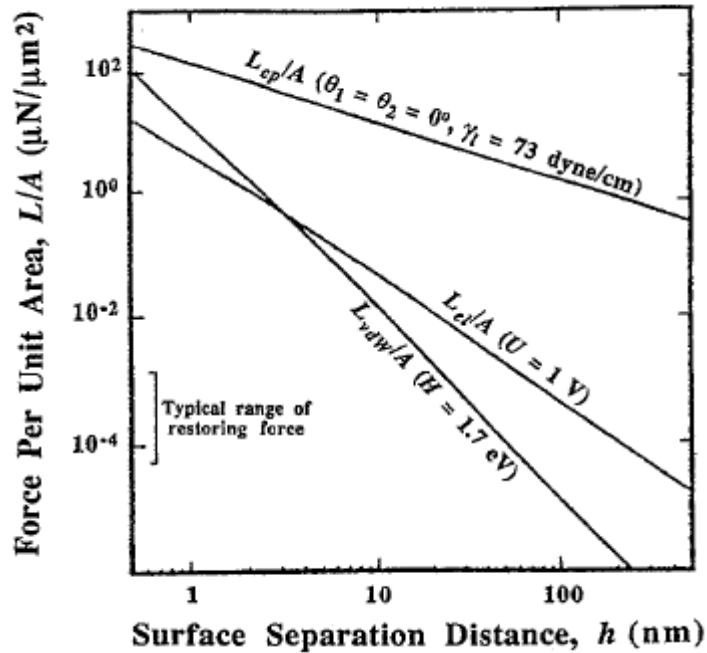


Figure 28- Force per unit area of Van der Waals forces, electrostatic forces and capillary forces as a function of separation distance[134].

A variety of models exist for the real contact area as a function of material hardness, elastic modulus, and applied pressure [135, 136]. Each of these indicates that the ratio between the apparent area of contact and actual area of contact can be many orders of magnitude.

A generalized expression for contact resistance is given by the following equation:

$$R = \frac{\kappa}{A_a} (\rho_1 + \rho_2) \left(\frac{E}{F}\right)^\beta \quad 4-5$$

where  $A_a$  is the apparent area of contact;  $\kappa$  is a proportionality constant,  $\rho_1$  and  $\rho_2$  are the resistances of the two materials;  $E$  is a reduced measure of the hardness or elastic modulus of the two materials;  $F$  relates the pressure or the force between the two surfaces (such as Van Der Waals attraction, capillary forces, or

electrostatic forces), and  $\beta$  is an exponent that roughly ranges from  $\frac{1}{3}$  to 1 [137, 138]. The analysis is further complicated by the scale of the assembly: for rigid materials there should only a handful of discrete contacting points between the nanomaterial and electrode. Furthermore, scattering effects can happen at the interface, leading to an increase in resistance [136, 139]. Fortunately, carbon nanotubes and reduced graphene oxide are exceptionally flexible, and SEM images suggest intimate contact across the entire overlap area.

b) ***Metal-semiconductor Junctions (Schottky Diodes)***<sup>3</sup>

Of greater concern is the Schottky diode that forms when a semiconductor (such as rGO or copper oxide) meets a metal. The diode action is a result of the quantum barrier that forms at the junction due to differences in the work functions of each material. A first order approximation of the barrier height can be estimated with the following equations:

$$\varphi_{bn} = \varphi_m - \chi_s \quad 4-6$$

$$\varphi_{bp} = E_g - [\varphi_m - \chi_s] \quad 4-7$$

where  $\varphi_b$  is the barrier height for the n- or p-type semiconductor;  $\varphi_m$  is the work function of the metal;  $\chi_s$  is the electron affinity of the semiconductor, and  $E_g$  is the bandgap of the semiconductor. Using the values from the literature (summarized in Table 6), an approximate value for the expected barrier heights for the rGO, CuO and SWNTs on gold are, respectively, .5eV, .57eV and .1eV.

---

<sup>3</sup> It should be noted that, as mentioned in Chapter 2, roughly two thirds of carbon nanotubes are metallic in nature. Thus, constriction resistance is the only form of contact resistance, and the ensuing sections on metal-semiconductor junctions do not apply.

The electron affinity and expected barriers for SWNTs is also given for completeness' sake, but, recalling that the metallic majority of SWNTs most likely dominate the resistance of these assemblies, it is likely an ineffectual point. MWNTs are always metallic, and as such their properties are omitted.

Property	Value
Gold Work Function	5.1eV
Electron Affinity of rGO	4.6eV
Electron Affinity of CuO	4.07eV
Band gap of CuO	1.6eV
Electron Affinity of SWNT	4.8-5.05eV

**Table 6- Relevant material properties to Schottky barriers [140-142]**

While this gives a first order approximation of the barrier height, the resistance seen across the contact can be derived to be the following non-linear. The current-voltage characteristic of an ideal diode junction is defined by

$$I(V) = I_0 \left[ e^{\frac{qV}{nkT}} - 1 \right] \quad 4-8$$

$$I_0 = cT^2 A e^{\frac{-q\phi_b}{kT}} \quad 4-9$$

$$R(V) = \frac{nkT}{I_0 q e^{\frac{qV}{nkT}}} \quad 4-10$$

where  $q$  is the elementary unit of charge,  $k$  is the Boltzmann constant,  $n$  is a correction factor valued between 1 and 2, which accounts for the abruptness of the junction, and  $T$  is temperature. In Equation 4-9,  $c$  is the Richardson constant, which deals with the number of interface states;  $A$  is the area (real contact area) of the junction, and  $\phi_b$  is the barrier height. Equation 4-10 is simply Equation 4-8 re-expressed as to represent the resistance as a function of voltage rather than the of current[143, 144].

This resistance model is fine for forward biased junctions; however, in DEP assemblies, one side of the assembly will always be reversed biased. The main method of breakdown in Schottky barriers junctions is tunneling. The tunneling probability is a classic quantum electronics problem, and the solution is given below (tailored to the Schottky barrier case):

$$T = e^{\left(\frac{4L\sqrt{2qm^*\varphi_B}}{3\hbar}\right)} \quad 4-11$$

$$I_T = Tqv_d nA \quad 4-12$$

where  $L$  is the barrier width (the width of the depletion region),  $m^*$  is the effective electron mass,  $\varphi_B$  is the barrier height, and  $\hbar$  is the reduced Planck constant. The tunneling current,  $I_T$ , (and therefore resistance via ohms law) can be found by Equation 4-12, in which  $n$  is the carrier concentration,  $v_d$  is the drift velocity, and  $A$  is the area. In the case of a uniform electric field, equation 4-12 will yield that the tunnel resistance is inversely proportional to the tunneling probability,  $T$ . In this case, like the forward bias case, the tunnel resistance decreases exponentially as a function of barrier height[145].

There is one more step necessary to transform the current-voltage relationship into a usable model for the DEP assembly. The geometry of the assembly must be considered. As shown in Figure 29, the current does not travel uniformly into the nanomaterial assembly, but rather the current crowds near the end of the contact. To account for this, the transmission line method may be used. In this method, the interface is viewed as a resistive network of “pi” connections (as shown). Integrating an infinitely dense “pi” network of resistors yields the following expression for the total resistance

$$R_c = \frac{\sqrt{\rho_c R_S}}{W} \coth \left( L \sqrt{\frac{R_S}{\rho_c}} \right) \quad 4-13$$

where  $W$  is the width of the contact;  $R_S$  is the sheet resistance of the semiconductor;  $L$  is the inter-electrode distance;  $\rho_c$  is the contact resistance. The

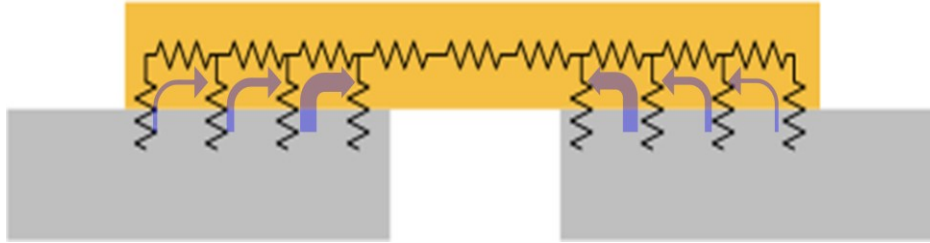


Figure 29- Current pathways in metal-semiconductor assembly junction

contact resistance is equal to the resistance divided by the real area of contact. The contact resistance can be derived from the tunnel resistance or the diode resistance, or both. The main point to take away from this equation is that, as one would expect, geometries with a short inter-electrode distance (small  $L$ ) and wide shared width (high  $W$ ) will have the smallest contact resistance.

### c) *Ambient Effects*

Again, the ambient environment can have an effect on metal-semiconductor IV relationship. The above equations are littered with temperature dependencies. Furthermore, absorbed gases can change the electron affinity or work function of a material, thereby affecting the barrier height.

### 4.2.4 Capacitances

While the capacitance across the electrodes was not measured (all measurements were taken at DC), the reactive portions of the impedance do merit brief mention. The main capacitance observed would be the capacitance across

the Schottky diode. This capacitance per unit area is given by the following equation:

$$C_j = \sqrt{\frac{q\epsilon_s N_D}{2(\varphi_b - V_a)}} \cong \frac{\epsilon_s}{d} \quad 4-14$$

where  $q$  is the elementary unit of charge,  $\epsilon_s$  is the permittivity of the semiconductor,  $N_D$  is the dopant concentration,  $\varphi_b$  is the barrier height, and  $V_a$  is the applied voltage.

This expression is derived from the equation for a parallel plate capacitor and inserting the depletion region width as the spacing between the plates. The quality factor of this capacitor is expected to be quite low: the defect density of the tested materials is quite high.

These effects and their mitigation are demonstrated in the following chapter, which details the measured results of the assembled chemiresistors.

# Chapter 5: **Results**

In this chapter, the gas sensing responses of the sequentially assembled nanomaterials are reported. After a brief overview of the test setups, the response of each sensor on its own will be analyzed and discussed. The response of the ensemble of nanomaterials integrated sequentially on chip is then

## 5.1 **Test Setups**

In order to extract chemoresistance data from the array, a back end electronics test set up is necessary to address and measure each assembly. This was accomplished through a printed circuit board and a daughter board. The daughter board only consists of the packaged gas sensor array. This allows for easy switching between gas sensing chips without the need for soldering and desoldering. A more detailed schematic and board layout can be found in the appendix. The following paragraphs describes the operation, which entails a LabView interface to simultaneously control an IC switch array as well as a benchtop Keithley SourceMeter to measure resistances. Each output of the switch array is connected to a different assembly, thus allowing the sequential measurement of each individual sensor.

Two test setups were used for the characterization of the fabricated electronic noses: one at Tufts University and one at University of Massachusetts Lowell.

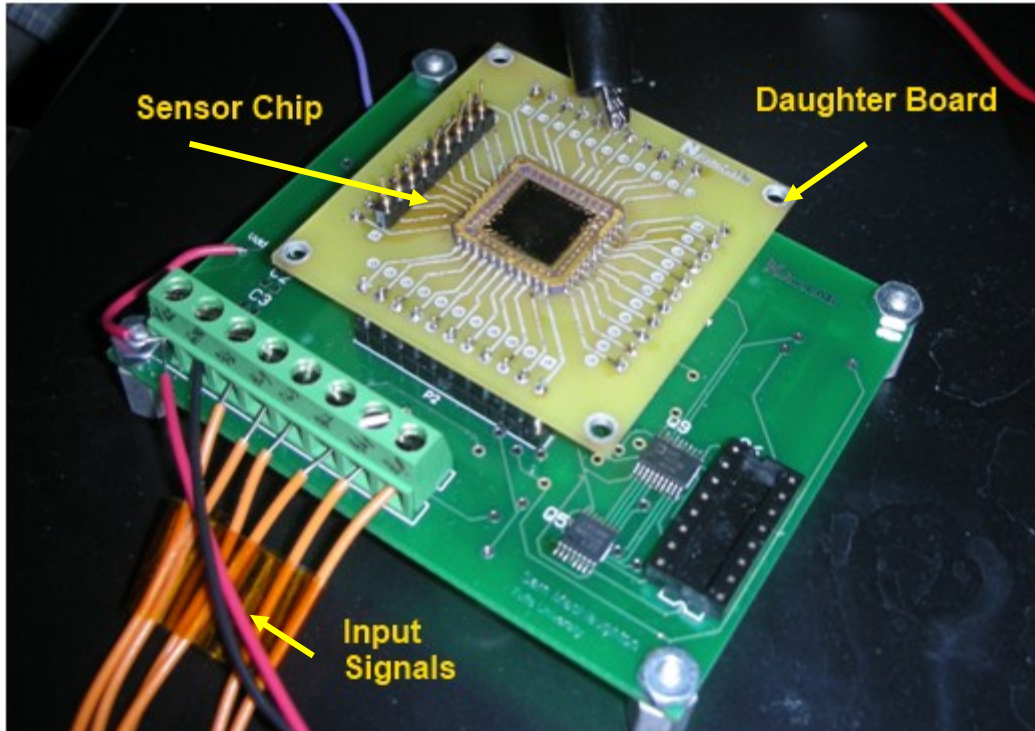


**Figure 30 - Picture of multiplexed gas sensor test board. The entire set up (excluding laptop) can easily be held in one hand.**

Each has the capability to perform time multiplexed resistance measurements of an entire array of sensors. The period to sweep an entire 40 element array of sensors is on the order of hundreds of milliseconds, which is far less than the time constants associated with the both the resistance response of the chemiresistors and also the diffusion rates of gaseous species. As such, time multiplexed

resistance measurements do not result in the loss of information from gas interactions<sup>4</sup>.

The operation proceeds as follows: the LabView interface cycles through the switch array, addressing each sensor. This allows a Keithley 6430 SourceMeter to measure the resistance of the addressed sensor. This allows for the time-multiplexed measurement and acquisition of every sensor over a period of hundreds of milliseconds. The switch array does contribute approximately 200 $\Omega$  of series resistance in addition to the chemoresistance. However, the resistances of the assemblies are, at a minimum, tens of kilohms. Thus, the added series resistance is negligible.

---

<sup>4</sup> This is not strictly accurate. The time constants of gas interaction kinetics (binding/unbinding and absorption/desorption) require a higher bandwidth to resolve. This information manifests itself in the noise spectrum of the signal. This spectrum, spanning a range from hertz to kilohertz can yield much insight into the gas molecules involved, but this analysis is beyond the scope of this work.

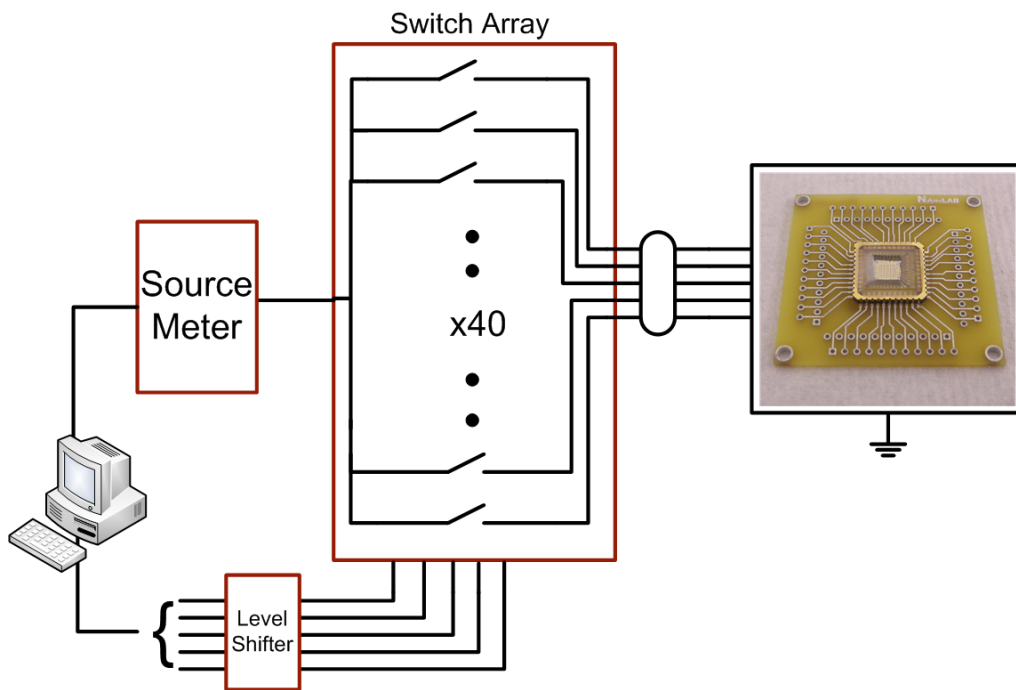


**Figure 31 - Simplified diagram of evaluation board operation.**

The saturated (or very nearly saturated gas environment) was created by thoroughly soaking a cotton swab with the liquid phase of the desired analyte and placing the swab above the sensor chip. The sensor chip and swab are enclosed under a small beaker to limit diffusion of the gas vapor away from the chip. As the gas species tested are extremely volatile, the enclosed chamber quickly reaches the vapor pressure of the analyte.

The UML test set up is similar excepting an Environics (Tolland, CT) gas dilution system with the ability to dilute gases with nitrogen to sub-PPM quantities is used to guarantee specific vapor concentrations. This allows very precise control of the gas environment within a custom-built chamber.

An IV curve for an typical rGO assembly is shown in Figure 32. Note the non-linear effects observed at low voltages. The 'turn-on' voltage is slightly lower than the predicted value of 0.5eV. The deviation could be attributed to the

fact that the work function of graphite was used as an approximation for that of rGO. In both test set ups, the chemiresistors were biased such that the voltage would be above this threshold. This ensured that the non-linear effects of the metal-semiconductor effects would be limited. While there Schottky contacts may also respond to gases, previous measurements on these materials were executed with four terminal measurements, eliminating contact effects[41]. As such, contact effects were also suppressed in this work by taking measurements at voltages far exceeding the Schottky threshold. Investigations into the Schottky response to gas analytes are ongoing.

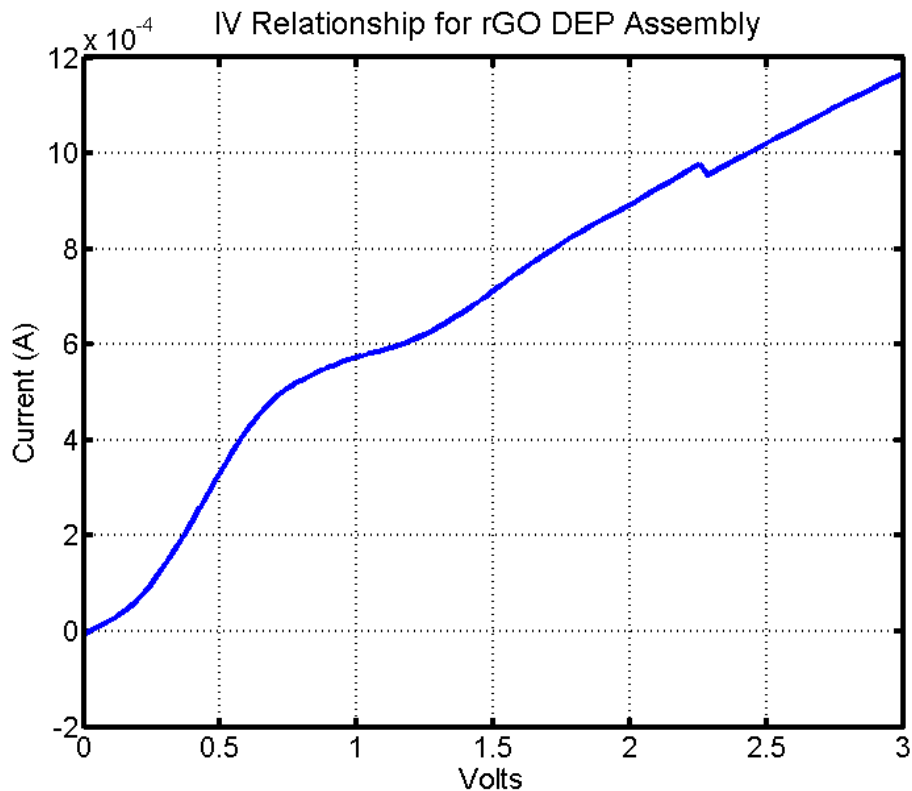


Figure 32 - IV curve of rGO DEP assembly showing non-linearity at low voltages. Higher potentials were used in testing to avoid responses in this regime. The kink observed at 2.1V is the result of range switching on the SourceMeter.

## 5.2 Measured Responses of Individual Gas Sensors

The following gases vapors, shown in Table 7, were tested at concentrations very near their vapor pressures, their maximum equilibrium partial pressure in an air atmosphere. Data for water is also provided for perspective. Toluene was included to test the sensors' response to aromatic, non-polar solvents and introduce some variety as most other tested analytes against the aliphatic compounds. Likewise, ammonia was tested as it is expected to give a strong response due to its dipole moment (allows for better binding), its alkalinity (bases are electron donors, charge carrier injectors), and its high vapor pressure (higher concentration in air).

	Chemical Formula	Dipole Moment (Debyes)	Molecular Weight (g/mol)	Vapor Pressure (kPa)
<b>Methanol</b>	CH <sub>3</sub> OH	1.7	32.0419	16.95
<b>Ethanol</b>	CH <sub>3</sub> CH <sub>2</sub> OH	1.69	46.0684	5.945
<b>Acetone</b>	CH <sub>3</sub> COCH <sub>3</sub>	2.88	58.0791	24.527
<b>Isopropyl Alcohol</b>	(CH <sub>3</sub> ) <sub>2</sub> CHOH	1.56	60.095	4.399
<b>Toluene</b>	C <sub>6</sub> H <sub>5</sub> CH <sub>3</sub>	0.37	92.1384	2.933
<b>Ammonia (20% aq.)</b>	NH <sub>3</sub>	1.472	17.0305	28.74
<b>Water</b>	H <sub>2</sub> O	1.87	18.0153	3.142

Table 7- Chemical and physical properties of test gases [146, 147].

### 5.2.1 Reduced Graphene Oxide

Out of all sensors tested, graphene samples gave the most consistent and time-invariant response. A typical rGO assembly can be seen in the SEM image shown in Figure 33. In the image, the graphene sheets make a tent-like structure

between the electrodes. It is apparent that several overlapping layers are assembled between the electrodes, not just one graphene flake.

A typical gas response is given shown in Figure 34. The gases tested in this run were, in order of introduction to the chamber, methanol (twice), ethanol, isopropyl alcohol (IPA), and acetone. The resistance changes are quite substantial, with fractional resistance changes exceeding 100%. This also shows the reproducibility of the measurements, as the initial two responses to methanol are nearly identical. Unlike the other nanomaterials tested, rGO demonstrated the most constant baseline resistance: the baseline remained constant throughout testing, and the assemblies were quick to recover to the baseline after a gas species was removed from the environment. The other point to note is that fractional resistance change corresponds roughly to vapor pressure. That is,

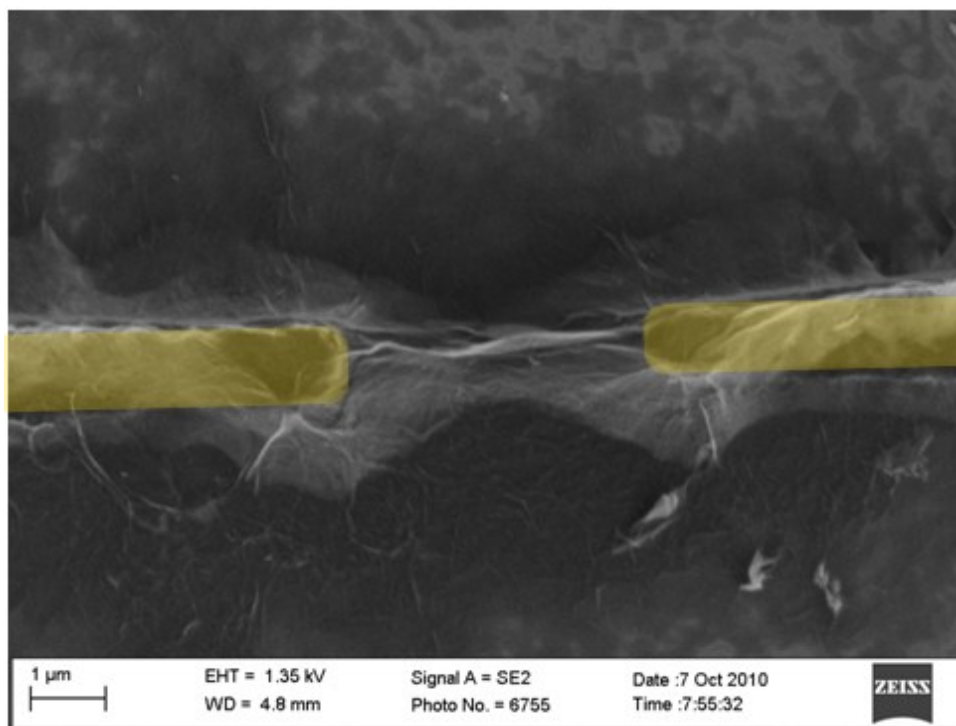


**Figure 33 – False color SEM images of assembled rGO. Gold electrodes are demarcated by the gold coloring.**

higher vapor pressure species, such as acetone, have greater responses compared to lower vapor pressure gases such as ethanol or IPA. This is ostensibly because a higher density of gas molecules were in the in the environment.

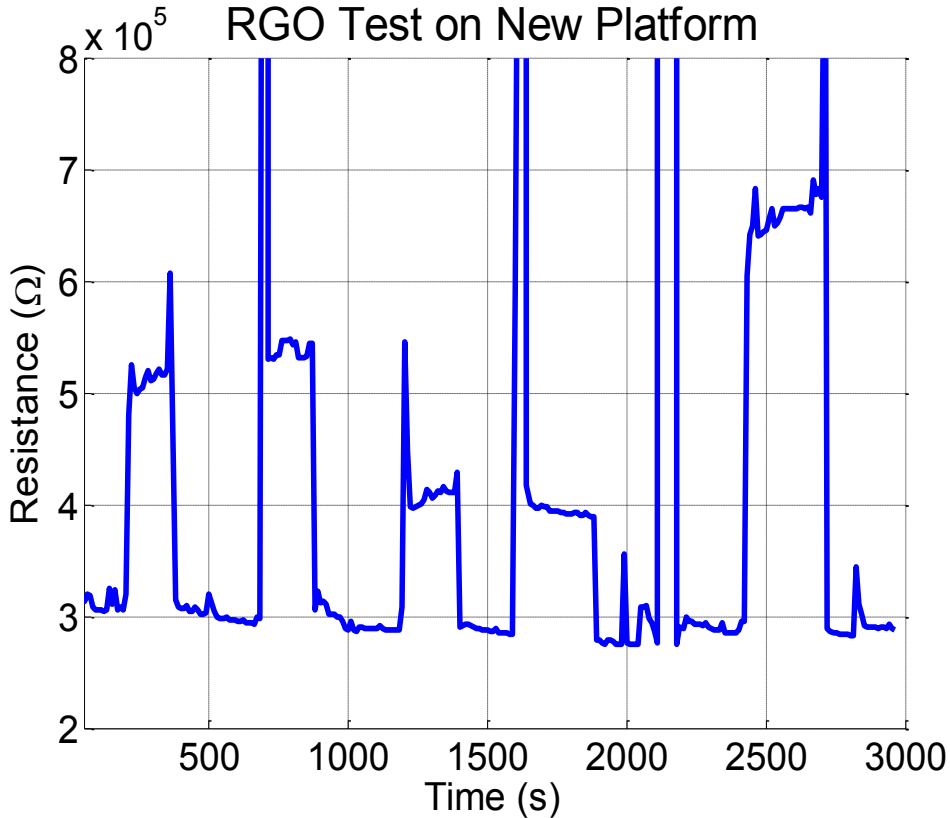
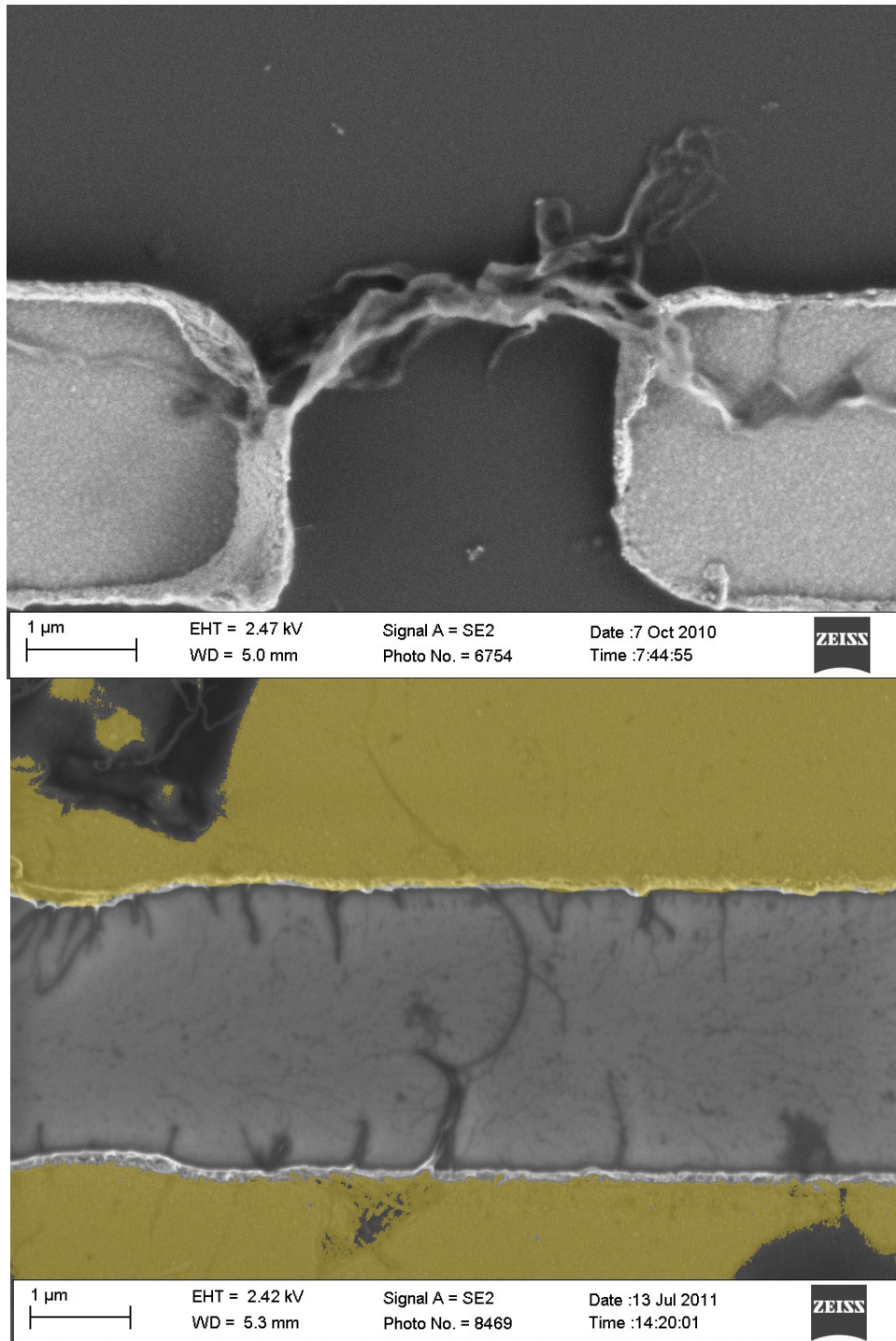


Figure 34 – Typical response of single rGO gas sensor. The spikes at the end of each gas hump are due to mechanical vibrations caused by the introduction of the gas and are not artifacts of the sensing mechanism itself. The peaks correspond to (in order) Methanol, Methanol again, Ethanol, IPA, and the last one being acetone. The sharp spike observed after 2000 was caused by a loss of connection.

### 5.2.2 Carbon Nanotubes

An SEM image of a single wall nanotube assembly is shown in **Error! eference source not found.** The nanowires tended to bundle to some extent form ‘ropes’ between electrodes rather than individual strands. If desired, this could potentially be alleviated by more aggressive sonification prior to assembly or assembling out of a more dilute solution. However, because the nanotubes align with the applied field, both the bundles and individual CNT’s align across



**Figure 35 - SEM image of single wall carbon nanotube DEP assembly. Electrodes in false color gold.**

the electrodes. Thus, the random network of conductors that defines percolation theory is not readily applicable to these assemblies. Typically assembly

resistances ranged from 10 kilohms to hundreds of kilohms depending on assembly conditions (frequency and applied field).

A typical gas response for two simultaneously tested CNT sensors is shown in Figure 36. The baseline resistances of each sensor differ by almost an order of magnitude and are not constant throughout the measurement. The drift in baseline resistance is hypothesized to be a result of environmental factors such as humidity or temperature (perhaps due to the resistive heating of the assembly over the course of the measurement). However, evidence to support this hypothesis is forthcoming.

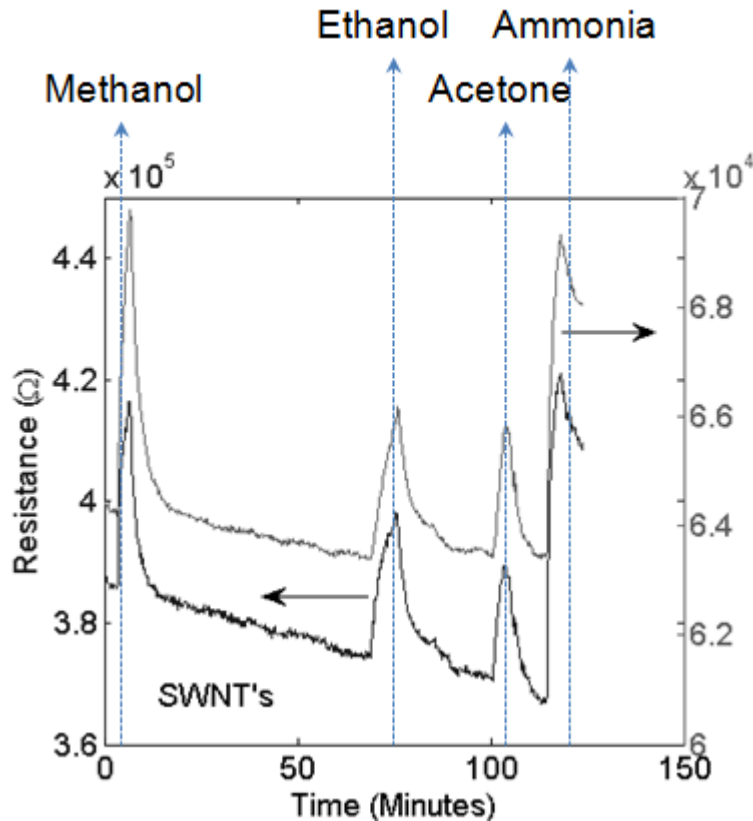


Figure 36 - Response of two separate SWNT DEP assemblies to simultaneous gas testing. Note the separate y-axis for each assembly. Despite being almost an order of magnitude different in resistance, the fractional changes in resistance are almost identical.

It should be noted that the gas responses observed in carbon nanotube assemblies resemble those of the rGO sensors. That is, similar fractional resistance changes are observed for each gas analyte. This is probably a result of the chemical similarities of graphene and CNT's. These carbon allotropes are chemical cousins; and, thus, it should be expected that their responses be similar. This is a disadvantage in a cross-reactive array, as much of the information rGO and CNT sensors relay is redundant to one another.

There was no significant difference in response observed between the SWNT's supplied from Helix and those from Unidym. The Helix CNT's generally showed a slower response, but this could be attributed to greater 'bundling' in their assemblies. In turn, this bundling could be traced to a more concentrated dispersion, or simply that the CNTs were more prone to clumping. Regardless, the responses were of the same magnitude. This is not too surprising, as both materials were made by CVD methods and both advertised to be of the same purity. 2 $\mu$ m

### 5.2.3 **Copper Oxide**

An SEM image of a copper oxide DEP assembly is given in Figure 37. Careful inspection will reveal that the nanowires are greater than the 200nm diameter of the pores in which they were formed. This is because the oxidation of copper following release from the AAO template and dispersion increases the

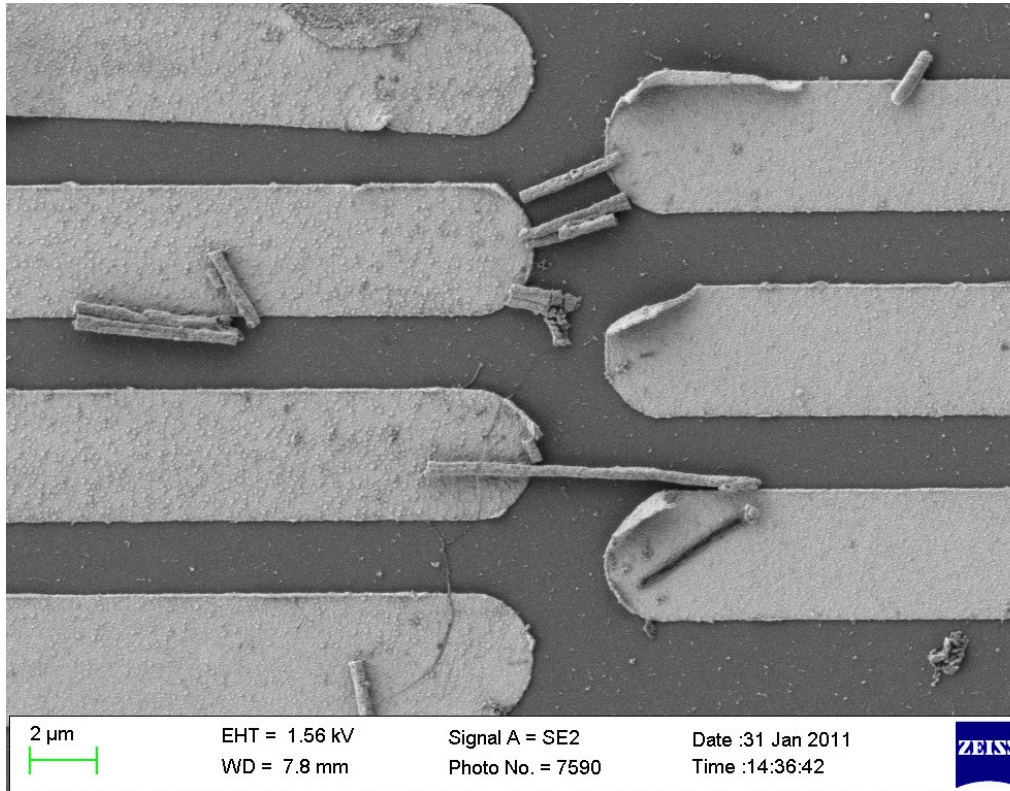


**Figure 37- Bundled and single copper oxide nanowires assembled across DEP electrode. The nanowires exceed the 200nm pore diameter because the nanowires thicken during oxidation.**

diameter of the nanowire; much like the oxidation of silicon will thicken a wafer.

A gas response for a copper oxide gas sensor is given in Figure 38. The response is not as clean as those with rGO or carbon nanotubes. Copper oxide showed resistance responses on the order of 50%, similar to that observed in the carbon sensors. The response times were on the order of minutes upon this introduction of the gas species, and the time to recover to the baseline resistance

could be hours or more. This suggests excellent binding between the copper oxide and gas analytes. The response also shows a good deal more noise as well as the response times being slower. These are not necessarily bad traits: the noise spectrum may be a source of information of the gas information, and the time constants associated with the response and recovery of the sensor are very much related to the gas environment. For example, acetone, an extremely polar molecule, would be expected to bind more easily, and, thus, have a longer desorption time.

As with CNT's and rGO, copper oxide assemblies the observed fraction changes in resistance exceeding 50% were observed. This shows that copper oxide has potential as a nanoscale gas sensor. However, there does remain much work in its optimization. The noisiness and slow responses must be either put to use for gas sensing, or removed. One potential way to remediate the slowness in response is to decrease the diameter of the nanowires, allowing gas to fully penetrate more quickly through the entire assembly. With 200nm diameter nanowires, recovery to baseline conditions can take hours, even up to a day.

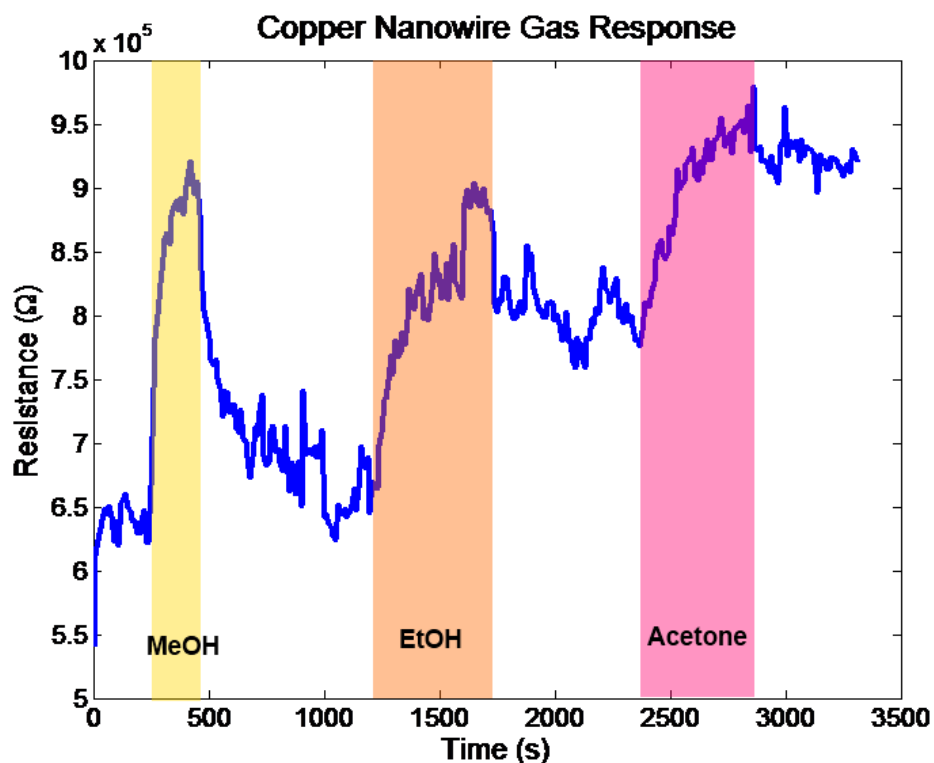
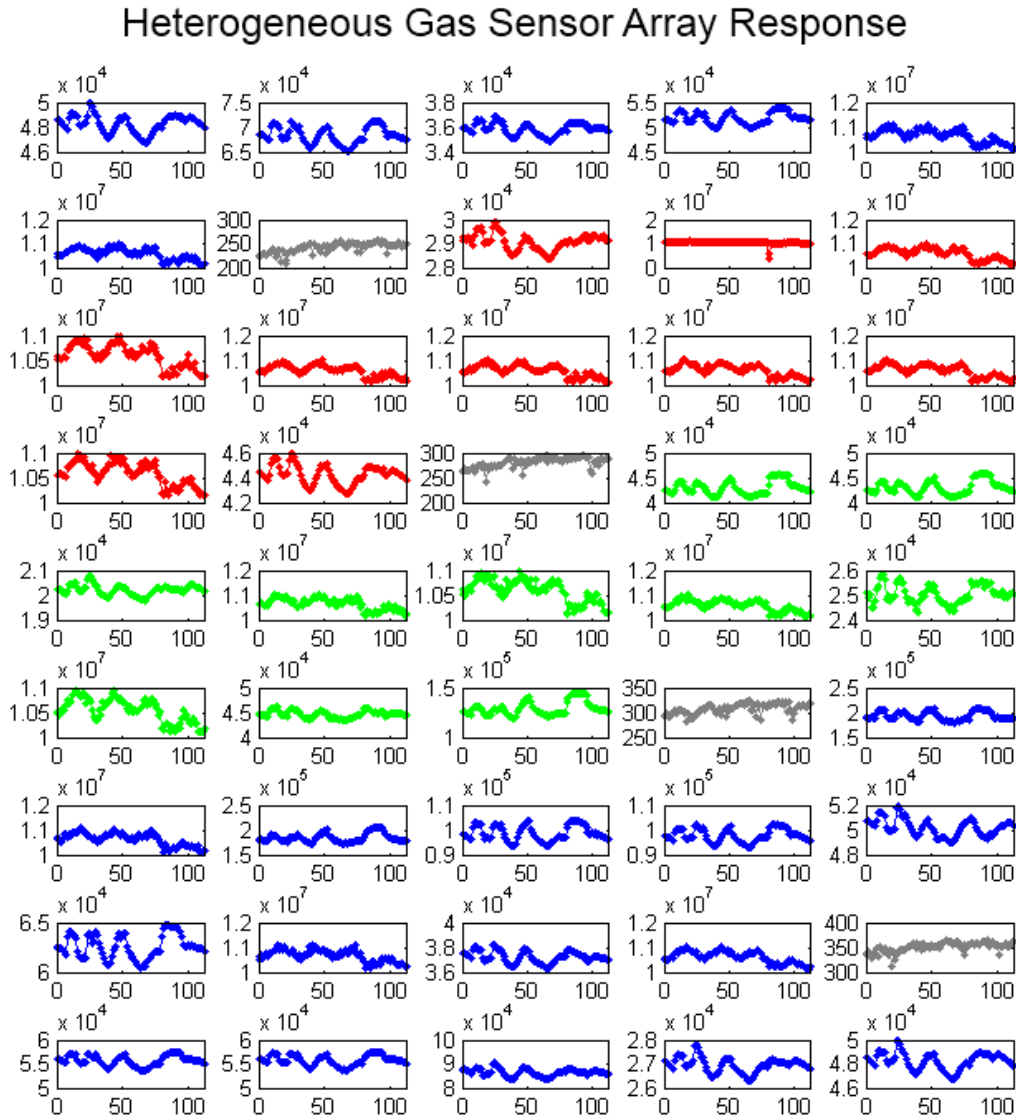


Figure 38 - Gas response of copper oxide to methanol, ethanol and acetone.

One incongruity with the copper oxide nanowire assemblies is their surprisingly low resistance. From the bulk resistivity of copper oxide (given in Table 5), one would expect much higher resistances than those observed in CNT or rGO samples. One possible explanation would be that surface conduction may be the main mode of electron travel in CuO nanowires, much like the observed parallel resistance across the silicon oxide. Another possible explanation is impurities such as the organic addition agents that are used in the copper plating solution. These embedded impurities could increase the conductivity of the material. However, deviations from the expected resistance in the copper oxide samples could also be a result of non-stoichiometric ratios of copper and oxygen in the material.

### 5.3 Electronic Nose Performance

While each material functions on its own as functional gas sensor, the electronic nose functionality is gained by the three materials sequentially integrated onto the same substrate and read out in parallel. The results of such a



**Figure 39- Parallel output of heterogeneous gas sensor array. Green is rGO; red is CuO; Blue is SWNT's; Grey is ground pins. X-axis is time in minutes; Y-axis is resistance. The four visible responses correspond, in order, to Methanol, Acetone, IPA, and Ethanol**

test are shown in Figure 39. The yield on this chip was exceptionally high; only

one sensor out of forty failed to respond to gases. Typically sensor yield varied between 50% and 75%. However, as this test indicates, nearly 100% yields are possible, and further process optimization could realize higher yield. The other point to note from this data is garnered from the four ground leads on the chip. The added series resistance is at most  $300\Omega$ . This combines the trace resistance on chip and the switch resistance of the muxes. This is indeed negligible compared to the resistances of the DEP assemblies.

In this first shown test, the sensor was exposed to methanol, acetone, isopropyl alcohol and ethanol. These are all chemically similar aliphatic, low molecular weight, volatile organic solvents. Thus, the response is very similar for each gas. In order to demonstrate the power of a cross reactive array, three chemically disparate analytes were introduced to a gas sensor array. The resulting resistance data is shown in Figure 40. The data has been normalized such that the baseline resistance is equal to one.

In this test, methanol was introduced into the chamber three separate times, followed by three toluene injections, and finally two ammonia tests. As in the previous graphic, CuO is represented in red; rGO in green; and CNT's in blue. The methanol and, especially, ammonia responses dwarfs most toluene responses. However, the responses actually exceed 5% in terms of fractional resistance change for the majority of assemblies. This is a very measurable amount, just not viewable next to the 250% fractional resistance changes observed in some of the ammonia responses. A few of CuO assemblies responded with a 25% or greater

decrease in resistance to toluene, a signature response to toluene. This decrease is a specific indicator of toluene.

This test demonstrates the advantages of having a cross-reactive array for chemical sensing. The three different materials varying responses to different gas species make it possible to identify the added analyte, even without the aid of a pattern recognition engine. Methanol can be distinguished as it gives a

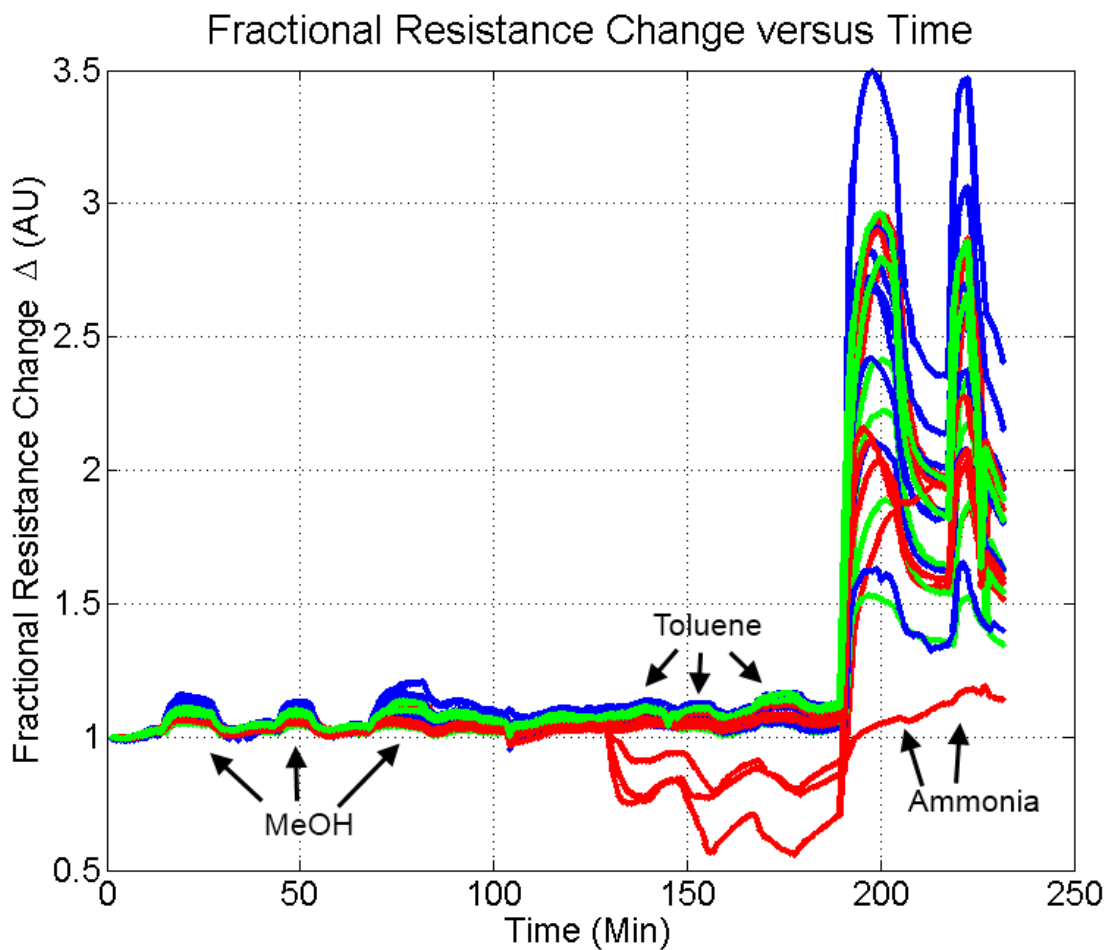


Figure 40 - Gas response to methanol, toluene and ammonia.

characteristic increase in resistance for all materials, with the greatest response coming from carbon nanotubes, then from rGO, and finally CuO. The toluene responses can be distinguished by two traits: First, the response is the slowest.

This might be caused by the fact that toluene is non-polar and relatively nonreactive; thus, not prone to binding. Second, CuO, in some cases, shows a profound decrease in resistance. We have no definite explanation as to why some CuO samples show an acute decrease in resistance while others show a slight increase. Finally, ammonia can be identified simply due to magnitude of both the fractional change in resistance and the time constants associated with its response. Ammonia shows a very fast uptake response, and comparatively slow return to baseline resistance.

While this shows that three dissimilar gases can be distinguished through the presented gas sensor array, three similar gases (such as methanol, ethanol and isopropyl alcohol) would be more difficult. However, an appropriately designed machine learning algorithm such as those discussed in Chapter 2 could distinguish data on levels not readily perceivable. To further limitations are the inability to perceive concentration and distinguish mixtures of gases. Studies on concentration dependence are the focus of future work. We believe that these issues could be solved with advanced pattern recognition and a wider range of chemiresistive sensor elements.

# Chapter 6: **Conclusions**

A procedure for the heterogeneous and sequential integration of different nanoscale chemiresistive elements is presented and shown to be a functional electronic nose. The fabrication and operation of these chemiresistive elements is Dielectrophoresis is modeled and shown to be a versatile and powerful technique for the bottom-up assembly of nanomaterials. Gas sensing responses for the individual sensors are shown. A heterogeneous, sequentially assembled sensor array of 40 elements is shown to be proficient not only at the gas detection, but also of gas identification. The electronic nose presented is easily transferable to CMOS dies.

## 6.1 **Future Work**

While the presented electronic nose has demonstrated functionality, there are still many paths to research to further its olfaction ability.

### 6.1.1 **Further Sensor Characterization**

With additional testing apparatuses, more interesting and realistic gas environments may be tested against the electronic nose. These tests would include varying concentrations of the gases already tested, testing with new gases, and testing mixtures of gases.

### 6.1.2 **Sensor Mechanism**

Investigations into the sensor mechanism are ongoing. The sensors are being studied by scanning probe microscopy. This technique allows for in situ

monitoring of the charge density, impurity concentrations, and potential distribution with sub-micron resolution across the assemblies. These studies will answer questions of whether sensing happens at the contacts and the mode of chemoresistance (i.e. is the mechanism a redox reaction, a binding event, doping-related, or a modification of the material electron affinity / work function?). With this knowledge, optimization of the gas sensors both in fabrication, assembly, and measurement will be possible.

### **6.1.3 Greater Sensor Variety**

Currently, there are only two types of sensors implemented (metal oxide and carbon). Granted the two carbon sensors (rGO and CNT) are very different, this still does allow for much improvement. Currently, conducting polymers are primarily being investigated as a third type of sensor. The diversity of sensor elements is a direct measure of the ease of achieving selectivity.

### **6.1.4 Classification Algorithm Implementation**

In order to take full advantage of the sensor array, a pattern recognition engine should be implemented to process the data from the sensors. A classification algorithm, if advanced enough, can not only distinguish from similar gases, but also provide information on the concentration of analytes and mixtures of analytes. However, the ability of the pattern recognition engine is limited by the cross-reactivity and diversity of the sensor array.

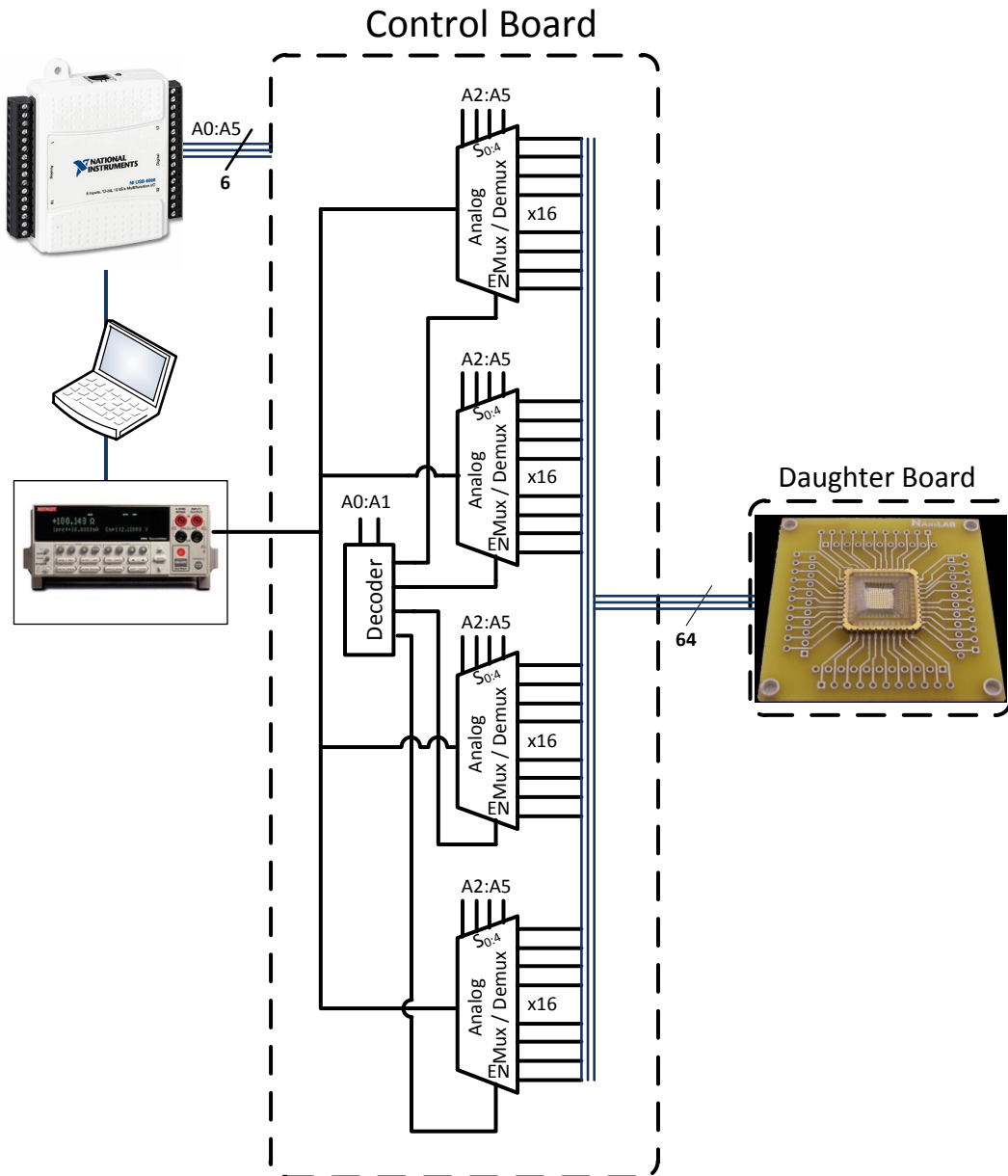
### **6.1.5 CMOS**

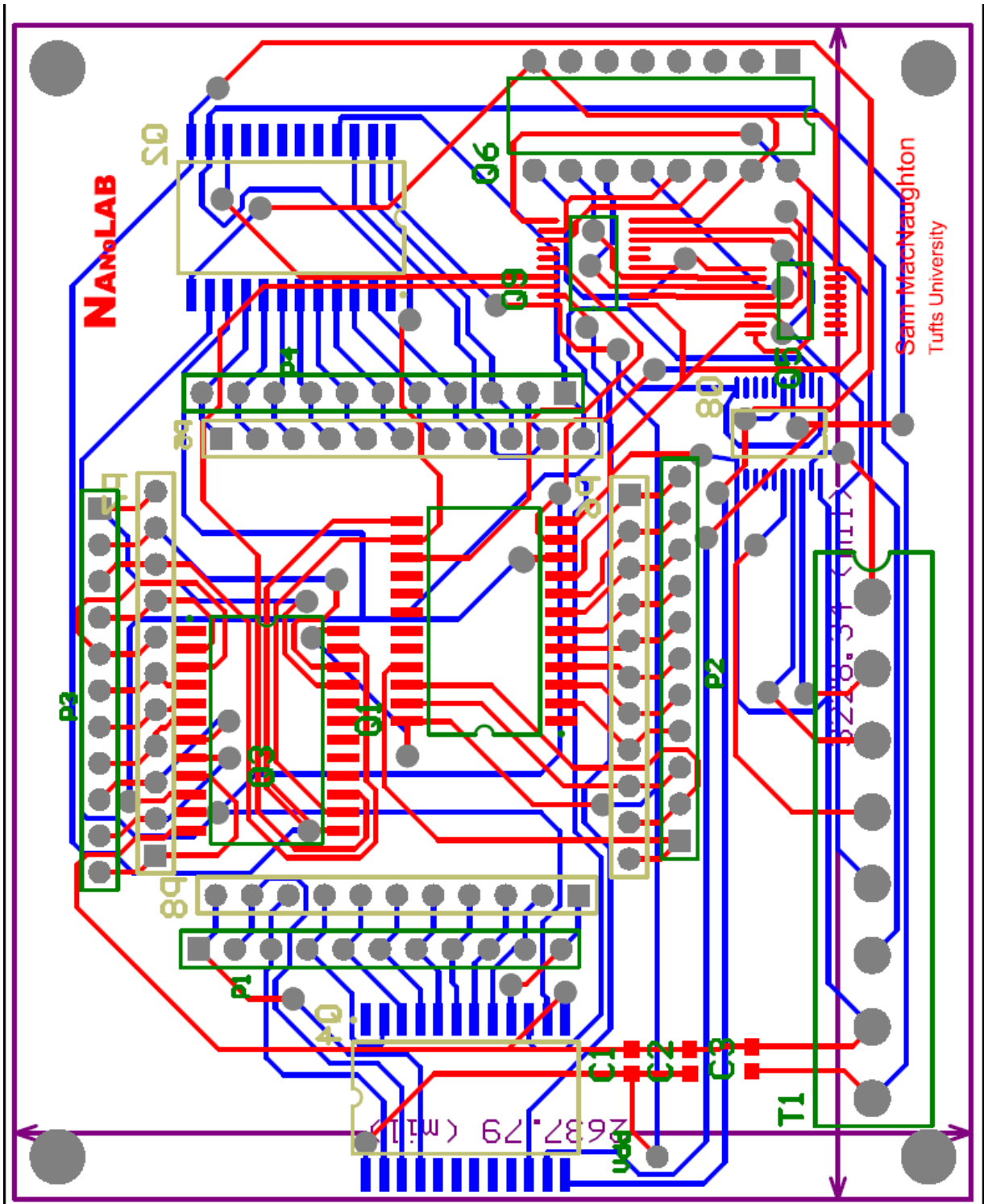
The final step of creating a truly versatile and practical electronic nose would be the integration of the presented technology on CMOS. This system would

include the heterogeneous sensor array, the sensor electronics, and, perhaps, even some of the pattern recognition processing. Such a system would be part of a new generation of sensors with applications stretching from food service to environmental monitoring and safety.

# Appendix I. Printed Circuit Board Design

This section shows the production documents of the PCB design which including six MUX/DEMUX switch units and level shifters to manage different voltage supplies.





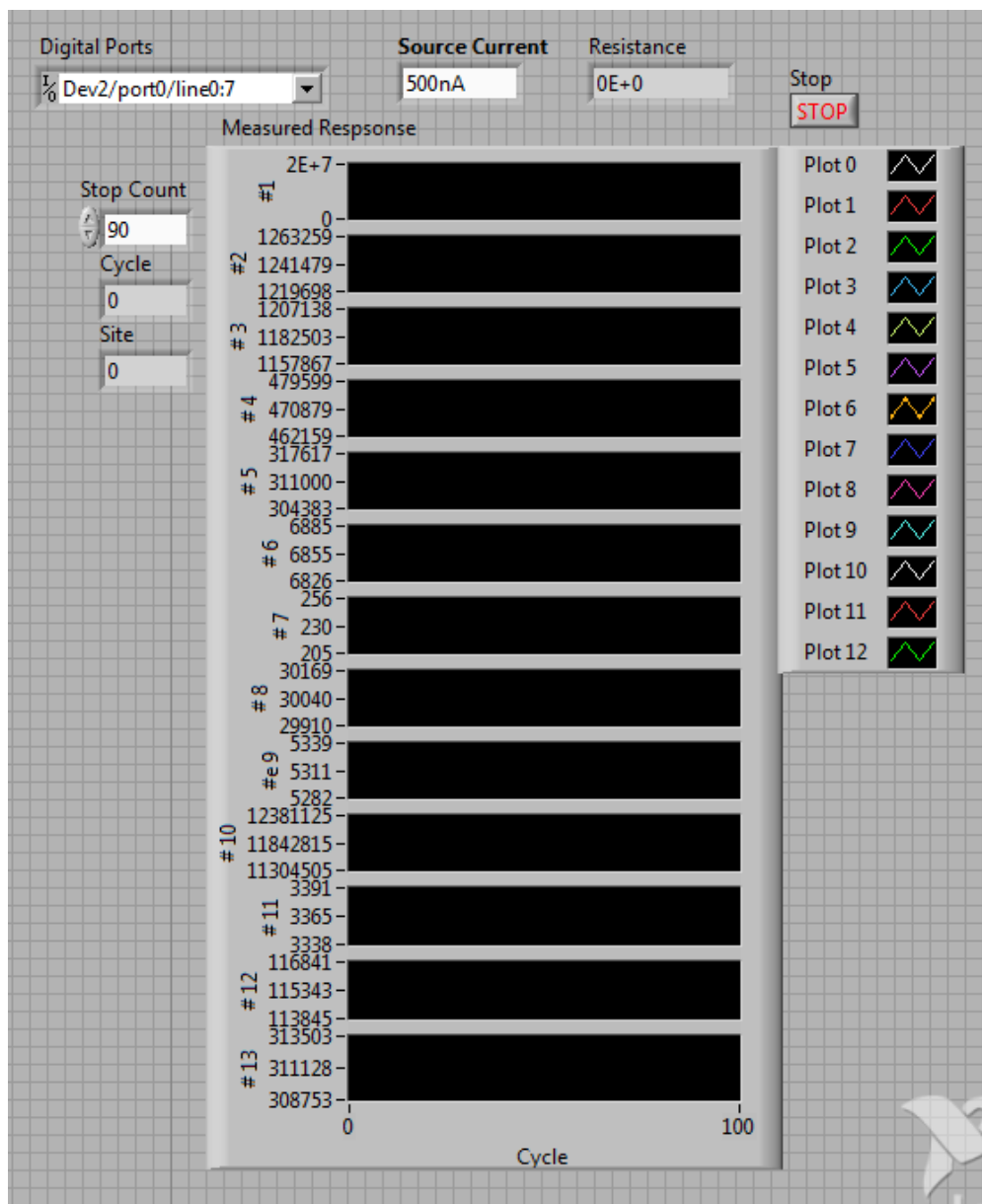
**Notes about board setup:**

There are “missing codes” or floating nodes on the output of the mux/demux switches. These are accounted for on the software side in the LabView environment.

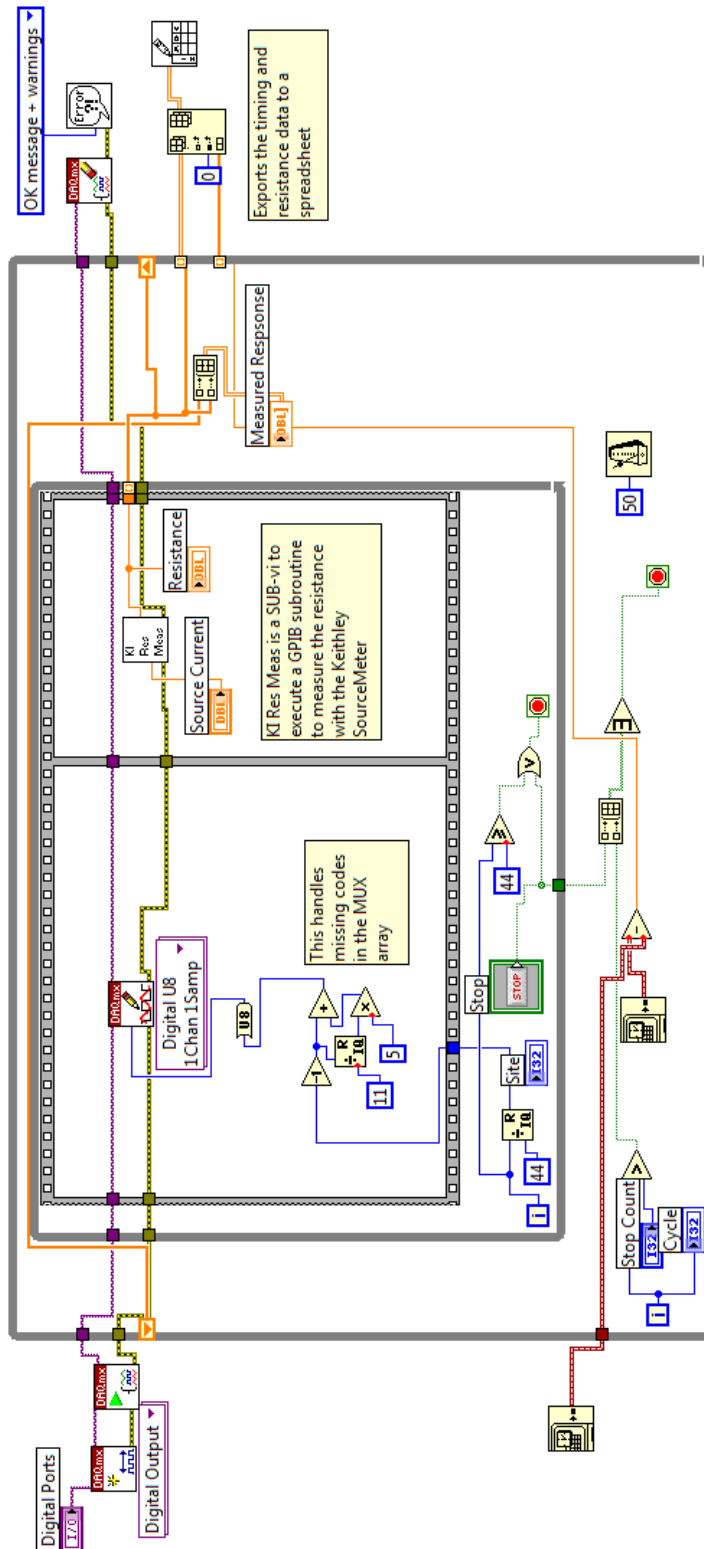
The board allows for power supplies ranging from 5-15V via the use of level shifting chips. The switch resistance is decreased by an order of magnitude by utilizing a 15V supply. However, the switch resistance of  $200\Omega$  is already orders of magnitude smaller than the total resistance of any assembly. Therefore, for convenience, the 5V supply from the DAQ interface is used. This eliminates the need for a power supply.

## Appendix II. LabView Interface

The LabView interface shown below controls the board and acquires (and live plots) the data from the board. Due to screen real estate limitations, only twelve individual traces may be plotted on their own axes. The top axis shows all forty traces on the same plot.



The inner workings (block diagram) of the LabView interface is shown below.



## Relevant MatLab Code

Shown below is the MatLab code to plot the relative DEP strength for different nanomaterials in different mediums.

```
function xx = DEP_PLOT(Em, Ep, Sigm, Sigp)
%Usage: DEP_PLOT(Em, Ep, Sigm, Sigp)
% where Em is the permittivity of the medium
% Ep is the permittivity of the particle
% Sigm is the conductivity of the medium
% Sigp is the conductivity of the particle

freq = logspace(0,9,100)./(2*pi());

Ems = -(j*Sigm./freq)+Em;
Eps = -(j*Sigp./freq)+Ep;

xx = real((Eps - Ems)./(3*Ems)); %Rod or wire
%xx = real((Eps - Ems)./(3*Eps)); %Disc, platelet

semilogx(freq, xx, 'LineWidth',3);

xlabel('Frequency (Hz)', 'FontSize',16)
ylabel('DEP Force (AU)', 'FontSize',16)
xlim([0 1e9])
title('Relative Dielectrophoretic Force versus Frequency', 'FontSize',18)
h = gca;

set(h, 'FontSize',16)
grid on

% text(10^6,1.5,{'\epsilon_m = ' Em, '\epsilon_p = ' Ep,
'\sigma_m = ' Sigm, '\sigma_p = ' Sigp})
end
```

Below is the code to plot the data as exported from the LabView interface given in the previous appendix.

```
function plotmuxdata2(data)
yy = size(data,1)-1;

h = gca;
set(h, 'FontSize',16)
ColorSet = varycolor(46); %This makes it easier to distinguish
plots
set(h, 'ColorOrder', ColorSet);

data(1:yy,2:size(data,2)) =
data(1:yy,2:size(data,2))./(ones(yy,1)*data(1,2:size(data,2)));
plot(data(2:yy,1)/60,data(2:yy,2:47),'.-')

xlabel('Time (Min)', 'FontSize',16)
ylabel('Fractional Resistance Change \DeltaR/R
(AU)', 'FontSize',16)
title('Fractional Resistance Change versus Time', 'FontSize',18)

legend(cellstr(num2str((1:46)')), 'FontSize',10)

end
```

# References

- [1] S. I. Association, "International Technology Roadmap for Semiconductors: Executive Summary ": Semiconductor Industry Association, 2009.
- [2] C. Hierold, "Intelligent CMOS sensors," in *Micro Electro Mechanical Systems, 2000. MEMS 2000. The Thirteenth Annual International Conference on*, 2000, pp. 1-6.
- [3] A. El Gamal and H. Eltoukhy, "CMOS image sensors," *Circuits and Devices Magazine, IEEE*, vol. 21, pp. 6-20, 2005.
- [4] D. X. D. Yang, A. E. Gamal, B. Fowler, and H. Tian, "A 640×512 CMOS image sensor with ultrawide dynamic range floating-point pixel-level ADC," *Solid-State Circuits, IEEE Journal of*, vol. 34, pp. 1821-1834, 1999.
- [5] "Omnidirectional Microphone with Bottom Port and Digital Output," Analog Devices, Norwood, MA 2010.
- [6] H. Qu, D. Fang, and H. Xie, "A Monolithic CMOS-MEMS 3-Axis Accelerometer With a Low-Noise, Low-Power Dual-Chopper Amplifier," *Sensors Journal, IEEE*, vol. 8, pp. 1511-1518, 2008.
- [7] H. Hatt, "Molecular and cellular basis of human olfaction," *Chemistry & Biodiversity*, vol. 1, pp. 1857-1869, 2004.
- [8] K. Mori, H. Nagao, and Y. Yoshihara, "The olfactory bulb: Coding and processing of odor molecule information," *Science*, vol. 286, pp. 711-715, Oct 22 1999.
- [9] M. Leon and B. A. Johnson, "Olfactory coding in the mammalian olfactory bulb," *Brain Research Reviews*, vol. 42, pp. 23-32, 2003.
- [10] K. J. Albert, N. S. Lewis, C. L. Schauer, G. A. Sotzing, S. E. Stitzel, T. P. Vaid, and D. R. Walt, "Cross-Reactive Chemical Sensor Arrays," *Chemical Reviews*, vol. 100, pp. 2595-2626, 2000.
- [11] K. Arshak, E. Moore, G. M. Lyons, J. Harris, and S. Clifford, "A review of gas sensors employed in electronic nose applications," *Sensor Review*, vol. 24, pp. 181-198, 2004.
- [12] M. P. Hughes, "AC electrokinetics: applications for nanotechnology," *Nanotechnology*, vol. 11, p. 124, 2000.

- [13] M. J. Madou, *Fundamentals of microfabrication: the science of miniaturization*, 2nd ed. Boca Raton: CRC Press, 2002.
- [14] J. Voldman, "A microfabricated dielectrophoretic trapping array for cell-based biological assays," Massachusetts Institute of Technology, 2001.
- [15] C.-L. Chen, "SS-DNA Decorated Single-Walled Carbon Nanotube Based Sensors Integrated Onto CMOS Circuitry," in *Electrical Engineering*. vol. Doctor of Philosophy Boston: Northeastern University, 2009.
- [16] H. A. Pohl, *Dielectrophoresis : the behavior of neutral matter in nonuniform electric fields*. Cambridge ; New York: Cambridge University Press, 1978.
- [17] A. Zehe, A. Ramirez, and O. Starostenko, "Mathematical modeling of electro-rotation spectra of small particles in liquid solutions. Application to human erythrocyte aggregates," *Brazilian Journal of Medical and Biological Research*, vol. 37, pp. 173-183, 2004.
- [18] B. R. Burg, V. Bianco, J. Schneider, and D. Poulidakos, "Electrokinetic framework of dielectrophoretic deposition devices," *Journal of Applied Physics*, vol. 107, pp. 124308-124308-11, 2010.
- [19] B. Kirby, *Micro- and nanoscale fluid mechanics : transport in microfluidic devices*. New York: Cambridge University Press, 2010.
- [20] O. D. Velev and E. W. Kaler, "In Situ Assembly of Colloidal Particles into Miniaturized Biosensors," *Langmuir*, vol. 15, pp. 3693-3698, 1999.
- [21] I. Doh and Y. H. Cho, "A continuous cell separation chip using hydrodynamic dielectrophoresis (DEP) process," *Sensors and Actuators A: Physical*, vol. 121, pp. 59-65, 2005.
- [22] B. G. Kim, K. S. Yun, and E. Yoon, "Active positioning control of single cell/microbead in a micro-well array chip by dielectrophoresis," 2005, pp. 702-705.
- [23] C. F. Chou, J. O. Tegenfeldt, O. Bakajin, S. S. Chan, E. C. Cox, N. Darnton, T. Duke, and R. H. Austin, "Electrodeless dielectrophoresis of single-and double-stranded DNA," *Biophysical Journal*, vol. 83, pp. 2170-2179, 2002.
- [24] Y. Dan, Y. Cao, T. E. Mallouk, A. T. Johnson, and S. Evoy, "Dielectrophoretically assembled polymer nanowires for gas sensing," *Sensors and Actuators B: Chemical*, vol. 125, pp. 55-59, 2007.
- [25] S. I. Jung, J. S. Choi, H. C. Shim, S. Kim, S. H. Jo, and C. J. Lee, "Fabrication of probe-typed carbon nanotube point emitters," *Applied Physics Letters*, vol. 89, p. 233108, 2006.

- [26] T. Hunt and R. Westervelt, "Dielectrophoresis tweezers for single cell manipulation," *Biomedical microdevices*, vol. 8, pp. 227-230, 2006.
- [27] A. D. Wissner-Gross, "Dielectrophoretic reconfiguration of nanowire interconnects," *Nanotechnology*, vol. 17, p. 4986, 2006.
- [28] J. Li, Q. Zhang, D. Yang, and J. Tian, "Fabrication of carbon nanotube field effect transistors by AC dielectrophoresis method," *Carbon*, vol. 42, pp. 2263-2267, 2004.
- [29] R. Pethig and G. H. Markx, "Applications of dielectrophoresis in biotechnology," *Trends in Biotechnology*, vol. 15, pp. 426-432, 1997.
- [30] T. P. Hunt, D. Issadore, and R. M. Westervelt, "Integrated circuit/microfluidic chip to programmably trap and move cells and droplets with dielectrophoresis," *Lab on a Chip*, vol. 8, pp. 81-87, 2008.
- [31] S. Evoy, N. DiLello, V. Deshpande, A. Narayanan, H. Liu, M. Riegelman, B. R. Martin, B. Hailer, J. C. Bradley, W. Weiss, T. S. Mayer, Y. Gogotsi, H. H. Bau, T. E. Mallouk, and S. Raman, "Dielectrophoretic assembly and integration of nanowire devices with functional CMOS operating circuitry," *Microelectronic Engineering*, vol. 75, pp. 31-42, 2004.
- [32] A. Narayanan, Y. Dan, V. Deshpande, L. Nicole Di, S. Evoy, and S. Raman, "Dielectrophoretic integration of nanodevices with CMOS VLSI circuitry," *Nanotechnology, IEEE Transactions on*, vol. 5, pp. 101-109, 2006.
- [33] C. L. Chen, V. Agarwal, S. Sonkusale, and M. R. Dokmeci, "The heterogeneous integration of single-walled carbon nanotubes onto complementary metal oxide semiconductor circuitry for sensing applications," *Nanotechnology*, vol. 20, p. 225302, 2009.
- [34] A. Enteshari, G. A. Jullien, O. Yadid-Pecht, and K. V. I. S. Kaler, "All CMOS low power platform for dielectrophoresis bio-analysis," in *Solid-State Circuits Conference, 2005. ESSCIRC 2005. Proceedings of the 31st European*, 2005, pp. 339-342.
- [35] S. Oh, Y. Cheng, J. Zhang, H. Shimoda, and O. Zhou, "Room-temperature fabrication of high-resolution carbon nanotube field-emission cathodes by self-assembly," *Applied Physics Letters*, vol. 82, p. 2521, 2003.
- [36] X. Xiong, C. L. Chen, P. Ryan, A. A. Busnaina, Y. J. Jung, and M. R. Dokmeci, "Directed assembly of high density single-walled carbon nanotube patterns on flexible polymer substrates," *Nanotechnology*, vol. 20, p. 295302, 2009.

- [37] V. Dua, S. P. Surwade, S. Ammu, X. Zhang, S. Jain, and S. K. Manohar, "Chemical Vapor Detection Using Parent Polythiophene Nanofibers," *Macromolecules*, vol. 42, pp. 5414-5415, 2009.
- [38] X. Chen, S. Lenhert, M. Hirtz, N. Lu, H. Fuchs, and L. Chi, "Langmuir-Blodgett Patterning: A Bottom-Up Way To Build Mesostuctures over Large Areas," *Accounts of Chemical Research*, vol. 40, pp. 393-401, 2007.
- [39] X. Li, G. Zhang, X. Bai, X. Sun, X. Wang, E. Wang, and H. Dai, "Highly conducting graphene sheets and Langmuir-Blodgett films," *Nature Nanotechnology*, vol. 3, pp. 538-542, 2008.
- [40] N. Minami, Z. Weihong, S. Kazaoi, R. Azumi, and M. Matsumoto, "Langmuir-Blodgett films of single-wall carbon nanotubes: layer-by-layer deposition and in-plane orientation of tubes," *Jpn. J. Appl. Phys.*, vol. 42, pp. 7629-7634, 2003.
- [41] V. Dua, S. P. Surwade, S. Ammu, S. R. Agnihotra, S. Jain, K. E. Roberts, S. Park, R. S. Ruoff, and S. K. Manohar, "All-Organic Vapor Sensor Using Inkjet-Printed Reduced Graphene Oxide," *Angewandte Chemie*, vol. 122, pp. 2200-2203.
- [42] J. Jang, J. Ha, and J. Cho, "Fabrication of Water Dispersible Polyaniline Poly (4 styrenesulfonate) Nanoparticles For Inkjet Printed Chemical Sensor Applications," *Advanced Materials*, vol. 19, pp. 1772-1775, 2007.
- [43] P. Calvert, "Inkjet printing for materials and devices," *Chemistry of Materials*, vol. 13, pp. 3299-3305, 2001.
- [44] M. Haque, K. Teo, N. Rupensinghe, S. Ali, I. Haneef, S. Maeng, J. Park, F. Udrea, and W. Milne, "On-chip deposition of carbon nanotubes using CMOS microhotplates," *Nanotechnology*, vol. 19, p. 025607, 2008.
- [45] S. B. Prakash, M. Urdaneta, M. Christophersen, E. Smela, and P. Abshire, "In situ electrochemical control of electroactive polymer films on a CMOS chip," *Sensors and Actuators B: Chemical*, vol. 129, pp. 699-704, 2008.
- [46] K. H. An, S. Y. Jeong, H. R. Hwang, and Y. H. Lee, "Enhanced Sensitivity of a Gas Sensor Incorporating Single-Walled Carbon Nanotube-Polypyrrole Nanocomposites," *Advanced Materials*, vol. 16, pp. 1005-1009, 2004.
- [47] Y.-T. Jang, S.-I. Moon, J.-H. Ahn, Y.-H. Lee, and B.-K. Ju, "A simple approach in fabricating chemical sensor using laterally grown multi-walled carbon nanotubes," *Sensors and Actuators B: Chemical*, vol. 99, pp. 118-122, 2004.
- [48] J. Watson, K. Ihokura, and G. S. V. Coles, "The Tin Dioxide Gas Sensor," *Measurement Science & Technology*, vol. 4, pp. 711-719, Jul 1993.

- [49] N. Yamazoe, Y. Kurokawa, and T. Seiyama, "Effects of additives on semiconductor gas sensors," *Sensors and Actuators*, vol. 4, pp. 283-289, 1983.
- [50] N. Barsan, M. Schweizer-Berberich, and W. Göpel†, "Fundamental and practical aspects in the design of nanoscaled SnO<sub>2</sub> gas sensors: a status report," *Fresenius' Journal of Analytical Chemistry*, vol. 365, pp. 287-304, 1999.
- [51] Y. Tokura, H. Takagi, and S. Uchida, "A superconducting copper oxide compound with electrons as the charge carriers," *Nature*, vol. 337, pp. 345-347, 1989.
- [52] Y. Xie and C. O. Huber, "Electrocatalysis and amperometric detection using an electrode made of copper oxide and carbon paste," *Analytical chemistry*, vol. 63, pp. 1714-1719, 1991.
- [53] X. M. Miao, R. Yuan, Y. Q. Chai, Y. T. Shi, and Y. Y. Yuan, "Direct electrocatalytic reduction of hydrogen peroxide based on Nafion and copper oxide nanoparticles modified Pt electrode," *Journal of Electroanalytical Chemistry*, vol. 612, pp. 157-163, 2008.
- [54] X. Li, Z. Gu, J. H. Cho, H. Sun, and P. Kurup, "Tin-copper mixed metal oxide nanowires: Synthesis and sensor response to chemical vapors," *Sensors and Actuators B: Chemical*, 2011.
- [55] G. Zhang and M. Liu, "Effect of particle size and dopant on properties of SnO<sub>2</sub>-based gas sensors," *Sensors and Actuators B: Chemical*, vol. 69, pp. 144-152, 2000.
- [56] T. Maekawa, J. Tamaki, N. Miura, and N. Yamazoe, "Improvement of copper oxide-tin oxide sensor for dilute hydrogen sulfide," *J. Mater. Chem.*, vol. 4, pp. 1259-1262, 1994.
- [57] J. Zhang, J. Liu, Q. Peng, X. Wang, and Y. Li, "Nearly Monodisperse Cu<sub>2</sub>O and CuO Nanospheres: Preparation and Applications for Sensitive Gas Sensors," *Chemistry of Materials*, vol. 18, pp. 867-871, 2006.
- [58] A. W. Smith and H. Wieder, "Oxygen Sorption and Electrical Conductivity of Copper Oxide Films," *The Journal of Physical Chemistry*, vol. 63, pp. 2013-2015, 1959.
- [59] X. Gou, G. Wang, J. Yang, J. Park, and D. Wexler, "Chemical synthesis, characterisation and gas sensing performance of copper oxide nanoribbons," *Journal of Materials Chemistry*, vol. 18, pp. 965-969, 2008.

- [60] S. T. Shishiyanu, T. S. Shishiyanu, and O. I. Lupan, "Novel NO<sub>2</sub> gas sensor based on cuprous oxide thin films," *Sensors and Actuators B: Chemical*, vol. 113, pp. 468-476, 2006.
- [61] P. R. Wallace, "The Band Theory of Graphite," *Physical Review*, vol. 71, p. 622, 1947.
- [62] A. K. Geim and K. S. Novoselov, "The rise of graphene," *Nature Materials*, vol. 6, pp. 183-191, Mar 2007.
- [63] J. T. Robinson, F. K. Perkins, E. S. Snow, Z. Wei, and P. E. Sheehan, "Reduced Graphene Oxide Molecular Sensors," *Nano Letters*, vol. 8, pp. 3137-3140, 2008.
- [64] P. Avouris, Z. Chen, and V. Perebeinos, "Carbon-based electronics," *Nat Nano*, vol. 2, pp. 605-615, 2007.
- [65] C. Virojanadara, M. Syväjarvi, R. Yakimova, L. Johansson, A. Zakharov, and T. Balasubramanian, "Homogeneous large-area graphene layer growth on 6H-SiC (0001)," *Physical Review B*, vol. 78, p. 245403, 2008.
- [66] Y. Xuan, Y. Wu, T. Shen, M. Qi, M. A. Capano, J. A. Cooper, and P. Ye, "Atomic-layer-deposited nanostructures for graphene-based nanoelectronics," *Applied Physics Letters*, vol. 92, p. 013101, 2008.
- [67] C. Gómez-Navarro, R. T. Weitz, A. M. Bittner, M. Scolari, A. Mews, M. Burghard, and K. Kern, "Electronic transport properties of individual chemically reduced graphene oxide sheets," *Nano Letters*, vol. 7, pp. 3499-3503, 2007.
- [68] T. Wehling, K. Novoselov, S. Morozov, E. Vdovin, M. Katsnelson, A. Geim, and A. Lichtenstein, "Molecular doping of graphene," *Nano Letters*, vol. 8, pp. 173-177, 2008.
- [69] T. Wehling, M. Katsnelson, and A. Lichtenstein, "Adsorbates on graphene: Impurity states and electron scattering," *Chemical Physics Letters*, vol. 476, pp. 125-134, 2009.
- [70] P. L. McEuen, M. S. Fuhrer, and P. Hongkun, "Single-walled carbon nanotube electronics," *Nanotechnology, IEEE Transactions on*, vol. 1, pp. 78-85, 2002.
- [71] J. Kong, N. R. Franklin, C. Zhou, M. G. Chapline, S. Peng, K. Cho, and H. Dai, "Nanotube Molecular Wires as Chemical Sensors," *Science*, vol. 287, pp. 622-625, January 28, 2000 2000.
- [72] P. N. Bartlett, P. B. M. Archer, and S. K. Ling-Chung, "Conducting polymer gas sensors part I: fabrication and characterization," *Sensors and Actuators*, vol. 19, pp. 125-140, 1989.

- [73] P. N. Bartlett and S. K. Ling-Chung, "Conducting polymer gas sensors Part III: Results for four different polymers and five different vapours," *Sensors and Actuators*, vol. 20, pp. 287-292, 1989.
- [74] G. Bidan, "Electroconducting conjugated polymers: New sensitive matrices to build up chemical or electrochemical sensors. A review," *Sensors and Actuators B: Chemical*, vol. 6, pp. 45-56, 1992.
- [75] H. Bai and G. Shi, "Gas sensors based on conducting polymers," *Sensors*, vol. 7, pp. 267-307, 2007.
- [76] A. J. Heeger, "Semiconducting and Metallic Polymers: The Fourth Generation of Polymeric Materials (Nobel Lecture)," *Angewandte Chemie International Edition*, vol. 40, pp. 2591-2611, 2001.
- [77] J. Janata and M. Josowicz, "Conducting polymers in electronic chemical sensors," *Nat Mater*, vol. 2, pp. 19-24, 2003.
- [78] H. M. McNair, J. M. Miller, and MyiLibrary, *Basic gas chromatography*: Wiley Online Library, 1969.
- [79] S. C. Terry, J. H. Jerman, and J. B. Angell, "A gas chromatographic air analyzer fabricated on a silicon wafer," *Electron Devices, IEEE Transactions on*, vol. 26, pp. 1880-1886, 1979.
- [80] B. H. Kim, F. E. Prins, D. P. Kern, S. Raible, and U. Weimar, "Multicomponent analysis and prediction with a cantilever array based gas sensor," *Sensors and Actuators B: Chemical*, vol. 78, pp. 12-18, 2001.
- [81] I. Sasaki, H. Tsuchiya, M. Nishioka, M. Sadakata, and T. Okubo, "Gas sensing with zeolite-coated quartz crystal microbalances--principal component analysis approach," *Sensors and Actuators B: Chemical*, vol. 86, pp. 26-33, 2002.
- [82] I. Lundström, T. Ederth, H. Kariis, H. Sundgren, A. Spetz, and F. Winqvist, "Recent developments in field-effect gas sensors," *Sensors and Actuators B: Chemical*, vol. 23, pp. 127-133, 1995.
- [83] "Op Amp Circuit Collection," Arlington: National Semiconductor Inc., 1978.
- [84] J. G. Webster and J. W. Clark, *Medical instrumentation : application and design*, 3rd ed. New York: Wiley, 1998.
- [85] D. Johns and K. W. Martin, *Analog integrated circuit design*. New York: John Wiley & Sons, 1997.
- [86] A. K. Anderson, K. Christoff, I. Stappen, D. Panitz, D. G. Ghahremani, G. Glover, J. D. E. Gabrieli, and N. Sobel, "Dissociated neural

representations of intensity and valence in human olfaction," *Nature Neuroscience*, vol. 6, pp. 196-202, Feb 2003.

- [87] C. Cortes and V. Vapnik, "Support-vector networks," *Machine Learning*, vol. 20, pp. 273-297, 1995.
- [88] B. Warner and M. Misra, "Understanding Neural Networks as Statistical Tools," *The American Statistician*, vol. 50, pp. 284-293, 1996.
- [89] P.-N. Tan, M. Steinbach, and A. Kumar, *Introduction to data mining*, 1st ed. Boston: Pearson Addison Wesley, 2006.
- [90] S. Dreiseitl and L. Ohno-Machado, "Logistic regression and artificial neural network classification models: a methodology review," *Journal of Biomedical Informatics*, vol. 35, pp. 352-359, 2002.
- [91] S. Wold, K. Esbensen, and P. Geladi, "Principal component analysis," *Chemometrics and Intelligent Laboratory Systems*, vol. 2, pp. 37-52, 1987.
- [92] H. Nanto, Y. Yokoi, T. Mukai, J. Fujioka, E. Kusano, A. Kinbara, and Y. Douguchi, "Novel gas sensor using polymer-film-coated quartz resonator for environmental monitoring," *Materials Science and Engineering: C*, vol. 12, pp. 43-48, 2000.
- [93] T. A. Dickinson, K. L. Michael, J. S. Kauer, and D. R. Walt, "Convergent, self-encoded bead sensor arrays in the design of an artificial nose," *Analytical chemistry*, vol. 71, pp. 2192-2198, 1999.
- [94] A. V. Shevade, M. A. Ryan, M. L. Homer, A. M. Manfreda, H. Zhou, and K. S. Manatt, "Molecular modeling of polymer composite-analyte interactions in electronic nose sensors," *Sensors and Actuators B: Chemical*, vol. 93, pp. 84-91, 2003.
- [95] X. Wang, W. P. Carey, and S. S. Yee, "Monolithic thin-film metal-oxide gas-sensor arrays with application to monitoring of organic vapors," *Sensors and Actuators B: Chemical*, vol. 28, pp. 63-70, 1995.
- [96] H.-K. Hong, H. W. Shin, D. H. Yun, S.-R. Kim, C. H. Kwon, K. Lee, and T. Moriizumi, "Electronic nose system with micro gas sensor array," *Sensors and Actuators B: Chemical*, vol. 36, pp. 338-341, 1996.
- [97] M. S. Freund and N. S. Lewis, "A chemically diverse conducting polymer-based "electronic nose"," *Proceedings of the National Academy of Sciences*, vol. 92, pp. 2652-2656, March 28, 1995 1995.
- [98] S. Parsa and L. Petho, "HMDS," Berkeley: Marvell Nanofabrication Center, 2010.
- [99] K. Emtsev, F. Speck, T. Seyller, L. Ley, and J. Riley, "Interaction, growth, and ordering of epitaxial graphene on SiC {0001} surfaces: A comparative

photoelectron spectroscopy study," *Physical Review B*, vol. 77, p. 155303, 2008.

- [100] S. Bhaviripudi, X. Jia, M. S. Dresselhaus, and J. Kong, "Role of kinetic factors in chemical vapor deposition synthesis of uniform large area graphene using copper catalyst," *Nano Letters*.
- [101] W. S. Hummers and R. E. Offeman, "Preparation of Graphitic Oxide," *Journal of the American Chemical Society*, vol. 80, pp. 1339-1339, 1958.
- [102] P. Nikolaev, M. J. Bronikowski, R. K. Bradley, F. Rohmund, D. T. Colbert, K. Smith, and R. E. Smalley, "Gas-phase catalytic growth of single-walled carbon nanotubes from carbon monoxide," *Chemical Physics Letters*, vol. 313, pp. 91-97, 1999.
- [103] R. T. K. Baker, "Catalytic growth of carbon filaments," *Carbon*, vol. 27, pp. 315-323, 1989.
- [104] J. Kong, A. M. Cassell, and H. Dai, "Chemical vapor deposition of methane for single-walled carbon nanotubes," *Chemical Physics Letters*, vol. 292, pp. 567-574, 1998.
- [105] S. C. Lyu, B. C. Liu, S. H. Lee, C. Y. Park, H. K. Kang, C. W. Yang, and C. J. Lee, "Large-scale synthesis of high-quality double-walled carbon nanotubes by catalytic decomposition of n-hexane," *The Journal of Physical Chemistry B*, vol. 108, pp. 2192-2194, 2004.
- [106] A. Thess, R. Lee, P. Nikolaev, H. Dai, P. Petit, J. Robert, C. Xu, Y. H. Lee, S. G. Kim, A. G. Rinzler, D. T. Colbert, G. E. Scuseria, D. Tománek, J. E. Fischer, and R. E. Smalley, "Crystalline ropes of metallic carbon nanotubes," *Science*, vol. 273, pp. 483-487, 1996.
- [107] C. Journet, W. K. Maser, P. Bernier, A. Loiseau, M. Lamy de la Chapelle, S. Lefrant, P. Deniard, R. Lee, and J. E. Fischer, "Large-scale production of single-walled carbon nanotubes by the electric-arc technique," *Nature*, vol. 388, pp. 756-758, 1997.
- [108] A. R. Harutyunyan, B. K. Pradhan, U. J. Kim, G. Chen, and P. C. Eklund, "CVD Synthesis of Single Wall Carbon Nanotubes under "Soft" Conditions," *Nano Letters*, vol. 2, pp. 525-530, 2002.
- [109] H. H. Wang, C. Y. Han, G. A. Willing, and Z. L. Xiao, "Nanowire and nanotube syntheses through self-assembled nanoporous AAO templates," *Self-Assembled Nanostructured Materials*, vol. 775, pp. 107-112, 394, 2003.
- [110] J. Oh, Y. Tak, and J. Lee, "Electrochemically Deposited NanoColumnar Junctions of Cu<sub>2</sub>O and ZnO on Ni Nanowires," *Electrochemical and Solid-State Letters*, vol. 8, pp. C81-C84, 2005.

- [111] "TECHNIC FB ACID COPPER PROCESS FOR THROUGH-HOLE PLATING OF PRINTED CIRCUIT BOARDS," Technic, Inc., 2010.
- [112] C. GÃmez-Navarro, R. T. Weitz, A. M. Bittner, M. Scolari, A. Mews, M. Burghard, and K. Kern, "Electronic Transport Properties of Individual Chemically Reduced Graphene Oxide Sheets," *Nano Letters*, vol. 7, pp. 3499-3503, 2007.
- [113] D. Joung, A. Chunder, L. Zhai, and S. I. Khondaker, "Space charge limited conduction with exponential trap distribution in reduced graphene oxide sheets," *Applied Physics Letters*, vol. 97, p. 093105.
- [114] X. Zheng, Y. Sakurai, Y. Okayama, T. Yang, L. Zhang, X. Yao, K. Nonaka, and C. Xu, "Dielectric measurement to probe electron ordering and electron-spin interaction," *Journal of Applied Physics*, vol. 92, p. 2703, 2002.
- [115] U. Kaatze, "Complex permittivity of water as a function of frequency and temperature," *Journal of Chemical & Engineering Data*, vol. 34, pp. 371-374, 1989.
- [116] C. Wohlfarth, "Dielectric constant of N,N-dimethylformamide," in *Data extract from Landolt-Börnstein IV/17: Static Dielectric Constants of Pure Liquids and Binary Liquid Mixtures*. vol. 17: Springer-Verlag Berlin Heidelberg, 2008.
- [117] G. Macfie, R. G. Compton, and H. R. Corti, "Electrical Conductivity and Solubility of KF in N,N-Dimethylformamide up to 125 Å°C," *Journal of Chemical & Engineering Data*, vol. 46, pp. 1300-1304, 2001.
- [118] S. Junya and et al., "Fabrication of a carbon nanotube-based gas sensor using dielectrophoresis and its application for ammonia detection by impedance spectroscopy," *Journal of Physics D: Applied Physics*, vol. 36, p. L109, 2003.
- [119] J. K. Srivastava, M. Prasad, and J. J. B. Wagner, "Electrical Conductivity of Silicon Dioxide Thermally Grown on Silicon," *Journal of the Electrochemical Society*, vol. 132, pp. 955-963, 1985.
- [120] J. A. Voorthuyzen, K. Keskin, and P. Bergveld, "Investigations of the surface conductivity of silicon dioxide and methods to reduce it," *Surface Science*, vol. 187, pp. 201-211, 1987.
- [121] H. A. Becerril, J. Mao, Z. Liu, R. M. Stoltenberg, Z. Bao, and Y. Chen, "Evaluation of solution-processed reduced graphene oxide films as transparent conductors," *Acs Nano*, vol. 2, pp. 463-470, 2008.

- [122] M. Dimaki and P. Bøggild, "Dielectrophoresis of carbon nanotubes using microelectrodes: a numerical study," *Nanotechnology*, vol. 15, p. 1095, 2004.
- [123] V. F. Drobny and L. Pulfrey, "Properties of reactively-sputtered copper oxide thin films," *Thin Solid Films*, vol. 61, pp. 89-98, 1979.
- [124] A. H. Jayatissa, K. Guo, and A. C. Jayasuriya, "Fabrication of cuprous and cupric oxide thin films by heat treatment," *Applied Surface Science*, vol. 255, pp. 9474-9479, 2009.
- [125] J. H. Hsieh, P. W. Kuo, K. C. Peng, S. J. Liu, J. D. Hsueh, and S. C. Chang, "Opto-electronic properties of sputter-deposited Cu<sub>2</sub>O films treated with rapid thermal annealing," *Thin Solid Films*, vol. 516, pp. 5449-5453, 2008.
- [126] Q. Cao and J. A. Rogers, "Ultrathin Films of Single Walled Carbon Nanotubes for Electronics and Sensors: A Review of Fundamental and Applied Aspects," *Advanced Materials*, vol. 21, pp. 29-53, 2009.
- [127] D. Hecht, L. B. Hu, and G. Gruner, "Conductivity scaling with bundle length and diameter in single walled carbon nanotube networks," *Applied Physics Letters*, vol. 89, pp. -, Sep 25 2006.
- [128] W. Steinhogel, G. Schindler, G. Steinlesberger, M. Traving, and M. Engelhardt, "Comprehensive study of the resistivity of copper wires with lateral dimensions of 100 nm and smaller," *Journal of Applied Physics*, vol. 97, p. 023706, 2005.
- [129] W. Wu, S. Brongersma, M. Van Hove, and K. Maex, "Influence of surface and grain-boundary scattering on the resistivity of copper in reduced dimensions," *Applied Physics Letters*, vol. 84, p. 2838, 2004.
- [130] R. Landauer, "Spatial Variation of Currents and Fields Due to Localized Scatterers in Metallic Conduction," *Ibm Journal of Research and Development*, vol. 32, pp. 306-316, May 1988.
- [131] X. Du, I. Skachko, A. Barker, and E. Y. Andrei, "Approaching ballistic transport in suspended graphene," *Nature Nanotechnology*, vol. 3, pp. 491-495, 2008.
- [132] D. Mann, A. Javey, J. Kong, Q. Wang, and H. Dai, "Ballistic transport in metallic nanotubes with reliable Pd ohmic contacts," *Nano Letters*, vol. 3, pp. 1541-1544, 2003.
- [133] A. Venugopal, L. Colombo, and E. Vogel, "Contact resistance in few and multilayer graphene devices," *Applied Physics Letters*, vol. 96, p. 013512, 2010.

- [134] K. Komvopoulos, "Surface engineering and microtribology for microelectromechanical systems," *Wear*, vol. 200, pp. 305-327, 1996.
- [135] M. Sridhar and M. Yovanovich, "Review of elastic and plastic contact conductance models: comparison with experiment," *Journal of thermophysics and heat transfer*, vol. 8, pp. 633-640, 1994.
- [136] J. A. Greenwood and J. B. P. Williamson, "Contact of Nominally Flat Surfaces," *Proceedings of the Royal Society of London. Series A, Mathematical and Physical Sciences*, vol. 295, pp. 300-319, 1966.
- [137] P. Zhou, C. Wu, and G. Ma, "Contact resistance prediction and structure optimization of bipolar plates," *Journal of Power Sources*, vol. 159, pp. 1115-1122, 2006.
- [138] L. Kogut and K. Komvopoulos, "Electrical contact resistance theory for conductive rough surfaces," *Journal of Applied Physics*, vol. 94, p. 3153, 2003.
- [139] R. Landauer, "Conductance determined by transmission: probes and quantised constriction resistance," *Journal of Physics: Condensed Matter*, vol. 1, p. 8099, 1989.
- [140] M. J. Allen, V. C. Tung, and R. B. Kaner, "Honeycomb Carbon: A Review of Graphene," *Chemical Reviews*, vol. 110, pp. 132-145, 2009.
- [141] F. Koffyberg and F. Benko, "A photoelectrochemical determination of the position of the conduction and valence band edges of p type CuO," *Journal of Applied Physics*, vol. 53, pp. 1173-1177, 1982.
- [142] F. Buonocore, F. Trani, D. Ninno, A. Di Matteo, G. Cantele, and G. Iadonisi, "Ab initio calculations of electron affinity and ionization potential of carbon nanotubes," *Nanotechnology*, vol. 19, pp. -, Jan 16 2008.
- [143] B. V. Zeghbroeck, "Principles of Semiconductor Devices," Boulder: University of Colorado, 2010.
- [144] B. L. Anderson and R. L. Anderson, *Fundamentals of semiconductor devices*. Boston: McGraw-Hill Higher Education, 2005.
- [145] E. H. Rhoderick, "Metal-semiconductor contacts," *Solid-State and Electron Devices, IEE Proceedings I*, vol. 129, p. 1, 1982.
- [146] D. R. Lide, *Basic laboratory and industrial chemicals : a CRC quick reference handbook*. Boca Raton: CRC Press, 1993.
- [147] D. R. Lide and H. V. Kehiaian, *CRC handbook of thermophysical and thermochemical data*. Boca Raton: CRC Press, 1994.